ORNL/TR--88/30

DE89 003249

PRODUCTION AND MUONIC DECAY OF THE Z^0 INTERMEDIATE VECTOR BOSON IN THE UA1 EXPERIMENT

Reinhard Leuchs

Translated from German.* Dissertation for the Attainment of the Doctoral Degree at the Mathematics and Natural Science Faculty of the Christian Albrechts University at Kiel (1988), 152 pp.

Prepared for the
OAK RIDGE NATIONAL LABORATORY
Oak Ridge, Tennessee 37831
operated by
MARTIN MARIETTA ENERGY SYSTEMS, INC.
for the
U.S. DEPARTMENT OF ENERGY
under Contract No. DE-AC05-84OR21400

---

*By Language Services, Knoxville, Tennessee.

ORNL/TR-88/30

PRODUCTION AND MUONIC DECAY OF THE Z^o INTERMEDIATE VECTOR BOSON IN THE UA1 EXPERIMENT

Dissertation
For the Attainment of the Doctoral Degree
at the
Mathematics and Natural Science Faculty
of the
Christian Albrechts University
at Kiel

Submitted by

Reinhard Leuchs

Kiel
1988

Referent: Prof. Dr. O. C. Allkofer

Co-referent: Prof. Dr. F Wagner

Date of oral examination: February 17, 1988

Approved for Publication,
at Kiel on: February 17, 1988

Prof. Dr. G. Wibberenz
Dean

Table of Contents

1. **Introduction** 1

2. **Theory of the Electroweak Interaction** 5
   - 2.1 The Fermi Theory 5
   - 2.2 The Gauge Theory of the Electroweak Interaction 11
     - 2.2.1 The Gauge Invariance of the Electroweak Interaction 12
     - 2.2.2 The Gauge Invariance of the Weak Interaction 15
     - 2.2.3 Spontaneous Symmetry Breaking 18
     - 2.2.4 The Higgs Mechanism 20
   - 2.3 The Standard Model 26
   - 2.4 Production and Detection of Vector Bosons 31

3. **The Equipment** 41
   - 3.1 The Storage Ring Facility 41
   - 3.2 The UA1 Detector 44
     - 3.2.1 The Central Detector 46
     - 3.2.2 The Electromagnetic Calorimeters 48
     - 3.2.3 The Hadron Calorimeters 50
   - 3.3 The Muon Detector 51
   - 3.4 The Muon Trigger 54
   - 3.5 Track Reconstruction 58
     - 3.5.1 Track Reconstruction in the Central Detector 58
     - 3.5.2 Track Reconstruction in the Muon Detector 60

3.5.3 The Method of Combined Momentum Fits 61
3.6 The Reconstruction of Jets and Neutrinos 63

4 Selecting the Z^0 Events 91
4.1 The Production of Muons 91
4.2 The Principle of Muon Detection 92
4.3 Calibration Using the Cosmic Radiation 94
4.4 On-Line Selection 97
4.4.1 The Geometric Acceptance 98
4.4.2 The Efficiencies of the Detector and the Trigger 100
4.5 Off-Line Selection 102
4.5.1 The Efficiency of the Selection Program 106
4.6 The Total Selection Coefficient 108

5 The Z^0 Data Sample 118
5.1 The Result of the Selection 118
5.2 The Background in the Sample 121
5.2.1 Meson Decays 122
5.2.2 Unabsorbed Hadrons 122
5.2.3 Cosmic Rays 123
5.2.4 $\tau^+\tau^-$ Pairs 125
5.2.5 Drell-Yan Pairs 127
5.2.6 The Total Background 128
5.3 Radiative Z^0 Events 128
5.3.1 Interpretation as Internal Bremsstrahlung 130
5.3.2 Interpretation via External Bremsstrahlung 132

6 The Production Properties 146
6.1 The Partial Production Cross Section 146
6.2 Comparison with Other Measurements 148
6.3 Quantum Chromodynamic Effects 149
6.3.1 The Longitudinal Motion of the Z^0 151
6.3.2 The Transverse Motion of the Z^0 153

7 Tests of the Standard Model 167
7.1 Determining the Mass of the Z^0 167
7.1.1 The Mass Fit 169
7.1.2 Corrections to the Mass Fit 172
7.2 The Determination of $\sin^2 \theta_W$) from the W and Z Masses 174
7.3 Determining the Radiative Corrections 177
7.4 The determination of $\sin^2 \theta_W$ from the Asymmetry 179
7.5 A Test of Lepton Universality 183
7.6 The Number of Neutrino Generations 185
7.7 Determining the ρ Parameter 190
7.8 The Search for Heavy W's and Z's 191

8 Summary 209

A Operation and Monitoring of the Muon Detector 213
A.1 The Power Supplies 213
A.2 Control of the Data Flow and the Events 214

B The Monte Carlo Simulation 221
B.1 The ISAJET Computer Program 221

Acknowledgments 225

Index of References 227

Index of Figures 235

Index of Tables 238

Chapter 1

Introduction

Elementary particle physics concentrates on two questions:

- What building blocks go to make up matter ?
- What holds these building blocks together ?

It has turned out that these two questions cannot be answered independently of each other, since the building blocks of matter cannot be sought without interactions of many kinds. The Greeks had already come to the view, based on considerations of principle, that matter consists of indivisible particles, the atoms [1]. We know today that this idea was correct, but we also understand that, because of the small size of atoms, and the limited technological means then available, they were unable to adduce proofs of the atomic theory. Neither did they succeed in arriving at an understanding of the causes for the holding together of matter, nor in relating this holding together with forces.

Only at the beginning of modern times did Newton [2] attain the insight that such forces may be mathematically described as fields; he developed the first field theory of the gravitational interaction. The concept of the field has remained, to this day, the foundation of theories of interactions.
In the 18th Century Faraday and Ampère succeeded in giving a consistent description of electric and magnetic phenomena, based on the motion of electric

charges. Shortly thereafter Hertz described the spreading of electromagnetic waves. Then, around the turn of the century, Maxwell formulated a complete theory which includes the entire field of electromagnetism by means of four field equations and three material equations [3]. This represents a milestone in the search for a large, unified (that is to say, valid for all physical processes) set of laws of nature. His theory brought optics, which until then had been a self-contained branch of classical physics, under the umbrella of electromagnetism. Shortly thereafter Einstein made an additional fundamental discovery, by showing that the electromagnetic interaction is transmitted via discrete particles, the photons, and not by continuous effects [4].

The electromagnetic phenomena act principally in the electron shells of the atoms, which are also responsible for the chemical properties of the elements. Further research now concentrates on the structure of the atoms themselves. In the course of investigating the electron shells around atoms the theory of quantum mechanics was soon developed; this theory called the principle of strict causality into question. Instead of working with strict cause-effect relationships, it became necessary to describe the events at the smallest dimensions by transition probabilities, under which matter may be transformed from one state to another.

Inside the electron shell it was suspected that an additional substance had to exist, which would carry the mass of the atom, and which would balance the charge of the electrons. With his scattering experiments Rutherford showed that in fact the atomic nucleus is extremely small in comparison to the whole atom, but nevertheless contains practically all of the atom's mass [5].

By applying quantum mechanics it was possible to understand the structure of the atom. However, the laws of nature then known how the atomic nucleus, carrying multiple positive charges, could hold together in such a very small volume.

Obviously what was needed for such stability of the nucleus and to explain the existence of this form of matter which until then had been quite unknown, was a very strong force or interaction.

In 1935 Yukawa postulated the nuclear forces, which he explained on the basis of the continuous exchange of particles which he called mesons [6]. The particles were taken to have mass, which had a consequence that was wholly unknown until then: the nuclear forces have a finite range, the potential with which these forces are described falls off faster than does either the Coulomb potential or the gravitational potential. The range of the nuclear forces is restricted to the order of magnitude of the diameter of the nucleus. The mass of the mesons is comparable with the mass of the "transmitter" or "receiver" particles of the interaction.

Ever since the end of the 19th Century an additional phenomenon with inexplicable cause was being examined, the artificial radioactivity discovered by Curie, which was created by bombarding heavy nuclei with α particles [7]. The ß radiation emitted in this process is the same as that emitted in natural radioactivity, which had been previously discovered by Becquerel [8]. A theory of ß decay was set up by Fermi in the 1930's [9]. Under certain conditions atomic nuclei can decay; in this process a neutron is transformed into a proton, and in addition an electron and a neutrino are emitted. This neutrino was unobservable, but it was postulated by Pauli to prevent the law of the conservation of energy from being endangered [10]. What was completely new in this reaction was the fact that one particle could transform into another, which led to the conclusion that an additional interaction of a different kind had to exist, which, because of its weak strength was designated as the weak interaction.

At the beginning of the second half of the century, the world could thus be described by means of nucleons, mesons, electrons, neutrinos, and photons. Four forces of nature were known: gravity, the electromagnetic force, the strong force, and the weak force. It appeared reasonable to search for a theory that would comprehensively describe the three stronger interactions. Quantum electrodynamics, which had been very successfully developed by Feynmann and others [11] was taken to be a model for such a comprehensive theory. Unfortunately, because of its very weak nature, gravity - the fourth force - has until now remained inaccessible to elementary particle physicists. Its coupling is almost 30 powers of ten smaller than that of the other interactions.

Since then the search has been on for such a comprehensive field theory which would be able to manage with as few free parameters as possible, and which would describe as many effects as possible. The strengths of the individual reactions as well as the particle masses and the quantum numbers of the particles, should arise out of the theory. To date the only success has been in combining the electromagnetic and weak forces into a single representation, which is named after its discoverers Glashow, Salam, and Weinberg [12, 13, 14]. This unified representation of the electroweak interactions of leptons and quarks has been declared to be the "standard model". However, the standard model is not yet a satisfactory theory, since it contains too many free parameters, namely at least 18, whose magnitudes cannot be predicted by the theory, and which must, so to say, be inserted into the model "by hand". Ideally a closed theory should contain no free parameters.

The theory of the electroweak interaction will be described in the next chapter. An important result of the electroweak theory is that it predicts the existence of heavy particles, the intermediate vector bosons, which are the carriers of the electroweak interaction. In particular, the theory also requires, in addition to the charged bosons, massive neutral bosons. In our experiment we succeeded, for the first time, in producing these particles directly, and thus producing a proof of the correctness of the Glashow, Salam, and Weinberg model. The experimental proof of the existence of the neutral interaction particles required by the theory, the Z^0 bosons, is the subject of this work.

Chapter 2

Theory of the Electroweak Interaction

2.1 The Fermi Theory

The Fermi theory [9] was the first to succeed in describing ß decay quantitatively as a process of the weak interaction. The calculation of the transition probability is carried out as a perturbation calculation to first order and yields:

$$W = \frac{2\pi}{\hbar} G^2 |M|^2 \frac{dN}{dE_0} \tag{2.1}$$

where G is the effective coupling constant, M the matrix element which contains a volume integration over the four participating fermion wave functions, and dN/dE_0 is the phase space factor that gives the state density in the final state. The matrix element is proportional to the overlap of the nucleon wave functions for the initial and final states. For allowed transitions, the Fermi transitions, this overlap is almost total, which means that $|M|^2$ becomes 1. W can be directly measured from the decay of O^{14} nuclei. Thus one obtains for the effective coupling constant:

$$G = \frac{10^{-5}}{M_p^2} \tag{2.2}$$

The matrix element of the beta decay is now determined by formulating the reaction differently:

$$n \rightarrow p + e + \bar{\nu} \Rightarrow n + \nu \rightarrow p + e \tag{2.3}$$

$$M = G(\psi_p^* O \psi_n)(\psi_e^* O \psi_\nu) \tag{2.4}$$

where O is a suitable operator which will be specified more exactly below. Such a formulation is used in analogy to the description of the electromagnetic scattering of two charged particles, for example ($e + p \rightarrow e + p$). This process can be handled as interaction between two currents, namely the electron current and the proton current. The coupling G is analogous to e^2. Quite generally, the operator O may be a scalar operator (S), a vector operator (V), an axial vector operator (A), or a pseudoscalar operator (P). Experimentally it is found that in the weak interaction only the V and A components play a role.

$$M = G \sum_{i=V,A} C_i(\psi_p^* O_i \psi_n)(\psi_e^* O_i \psi_\nu) \tag{2.5}$$

(For pure Fermi transitions $C_A = 0$.) This matrix element is a scalar parameter, and has definite parity. From the experiment based on a postulate by Lee and Yang [15], however, it is known that parity is not conserved in the weak interaction, since the neutrino participating in the reaction has maximum polarization [16]. It carries a spin 1/2 and has no mass. Its helicity of $H = \pm 1$. It is therefore necessary to introduce a pseudoscalar component into the matrix element which will project out the helicity of the neutrino. This is achieved by multiplying the wave function by $(1 \pm \gamma_5)$, so:

$$M = G \sum_{i=V,A} C_i (\psi_p^* O_i \psi_n)(\psi_e^* O_i (C_j + C_j' \gamma_5) \psi_\nu) \tag{2.6}$$

Since the neutrino is left-handed, it follows that for the correct projector $(1 \pm \gamma_5)$, $C_j = C'_j = 1$. It remains only to determine C_A and C_V. This is done experimentally by measuring the interference terms of the vector and axial vector components using polarized neutrons, by measuring the angular distribution of the reaction products from neutron decay [17]. For leptons one finds:

$$C_A = -C_V \tag{2.7}$$

For this reason the theory is also known as V-A theory. For nucleons one does not find pure V-A behavior, since the strong force also plays a role. For nucleons one has [18]:

$$\lambda = -\frac{C_A}{C_V} = 1.25 \tag{2.8}$$

The final matrix element that results is:

$$M = G\, C_V\, (\psi_p^* \gamma^\mu (1 + \lambda\gamma_5) \psi_n)\, (\psi_e^* \gamma_\mu (1 + \gamma_5) \psi_\nu) \tag{2.9}$$

In order for the expectation value of the reaction to be an observable, the matrix element must be hermitian, in other words we still have to add the hermitian conjugate component and renormalize: $M' = (1/\sqrt{2})(M + M^\dagger)$.

The universal Fermi interaction is a four-fermion interaction with a current-current coupling whose Lagrange function, with its lepton and nucleon currents, may be written as

$$L = \frac{G}{\sqrt{2}} J^{\mu} J_{\mu}^{\dagger} \tag{2.10}$$

This theory has a fundamental flaw which results from the fact that a local four-fermion interaction is to be described: The cross section diverges at high energies. This stems from the dimension-containing coupling constant, consequently the cross sections must contain a term proportional to E. For example, for the reaction $\nu_e + e^- \rightarrow \nu_e + e^-$, where p is the momentum of the electrons, one has:

$$\sigma \approx \frac{2G_F^2}{\pi} p^2. \tag{2.11}$$

From scattering theory it is known that the maximum scattering cross section can be expanded in terms of the partial wave amplitudes:

$$\sigma = \left(\frac{4\pi^2\hbar^2}{p^2}\right) \sum_j (2j+1) |f_j|^2 \tag{2.12}$$

where f_j is the amplitude of the j'th partial wave. A point-like interaction signifies s-wave scattering, that is to say, $j = 0$; furthermore, it is true that $f_j \leq 1$. From this it is possible to calculate a maximum momentum at which the effective cross section is greater than the scattering cross section; one says that unitarity is violated: $p_{max} \geq 666$ GeV.

The question has therefore arisen as to how to eliminate this divergence. A comparison with the successful elimination of such a divergence in quantum electrodynamics shows that there the cross sections of such reactions as, for example, $e^+ + e^- \rightarrow \mu^+ + \mu^-$ the cross sections decrease with increasing energy, and therefore do not violate the unitarity condition

$$\sigma_{QED} = \frac{\alpha^2}{E_{cm}} \tag{2.13}$$

Quantum electrodynamics is a renormalizable theory. Any possible divergences due to higher-order effects, such as vacuum polarization around a point-like electron, which lead to infinite field energy, are eliminated by re-defining the charge and the mass of the particles.

A way out of the divergence problem of the weak interactions is found by giving up the point-nature of the interaction, and introducing a dimensionless coupling constant. In order to describe the short range of the weak interaction correctly, one needs a massive exchange particle which mediates the interaction [19, 20]. The following statements can be made, regarding this particle:

- The charge should be ± 1, since (at that point in time) only charged currents were observed in the weak interaction.
- The spin should be 1, in order to guarantee the V-A character.
- The mass should be at lest several GeV.
- Its coupling strength to other particles is specified by measurements at low energies.

Fig. 2.1shows the representation of the reaction according to the views to date and according to the new conception.

Instead of the old effective coupling constant $G_F/\sqrt{2}$, a new coupling g must, of course, be introduced at each vertex. The exchange of the W particles is described by a propagator of the type

$$g^{\mu\nu}(1 - \frac{q^{\mu}q^{\nu}}{M_W^2})\frac{1}{q^2 - M_W^2} \tag{2.14}$$

For small q^2 one obtains, just as before, the old form of the Fermi interaction, and so one has

$$\frac{G_F}{\sqrt{2}} = \frac{g^2}{m_W^2} \tag{2.15}$$

If one assumes a comparable coupling strength as for the electromagnetic interaction, in other words:

$$g^2 = e^2 = 4\pi\alpha \quad , \tag{2.16}$$

then one finds $m_W \approx 100$ GeV.

Unfortunately this does not completely eliminate the divergences. The unitarity limit is still violated, even though now only a logarithmic divergence appears. In addition, effects of higher order lead to a quadratic divergence, where σ grows in proportion to the square of the center-of-mass energy, for example in the reaction

$$\nu_\mu + \bar{\nu}_\mu \rightarrow W^+ + W^- \rightarrow \nu_\mu + \bar{\nu}_\mu \tag{2.17}$$

Thus the theory is still not renormalizable. This process must be artificially damped by introducing an additional interaction with a new, neutral exchange particle, called Z^0, so that the two reactions interfere destructively. This Z^0 should then couple to all the fermions and the W bosons· However an additional problem now raises its head. Since the Z^0 couples to fermions, there are l^+l^- annihilation processes which are in interference with an exchange of photons, so that a total of 3 reactions are possible, which are shown in Fig. 2.2, the exchange of a photon, a Z^0 or a neutrino. Their relative strength must be exactly balanced in such a way that the total cross section does not diverge.

The Z^0 thus couples to a Fermi current that consists of two parts:

- The V-A part, in which only left-handed fermions and right-handed antifermions participate
- A part that must look exactly like an electromagnetic current.

The relative strength depends on the ratio of the coupling constants of the V-A interaction and the electromagnetic interaction. One assigns an angle to this ratio and defines

$$\sin\theta_W = \frac{e}{g} \tag{2.18}$$

The current, to which the Z°, couples then becomes:

$$J^{Z^0} = J^{(V-A)} + \sin^2\theta_W \cdot J^{em} \tag{2.19}$$

The first reaction, which can be explained only by such "neutral currents" was found as early as 1973 in muon-electron scattering [21].

This made it clear that the phenomena of the weak interaction and the electromagnetic interaction are closely related to one another, and should be capable of being described by one comprehensive theory.

2.2 The Gauge Theory of the Electroweak Interaction

The fundamental idea of the theory of the electroweak interaction is the concept of the local gauge invariance in the field theory. The principles of such a theory will now be explained, from which, ultimately, follows the "standard model" which is the theory that is generally accepted today.

2.2.1 The Gauge Invariance of the Electromagnetic Interaction

Symmetry principles have always played a very important role in physics. According to Noether's Theorem, every symmetry law has the conservation of some physical parameter as a consequence. It is a common feature of all symmetry laws that the field equations retain their validity if the phases of the quantum-mechanical states are uniformly altered everywhere in space; this phase is not a quantum-mechanical observable, it is not measurable.

$$U: \quad \psi(x) \rightarrow \psi'(x)e^{i\theta} \tag{2.20}$$

Invariance under such a transformation is called global gauge invariance. A stronger symmetry is derived from the requirement of local gauge invariance. This means that now the phase shift no longer has to take place at all points in the space-time continuum uniformly, but rather may look different everywhere; Θ is to be a function of x.

$$U(x): \quad \psi(x) \rightarrow \psi'(x)e^{i\theta(x)} \tag{2.21}$$

Invariance under such local transformations U(x) is called gauge symmetry. Since in this case, however, the relative phases of the states are changed, and thus the observables of the system are also changed, an additional mechanism is needed to compensate for these changes. In general, an additional field must be introduced.

In the case of a free electron, for example, one adds a mass-less vector field, the photon, which, it is true, in contrast to the electron does not carry a charge.

This photon then couples to the charged current. It is known that the sequence of several couplings of photons to an electron has no influence on the final state, since these transformations commute. Quantum electrodynamics describes these processes; because of the commutative properties they are called Abelian gauge theory.

We now consider the Lagrange function of a free fermion, for example, the electron

$$L_{frei} = i\bar{\psi}(x)\gamma^{\mu}\partial_{\mu}\psi(x) - m\bar{\psi}(x)\psi(x) \quad , \tag{2.22}$$

{Translator's note: the subscript "frei" translates as "free"]} which remains invariable under global transformation, since the gradient $\partial_{\mu}\psi(x)$ transforms exactly like $\psi(x)$ if an x-independent phase factor is introduced into ψ. The fundamental requirement of gauge theories now consists in demanding that this phase shall be unobservable not only globally, but also locally, no matter where one is positioned in space. The phase shift Θ may be x-dependent.

This requirement has effects on terms in the Lagrange function that contain derivatives, on the kinetic terms. Additional terms that arise must be compensated for, and the kinetic term must be redefined, if a new vector field is introduced with the minimum substitution.

$$L \Rightarrow L' = i\bar{\psi}(x)\gamma^{\mu}[\partial_{\mu} - ieA_{\mu}]\psi(x) - m\bar{\psi}(x)\psi(x) \tag{2.23}$$

A_{μ} is the so-called Yang-Mills field. Thus the minimal coupling to the gauge field describes the covariant derivative $D_{\mu} = (\partial_{\mu} - A_{\mu})$. With this one obtains the new form of the Lagrange function:

$$L = \bar{\psi}(i\gamma^{\mu}D_{\mu} - m)\psi \tag{2.24}$$

$$= \bar{\psi}(i\gamma^{\mu}\partial_{\mu} - m)\psi + e\bar{\psi}\gamma^{\mu}A_{\mu}\psi \tag{2.25}$$

$$= L_{free} + eJ^{\mu}A_{\mu} \tag{2.26}$$

In the new form of the interaction J^{μ} is the charged, conserved current from the consideration of the global gauge invariance. In order to identify $A\mu$ as emitted vector field it is necessary to introduce an additional kinetic term which contains the field energy of the gauge field, thus in the present case of the photon:

$$L_{kin} = -\frac{1}{4}F_{\mu\nu}F^{\mu\nu}, \quad F_{\mu\nu} = \partial_{\mu}A_{\nu} - \partial_{\nu}A_{\mu}, \tag{2.27}$$

which remains invariant under local gauge transformation, and which corresponds to a mass-less particle. An explicit mass term in the Lagrange function in analogy with the Klein-Gordon equation ($\Box + m^2)A = 0$ would have the form

$$L_m = -\frac{1}{2}m_A^2 A_{\mu}(x)A^{\mu}(x) \ . \tag{2.28}$$

Such a mass term is not invariant, and is therefore strictly forbidden in local gauge theories. A Yang-Mills field must always be mass-less. The final form of the Lagrange function for a fermion and a photon field under gauge transformation $U(x)$ reads:

$$L = L_{free} + eJ_{\mu}A^{\mu} - \frac{1}{4}F_{\mu\nu}F^{\mu\nu} \tag{2.29}$$

Frequent attempts have been made to measure the mass of the photon in order to test the correctness of the theory. The best estimate today stems from magnetic field measurements at the planet Jupiter, made by the Pioneer X Probe [22].

$$m_\gamma \leq 6 \cdot 10^{-16}\ eV \tag{2.30}$$

2.2.2 The Gauge Invariance of the Weak Interaction

On the way to the unified theory of the electroweak interaction it appears very reasonable to investigate how the vector bosons of the weak interaction behave under a local gauge transformation. It is already clear that the masses of the bosons magnify the problem. In addition the bosons carry electric charges and hence couple to the photon. Whereas in quantum electrodynamics one is dealing with a one-dimensional transformation U(x) with one free parameter θ (x), in gauging the weak fields it is necessary to carry out transformations in higher dimensions; several parameters are required. The weak interaction affects a fermion multiplet, and the gauging should produce at least three gauge bosons.

Initially we shall limit our consideration to the interaction of the leptons and the gauge bosons. Leptons occur in left-handed and right-handed form; they may be arranged in a "weak isospin" space that contains a left-handed doublet and a right-handed singlet:

$$\mathbf{L}: \begin{pmatrix} \nu \\ e \end{pmatrix}_L = \frac{1}{2}(1-\gamma_5)\begin{pmatrix} \nu \\ e \end{pmatrix} \tag{2.31}$$

$$\mathbf{R}: \ e_R = \frac{1}{2}(1+\gamma_5)e \tag{2.32}$$

In order to include the electromagnetic interaction also, we make use of the Gell-Mann-Nishijima relationship, which ties together the hypercharge Y, the charge Q, and the weak isospin T:

$$Y = Q - T_3 \tag{2.33}$$

and define the weak hypercharge Y. Table 2.1 shows the electroweak quantum numbers which the leptons carry. The quantum numbers of the quarks, which will later be fitted into the model of the electroweak interaction, are also included.

In the discussion that follows we will treat mass-less fermions and mass-less gauge bosons. The fermions carry the weak hyper-charge Y and couple to the mass-less vector field B. Furthermore, we give the fermions weak isospin $\vec{T}$ and let them be coupled to the mass-less iso-vector field W. We also assume that the fundamental transformation group generated by $\vec{T}$ and Y has the character $SU_2 \times U_1$, and require invariance under

$$\psi(x) \rightarrow U(x)\psi(x) \quad U(x) = U_2(x) \times U_1(x) \ . \tag{2.34}$$

The transformations U_1 and U_2 are first expanded in their generators:

$$U_1(x) \ = \ e^{iY\theta(x)} \tag{2.35}$$

$$U_2(x) \ = \ e^{i\vec{T}\vec{\alpha}(x)} \tag{2.36}$$

where Θ and $\vec{\alpha}$ are the local parameters, while Y and $\vec{T}$ are the generators. It is known that a SU(N) matrix has a total of $N^2 - 1$ real parameters, hence our gauge transformations together have four parameters, to which four gauge fields correspond, which are required to make the Lagrange function of the free fermions gauge invariant. These fields are designated as B_μ and $\vec{W}_\mu = (W_\mu^1, W_\mu^2, W_\mu^3)$. The covariant derivatives, which yield the coupling of the material fields to these gauge fields, read:

$$D_\mu^R = \partial_\mu - i g' Y \cdot B_\mu \tag{2.37}$$

$$D_\mu^L = \partial_\mu - i g \vec{T} \cdot \vec{W} - i g' Y \cdot B_\mu \tag{2.38}$$

The right-handed singlet thus couples to field B; the left-handed doublet to the field $\vec{W}$.

After some complicated transformations one finally obtains the transformation behavior of these four gauge fields:

$$\vec{W}'_\mu = \vec{W}_\mu - \vec{\alpha} \times \vec{W}_\mu + \frac{1}{g}\partial_\mu \vec{\alpha} \qquad , U_2 = e^{i\vec{\alpha}\vec{T}} \tag{2.39}$$

$$B'_\mu = \qquad B_\mu + \frac{1}{g'}\partial_\mu \theta \qquad , U_1 = e^{i\theta(x)Y} \tag{2.40}$$

In order now to identify B_μ and W_μ with the physical particles we must, analogously as in the case of the photon, construct a kinetic term which contains the fields themselves and their derivatives. For B this is:

$$L_{kin}(B) = -\frac{1}{4}B_{\mu\nu}B^{\mu\nu}, \quad B_{\mu\nu} = \partial_\mu B_\nu - \partial_\nu B_\mu, \tag{2.41}$$

in complete analogy to the photon case. The case of the Ws is more difficult because of the cross products $\vec{\alpha}$ x $\vec{W}$. Here the solution reads:

$$L_{kin}(W) = -\frac{1}{4}\sum_{i=1}^{3} W^i_{\mu\nu} W^i_{\mu\nu} \tag{2.42}$$

(2.43)

A remarkable property emerges: The gauge bosons arising from a non-Abelian ansatz exhibit a self-interaction for which there is no correspondence in the case of the photon. The W field couples to all particles that carry weak isospin, hence also to itself. In the self-interaction there appear both three-fold and four-fold vertices.

2.2.3 Spontaneous Symmetry Breaking

Similarly to the situation in quantum electrodynamics we know that the W_μ fields must be mass-less, since explicit mass terms of the form $M_W^2 W_\mu W^\nu$ violate the local gauge invariance, and therefore may not appear in the Lagrange function. An exact consideration reveals that even the participating fermions must be mass-less. We know only the following: The fermions carry the weak hyper-charge and couple gauge-invariantly to the mass-less vector field B_μ. In addition we assign a weak isospin to the fermions, and permit them to couple to the mass-less vector field $\vec{W}_\mu$. The Lagrange function then exhibits invariance under the transformation $SU_2 \times U_1$. The particles derive their mass by means of the new mechanism of spontaneous symmetry breaking. How this happens will now be explained:

For simplicity's sake we shall start by considering a Lagrange function which is invariant under a global gauge transformation, and which shall allow a self-interaction. Let the field under consideration be ϕ and the potential in which the self-interaction appears be $V(\phi)$. It is to depend on the field ϕ at most to fourth power, and be symmetric in ϕ (this is the simplest assumption that will allow the argument which follows):

$$L = \frac{1}{2}(\partial_\mu \phi)^2 - V(\phi) \ , \ V(\phi) = \mu^2\phi^2 + \lambda\phi^4 \qquad (2.44)$$

With this Lagrange function we shall show that, although the Lagrange function itself is invariant under the gauge transformation (here, for simplicity's sake the discrete transformation $\phi \to -\phi$), this is not necessarily true for the ground state of the system, the vacuum expectation value or the state of lowest energy. For the described potential various ground states exist, where $\partial V / \partial\phi = 0$ ($\lambda > 0$).

$$\frac{\partial V}{\partial \phi} = (2\mu^2 + 4\lambda\phi^2)\phi = 0 \tag{2.45}$$

For $\mu^2 > 0$ a minimum occurs at $\phi_0 = 0$. However, it will be seen that for $\mu^2 < 0$ two possible ground states exist; another way of saying this is that the vacuum is degenerate (see Section 2.3). In this case ϕ_0 is not equal to $-\phi_0$, the ground state is no longer an eigenstate of the symmetry operation, which it still was in the case where $\mu^2 > 0$. Thus the symmetry is broken spontaneously. An important result is: The vacuum expectation value no longer lies at $\phi_0 = 0$.

We shall now redefine the field ϕ so that the minimum will again lie at $\phi' = 0$, and expand the potential about this new minimum to second order in ϕ':

$$V(\phi') = -2\mu^2\phi'^2 + O(\phi'^3) + \ldots \tag{2.46}$$

ϕ' can then be interpreted as a massive particle which moves out of the ground state in a parabolic potential.

The Lagrange function for a complex field ϕ (which may, for example, describe a spin 0 particle with hypercharge) is constructed in the same way:

$$V = \mu^2\phi^*\phi + \lambda(\phi^*\phi)^2 \ , \tag{2.47}$$

$$L = \partial_\mu \phi^* \partial^\mu \phi - \mu^2 \phi^* \phi - \lambda(\phi^* \phi)^2 \tag{2.48}$$

This Lagrange function is invariant under the U_1 transformation $\phi \rightarrow e^{i\theta}\phi$. As before, the potential has a minimum at $\phi_0 = 0$ for $\mu^2 > 0$. In case $\mu^2 < 0$, several solutions result:

$$\phi_0 = \sqrt{\frac{-\mu^2}{2\lambda}} e^{i\theta} \ . \tag{2.49}$$

The ground state is again degenerate (see Fig. 2.3); it is no longer invariant under hypercharge exchange, whereas the Lagrange function still possesses this property. The excitation spectrum of the massive particle is obtained by expanding the field ϕ around the minimum value. The variation is done in two coefficients, the remaining degrees of freedom:

- on the circle on which the minima lie (coordinate ϕ_1)
- perpendicular thereto, in other words, radial (ϕ_2).

The potential can be expanded in ϕ_1 and ϕ_2 around the minimum. The expansion in ϕ_2 describes a particle with mass $\sqrt{-2\mu^2}$ in a parabolic potential, while the expansion in ϕ_1 designates a mass-less scalar particle, which is called the Goldstone boson [23]. Clearly the number of Goldstone bosons in a system depends on the number of degrees of freedom of the potential, expressed in the coordinates ϕ_n.

2.2.4 The Higgs Mechanism

These considerations will now be extended to Lagrange functions in which both the gauge fields as well as the matter fields exhibit self-interactions. all these fields are to be invariant under gauge transformation. Both fields appear in powers up to fourth order. In this case mass-less Goldstone bosons do not appear from the invariance considerations and the spontaneous symmetry breaking, but instead massive gauge bosons appear. The gauge fields obtain mass, or the corresponding degrees of freedom of the fields give the vector bosons their mass. This process is called the Higgs mechanism [24] or symmetry breaking of the second kind.

As we have already seen, the kinetic term of the Lagrange function is no longer invariant under local gauge transformation, in contrast to the potential in the Lagrange function. Hence a gauge field B_μ must be introduced. The Lagrangian then becomes:

$$L = (D^\mu\phi)^*(D_\mu\phi) - V(\phi\phi^*) \tag{2.50}$$

$$D_\mu = \partial_\mu - igB_\mu \ . \tag{2.51}$$

Consider the transformation behavior under

$$\phi \rightarrow \phi e^{i\theta(x)} \ , \ B_\mu \rightarrow B_\mu + \frac{1}{g}\partial_\mu\theta(x) \ . \tag{2.52}$$

The complete Lagrangian then reads:

$$L = (\partial_\mu + igB_\mu)\phi^*(\partial_\mu - igB_\mu)\phi - \frac{1}{4}B_{\mu\nu}B^{\mu\nu} - V(\phi^*\phi) \tag{2.53}$$

$$B_{\mu\nu} = \partial_\mu B_\nu - \partial_\nu B_\mu \tag{2.54}$$

$$V(\phi^*\phi) = \mu^2(\phi^*\phi) + \lambda(\phi^*\phi)^4 \tag{2.55}$$

(In the case where $\mu^2 > 0$, B_μ can be considered as the photon.) For $\mu^2 < 0$ the gauge symmetry is again broken spontaneously, and we obtain a vacuum expectation value different than 0 for the complex field ϕ. The complex field ϕ is now expressed in terms of two real fields ϕ_1 and ϕ_2 and an expansion is carried out around the ground state ϕ_0. We also define $v^2 = \mu^2/\lambda$.

$$\phi = \frac{1}{\sqrt{2}}(\phi_1 + i\phi_2) + \phi_0 \tag{2.56}$$

$$= \frac{1}{\sqrt{2}}(\phi_1 + v + i\phi_2) \tag{2.57}$$

$$\approx \frac{1}{\sqrt{2}}(\phi_1 + v)e^{\frac{i\phi_2}{v}} \tag{2.58}$$

We make use here of the gauge invariance and thus eliminate the field ϕ_2:

$$\phi \rightarrow \phi e^{-i\phi_2/v} = \phi_1 + v \quad , B'_\mu = B_\mu + (-\frac{1}{v}\partial_\mu\phi_2) \tag{2.59}$$

The Lagrange function now describes a massive vector boson B_μ with mass

$$M_B = gv \quad (v^2 = \frac{\mu^2}{\lambda}) \tag{2.60}$$

which results from its interaction with the scalar field ϕ. The ground state of the system is again at $\phi_0 \neq 0$. The scalar field ϕ_1 also has a mass of $\sqrt{(-4\mu^2)}$.
The field ϕ_2 has completely disappeared from the description as well as the degeneracy of the ground state. The following overall picture emerges:

Initially one has a mass-less vector field B with two spin states and two scalar fields ϕ, with one spin state each; this results in four degrees of freedom in the Lagrange function. After the spontaneous symmetry breaking the resulting massive vector particle has three polarization states which result from the absorption of the mass-less Goldstone bosons, and the fourth degree of freedom survives in the massive field ϕ_1, which is also called the Higgs particle. It has been successfully shown that such a local gauge theory with spontaneously broken symmetry is renormalizable with finite masses, if one introduces an additional massive particle, the Higgs boson [25].

Up to now we have been dealing only with fields that carry the weak hypercharge. However, these considerations now need to be carried a step further, in that we need to consider a field that carries both hypercharge and weak isospin, and which satisfies the symmetry $SU_2 \times U_1$. We consider, in other words, an iso-doublet $\begin{pmatrix} \phi' \\ \phi \end{pmatrix}$ with hypercharge $Y = 1/2$ and a self-interaction in the potential $V(\phi)$. The associated Lagrangian

$$L = (D_\mu\phi)^\dagger(D^\mu\phi) - V(\phi^\dagger\phi) \quad ,V(\phi^\dagger\phi) = \mu^2(\phi^\dagger\phi) + \lambda(\phi^\dagger\phi)^2 \tag{2.61}$$

is symmetric under the transformation $\phi \rightarrow U\phi$, where

$$U = e^{iY\alpha(x)}e^{iT\beta(x)} \ . \tag{2.62}$$

Let the complex field doublet be

$$\phi = \frac{1}{\sqrt{2}}(\phi_1 + i\phi_2) \quad \phi' = \frac{1}{\sqrt{2}}(\phi'_1 + i\phi'_2) \tag{2.63}$$

Spontaneous symmetry breaking again occurs for $\mu^2 < 0$. An expansion about the vacuum expectation value produces a mass term in the Lagrange function of the form

$$L_m = |(g\vec{T}\vec{W}_\mu + g'YB_\mu)\phi_0|^2 \tag{2.64}$$

$$= \frac{1}{2}(\frac{1}{4}g^2v^2)(W_\mu^{(1)^2} + W_\mu^{(2)^2}) + \frac{1}{4}v^2(gW_\mu^{(3)} - g'B_\mu)^2 \tag{2.65}$$

(g is the coupling strength of $\vec{W}$ to the weak isospin, g' is the coupling strength of B_μ to the hypercharge.) The mass term contains three massive gauge bosons, $W_\mu^{(1)}$, $W_\mu^{(2)}$, and a linear combination of B_μ and $W_\mu^{(3)}$. The composite term, which contains a product of B_μ and $W_\mu^{(3)}$ can be diagonalized into two orthogonal combinations of B_μ and $W_\mu^{(3)}$:

$$Z_\mu = \cos\theta_W W_\mu^{(3)} - \sin\theta_W B_\mu \tag{2.66}$$

$$A_\mu = \sin\theta_W W_\mu^{(3)} + \cos\theta_W B_\mu \tag{2.67}$$

The following fields then describe the massive gauge bosons W± and Z^0 and the mass-less photon:

$$W_\mu^\pm = \frac{1}{\sqrt{2}}(W_\mu^1 + iW_\mu^2) \tag{2.68}$$

$$Z^\circ{}_\mu = \frac{1}{\sqrt{g^2 + g'^2}}(gW_\mu^{(3)} - g'B_\mu) \tag{2.69}$$

$$A_\mu = \frac{1}{\sqrt{g^2 + g'^2}}(gW_\mu^{(3)} + g'B_\mu) \tag{2.70}$$

The Lagrange function of the electroweak interaction can then be written as

$$L_{ew} = gJ_\mu^T\vec{W}_\mu + g'J_\mu^Y B_\mu \tag{2.71}$$

with the weak iso-spin $\vec{J}_\mu{}^T$ and the hypercharge current $J_\mu{}^Y$. Because of

$$Y = Q - T_3 \tag{2.72}$$

we may write

$$J_\mu^Y = J_\mu^{(e)} - J_\mu^{T_3} L_{ew} = g \vec{J}_\mu^T \vec{W}_\mu + g'(J_\mu^{(e)} - J_\mu^{T_3}) B_\mu \tag{2.73}$$

with the weak mixing angle

$$\tan\theta_W = \frac{g}{g'} \tag{2.74}$$

we finally obtain the complete Lagrange function:

$$L_{ew} = \left(\frac{g}{2\sqrt{2}}\right)(2J_\mu^- W_\mu^+ + 2J_\mu^+ W_\mu^-) \quad \text{(charged current)} \tag{2.75}$$

$$+ \frac{g}{\cos\theta_W}(J_\mu^{(3)} - J_\mu^{(e)} \sin\theta_W{}^2) Z_\mu \quad \text{(neutral current)} \tag{2.76}$$

$$+ \quad g' J_\mu^{(e)} A_\mu \cos\theta_W \quad \text{(electromagnetic current)} \tag{2.77}$$

The charged weak current carries the lower component of a left-handed fermion doublet into the upper component, and inversely, by being coupled to a W. The current has both a vector and an axial vector component:

$$J = \frac{1}{2} \sum_f \bar{f}(g_V^f \gamma^\mu - g_A^f \gamma^\mu \gamma^5) f \tag{2.78}$$

The vector and axial vector components have equal strengths. The neutral current ties together fermions of the same type; gV and gA depend on the type of fermion here. Table 2.2 summarizes the components.

In addition to the leptons, the quarks [26, 27] also participate in the weak interaction. The quarks are also fundamental fermions, which do, however, carry electric charges in thirds. Furthermore, free quarks are not observable, but are observable only when formed into bound states of 2 or 3 quarks. It was in 1972 that Glashow, Iliopoulos and Maiani first achieved the insight that the quarks are based on the same generation structure as the leptons, and that therefore an identical treatment of the quarks and leptons is possible in the electroweak interaction [29].

2.3 The Standard Model

With the approach described here we have found a possible theoretical ansatz to be used in explaining the electromagnetic and weak interactions of the fundamental fermions. This results in giving us the massive gauge bosons in a simple manner from field-theory principles. At the same time, the currents required initially were produced. Furthermore, the model is in agreement with all experiments on the electroweak interaction. It is the simplest description of the combined electromagnetic and weak interactions of the leptons and quarks, and is therefore also called the "standard model."

We turn once again to the couplings. From the general Lagrange function of the electroweak interaction we can derive the coupling strengths by comparison with quantum electrodynamics:

$$e = g \sin\theta_W = g' \cos\theta_W \tag{2.79}$$

One sees immediately that the coupling to the W and Z bosons is of the same order of magnitude as the electromagnetic coupling e. If one now compares the coupling of the charged current with the coupling constant of the weak interaction known from the Fermi theory, which has been determined experimentally, the result is:

$$\frac{g}{2\sqrt{2}} = g_W = m_W\left(\frac{G}{\sqrt{2}}\right)^{1/2} \tag{2.80}$$

This may be used to calculate the mass of the W boson:

$$m_W = \left(\frac{e^2\sqrt{2}}{8G}\right)^{1/2} / \sin\theta_W \ (GeV/c^2) \tag{2.81}$$

The masses of the W and Z boson are interrelated:

$$m_W^2 = m_Z^2 \cos^2\theta_W \tag{2.82}$$

Making the substitution $e^2 = 4\pi\alpha$, where $\alpha = 1/137.036$, as well as

$\sin^2 {}_W = 0.233$ [30]

one finds the W and Z^0 masses given by:

$$m_W = \frac{37.3\ GeV/c^2}{\sin\theta_W} = 77.2 \pm 1.6\ GeV/c^2 \tag{2.83}$$

$$m_{Z^0} = \frac{37.3\ GeV/c^2}{\sin\theta_W \cos\theta_W} = 88.1 \pm 1.6\ GeV/c^2 \tag{2.84}$$

The width if the boson mass is determined from the sum of its partial widths from all possible decay channels. The bosons decay leptonically or hadronically. The hadronic channels are represented three times as frequently as a leptonic channel, since the quarks occur in three colors. The decay width and the branching ration BR are also dependent on the number of quark and lepton generations N_G, which are lighter than the boson. We assume that 6 light quarks and 6 light leptons exist in a total of 3 generations. This yields for the following for the W boson:

$$\Gamma(W \to e\bar{\nu}) = \frac{GM_W^3}{6\pi\sqrt{2}} = 208\ MeV/c^2 \tag{2.85}$$

$$\Gamma(W \to alle) = (N_G + 3N_G)\Gamma(e\bar{\nu}) = 2.5\ GeV/c^2 \tag{2.86}$$

$$BR(W \to l\bar{\nu}) = \frac{1}{4N_G} = \frac{1}{12} \tag{2.87}$$

For the Z^0 we find

$$\Gamma(Z^0 \to l^+l^-) = \frac{GM_{Z^0}^3}{12\pi\sqrt{2}} = 76\ MeV/c^2 \tag{(2.88)}$$

$$\begin{aligned}\Gamma(Z^0 \to alle) = {} & \Gamma(Z^0 \to l^+l^-)\{[1 + (1 - 4x^2)^2]N_l + 2N_\nu + \\ & 3[1 + (1 - \tfrac{8}{3}x^2)^2]N_u + 3[1 + (1 - \tfrac{4}{3}x^2)^2]N_d]\end{aligned} \tag{2.89}$$

$$= 2.5\ GeV/c^2 \tag{2.90}$$

$$BR(Z^0 \to l^+l^-) = \frac{1}{33.0} \tag{2.91}$$

where $x = \sin^2\theta_W = 0.2333$, and N_l, N_ν, N_u, and N_d are the numbers of generations of charged leptons, neutrinos, u-type and d-type quarks, respectively; here equal to 3 in each instance.

If one forms the ratio of boson masses one obtains a new parameter, which depends on the isospin of the gauge fields in which the Higgs boson was defined. It depends on the isospin of the Higgs particle:

$$\rho = \frac{m_W^2}{m_Z^2 \cos^2\theta_W} = \frac{1}{2}T_\phi \tag{2.92}$$

In our standard model $\rho = 1$. Once the mass of the gauge bosons has been experimentally determined the rho parameter can in turn be used to decide the structure of the Higgs sector. Any deviation of this parameter from 1 indicates that the isospin of the gauge fields was chosen wrongly and that the neutral and charged current are not of the same magnitude.

The weak interaction exhibits its A-V character not only in the case of the leptons, but also in the case of the quarks. Thus there are also 6 quarks in three generations in analogy to the 6 leptons in their three generations. It therefore seem reasonable to divide the quarks also into left-handed doublets and right-handed singlets. When calculating the hypercharge and the weak isospin for quarks, it is necessary to keep in mind that the quark charge is either 1/3 or 2/3. Furthermore, the left-handed d-type quarks do not appear in their pure mass states, the flavor eigenstates, but rather in mixtures. Only these mixed quarks are eigenstates of the weak isospin and the weak hypercharge. The relative weights of the components form the elements of the Kobayashi-Maskawa matrix [28, 31]. This matrix can be expanded according to four parameters; three of these parameters give the mixing angle, the fourth parameter is a phase which is responsible for the CP violation in the weak interaction of the hadrons. The results are:

$$\begin{pmatrix} \nu_e \\ e \end{pmatrix}_L, \begin{pmatrix} \nu_\mu \\ \mu \end{pmatrix}_L, \begin{pmatrix} \nu_\tau \\ \tau \end{pmatrix}_L \quad T = 1/2, Y = -1/2 \tag{2.93}$$

(2.94)

$$e_R, \mu_R, \tau_R \qquad T = 0, Y = 1$$

(2.95)

$$\begin{pmatrix} u \\ d' \end{pmatrix}_L, \begin{pmatrix} c \\ s' \end{pmatrix}_L, \begin{pmatrix} t \\ b' \end{pmatrix}_L \quad T = 1/2, Y = 1/6 \tag{2.96}$$

$$u_R, d_R, c_R, s_R, t_R, b_R \qquad T = 0, Y = Q \tag{2.97}$$

Not all the elements of the KM matrix are known today, since the mixtures are mostly small and therefore difficult to measure. Also, as of today, experimental verification of the heaviest quark, the top quark, is still lacking. Nevertheless, it is assumed that the generation subdivision of the leptons and quarks is of fundamental origin.

The standard model succeeds in providing a consistent description of the electroweak interaction of leptons and quarks:

- Quarks and leptons participate in identical manner in the electroweak interaction. They carry the quantum numbers for weak isospin and weak hypercharge.
- In addition to charged currents that couple to all particles with weak isospin, there are neutral currents that couple to all particles with weak hypercharge.
- If one ascribes the simplest mechanism to the spontaneous symmetry breaking, the result is that the neutral current and the charged current have the same strength ($\rho = 1$)
- Both currents consist of vector and axial vector components, with different proportional contributions in each case.
- The masses of the gauge bosons W and Z are predicted.

However, the standard model contains 18 free parameters, about whose origin and magnitude nothing can be said:

- 3 lepton masses: m_e, m_μ, m_τ,

- 6 quark masses: m_u, m_d, m_c, m_s, m_t, m_b,
- 4 parameters of the Kobayashi-Maskawa matrix,
- 3 coupling constants: e, g, and α_3,
- 2 potential parameters μ and λ for explaining the self-interaction of the gauge fields.

2.4 Production and Discovery of the Vector Bosons

In proton-antiproton collisions at a center-of-mass energy of several hundreds of GeV the quark structure of the nucleons becomes clearly evident. In highly inelastic collisions one quark of the proton and an antiquark of the antiproton can annihilate, not only via the strong interaction, but also due to the electroweak interaction. In this process a virtual photon is created which, in turn can decay into lepton pairs. Such a reaction is termed a Drell-Yan process [32], and is diagrammed in Fig.2.4.

Occasionally, in this annihilation process, a sufficient amount of center-of-mass energy is available to produce a vector boson weighing 100 GeV directly. An interference between the virtual photon and the Z^0 occurs. On the steeply decreasing mass spectrum of the produced lepton pair a resonance appears at the Z^0 mass. Fig. 2.5 shows this spectrum.

However, producing so large a mass requires almost the entire energy of the partons; hence the produced boson is almost at rest and may decay isotropically into new particles that fly off with high energies at angles up to 90^0 relative to the direction of the incident protons. The remaining quarks and gluons also react with each other. They form themselves anew and leave the interaction region at small angles to the direction of the incident hadrons.

Still, this simple picture does not yet give a complete description of the $q\bar{q}$ annihilation. If a more exact calculation is done with the aid of quantum chromodynamics, processes of higher order are also taken into account. The strongest correction is due to the process in which a gluon is radiated off in the initial state, as shown in Fig. 2.6. An additional small correction is caused by the quantum chromodynamics Compton effect. These higher-order processes explain the production of Z^o's with high transverse momenta. The theoretical distribution , in fact, predicts a large fraction of these at high values of p_t [34, 35].

Since the Z^o, exactly like the photon, couples to the charged fermions, it appears reasonable to discover the Z^o also in one of its fermionic decay channels. However, the reaction Zo → $q\bar{q}$ is very difficult to isolate experimentally, since the quarks do not appear as free particles. As soon as they are created they produce new $q\bar{q}$ pairs from the vacuum with which they then form themselves into a spatially distributed particle cascade. Such a jet is very difficult to separate from the background consisting of other jets which are produced as a result of the interactions of the other participating quarks ar the accompanying gluons. It is not possible to determine the jet masses with sufficient precision to be able to recognize the Z^o resonance peak on the continuum in the mass spectrum. Therefore we have selected the leptonic decay channels for detecting the Z^o. Here we make use of a double advantage:

1) The background to the reaction $Z^o \rightarrow l^+l^-$ is practically negligible, since other reactions in which high-energy leptons are produced are rare.
2) The kinematic parameters of the leptons, such as energy or momentum, as well as the angles of emission can be precisely determined. We can measure the invariant mass of the lepton pairs, and hence the mass of the Z^o with the required accuracy.

Fig. 2.1: The Fermi Ansatz and the New Three-Particle Interaction

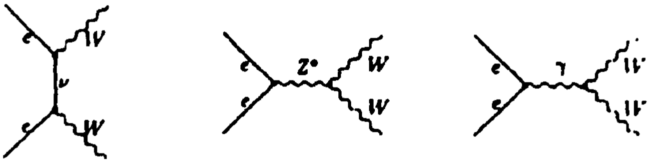

Fig. 2.2: On the Interference of the Z^0

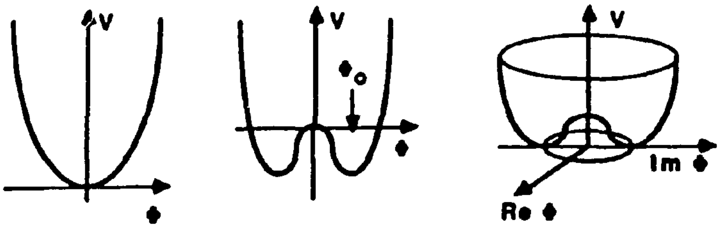

Fig. 2.3: Degenerate Vacuum Expectation Value with Spontaneous Symmetry Breaking

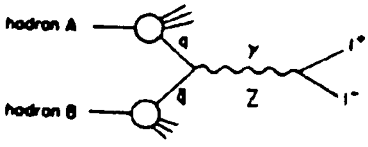

Fig. 2.4: The Lowest-Order Drell-Yan Process

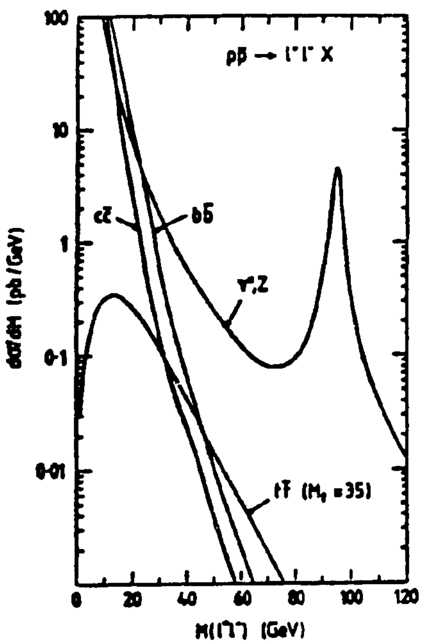

Fig. 2.5: Invariant Two-Lepton Mass in Proton-Antiproton Collisions

A comparison is made between the cross sections for the Drell-Yan process with exchange of a photon in interference with the Z^0, and the quantum chromodynamics production of heavy quarks, which then decay semi-leptonically. The center-of-mass energy amounts to $\sqrt{S}$ = 540 GeV. The resonance peak at the Z^0 mass is clearly recognizable on the continuum. The plot is taken from [33].

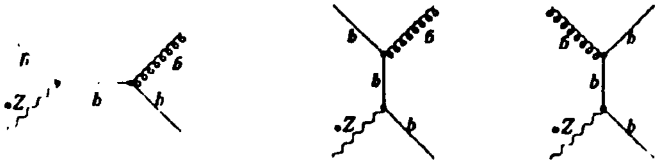

Fig. 2.6: Quantum Chromodynamics Corrections
to the First-Order Drell-Yan Process:

A gluon radiates off in the initial state and there is a quantum chromodynamics Compton effect.

	Fermion		T_3	Y	Q
Ⓑ	Leptonen				
Ⓒ	links-händ.	ν_e, ν_μ, ν_τ	+1/2	−1/2	0
		e^-, μ^-, τ^-	−1/2	−1/2	−1
Ⓓ	rechts-händ.	Ⓔ keine Neutrinos			
		e^-, μ^-, τ^-	0	−1	−1
	Quarks				
Ⓒ	links-händ.	u, c, t	+1/2	+1/6	+2/3
		d', s', b'	−1/2	+1/6	−1/3
Ⓓ	rechts-händ.	u, c, t	0	−2/3	−2/3
		d, s, b	0	−1/3	−1/3

A. Fermion
B. Leptons
C. Left-handed
D. Right-handed
E. No neutrinos

Table 2.1: The Electroweak Quantum Numbers of the Fermions

Ⓐ Kopplungskonstanten des Vektor- und Axialvektorstromes

Ⓑ Strom				
Ⓒ geladen	ν_e, ν_μ, ν_τ	e, μ, τ	u, c, t	d, s, b
g_V	1/2	1/2	1/2	1/2
g_A	1/2	−1/2	1/2	−1/2
neutral	ν_e, ν_μ, ν_τ	e, μ, τ	u, c, t	d, s, b
g_V	1/2	$-1/2 + 2x$	$1/2 - 4/3x$	$-1/2 + 2/3x$
g_A	1/2	−1/2	1/2	−1/2

A. Coupling Constants of the Vector and Axial Vector Current
B. Current
C. Charged

Table 2.2: Coupling Constants of the Vector and Axial Vector Current g_A and g_V ($x = \sin^2 \theta_W$)

Chapter 3

The Equipment

In the year 1976 it was recognized that the existing Super Proton Synchrotron (SPS) at CERN was a suitable machine for producing large center-of-mass energies [36]. Carlo Rubbia showed that it would be possible to convert this accelerator into a $p\bar{p}$ collision machine, which would then be in a position to achieve 500 GeV center-of-mass energy. This would suffice for the direct production of the heavy vector bosons. Eventually five proposals for experiments using this new storage ring were approved officially [37] and the construction of the facility was begun. The first beam collisions took place in 1981.

3.1 The Storage Ring Facility

Fig. 3.1 shows the arrangement of the individual components. In the proton synchrotron (PS) about 10^{13} protons are accelerated to an energy of 26 GeV and then directed onto a copper block, leading to the production of about 10^6 antiprotons. Every 2.4 s, the accumulator ring (AA) located downstream receives a packet of antiprotons with a momentum of 3.5 GeV/c. After a typical accumulation time of 24 hours about 10^{11} antiprotons are taken from the ring, directed back to the PS, there accelerated to 26 GeV, and then injected into the Super Proton Synchrotron (SPS). Shortly prior to that, protons of 26 GeV are produced in the PS and introduced into the SPS, moving in the direction opposite to that of the antiprotons. In the SPS both protons and antiprotons are then simultaneously accelerated to the final beam energy of 315 GeV each; they then remain in the ring for several hours. Since the beams are not homogeneous but consist of discrete packets called bunches, there are only three discrete positions along the ring at which the desired collisions occur, and these take place every 7.6 μs. The detectors are placed at these collision points. For the future it is proposed to work with double the number of bunches, and thus to halve the time between the collisions.

Dense antiproton bunches are required for achieving large luminosity. However, producing a large quantity of monoenergetic antiprotons is quite difficult since it appears to be necessary to satisfy apparently contradictory requirements. The antiproton accumulator needs to have large acceptance in order to collect as many particles as possible. This means that many particles with different momenta occupy a large volume; the phase space density is low. However the SPS requires large phase space density, in other words, small bundles of particles with sharply defined particle momenta. Thus it has a small acceptance. The required density enhancement in phase space by a factor of 10^9 is achieved in the AA by using the technique of stochastic cooling [38].

The Liouville Theorem forbids a compression in phase space by means of conservative forces, such as, for example, systems of electromagnetic lenses or mechanical constraints. Thus the overall phase space density in a packet of particles cannot be increased. It is useless to try to influence the packet as a whole; rather it is necessary to accelerate or slow down individual particles of the packet in a specific manner. It is possible to re-sort the particles in phase space so that after the re-sorting they will occupy different cells. In this manner the overall density in phase space remains the same, but it is increased locally. Roughly speaking, the occupied cells are carried toward the center, and the empty space towards the outside, so that the occupied part of the phase space falls within the acceptance of the SPS. To achieve this it is necessary to measure the momentum and location of individual particles and influence them in a specified manner. This is achieved in the AA with a sensor (pick-up) and a manipulator (kicker). The entropy reduction in the particle gas is more than compensated by the entropy increase that occurs due to the operation of the pick-up and the kicker [39]. Thus the Second Law of Thermodynamics is not violated. In this feed-back system the amplification is a critical parameter. If the amplification is too great, the stray effect of the kicker on the remaining gas particles is too great, and a heat-up results, in other words, an increase of the entropy rather than the desired cooling of the gas (see Fig. 3.2.) Thus the optimum amplification sets limits to the rate of cooling [40].

The pre-cooled particles are then bundled into a beam by means of an additional complicated process called stochastic collection [41]. Fig. 3.3 shows the particle density as function of the revolution frequency in the AA. It will be noted that there is a high density for a sharply limited revolution frequency (energy) in the center of the accumulated antiproton packet. By means of an elegant arrangement it is possible to cool the particles in the tail of the density distribution rapidly, but cool those in the center slowly. This results in the creation of dense antiproton bunches with low dispersion. Once a day about 30% of the particles are extracted from this beam and made available for the proton-antiproton collision experiments. The processes of stochastic cooling and collecting were primarily developed by Simon van der Meer, who received the Nobel Prize in physics for this work in 1984 together with Carlo Rubbia.

3.2 The UA1 Detector

The UA1 detector is located at one of the collision points, LSS5 (long straight section 5). An additional large experiment is placed at the next interaction point. This latter experiment was built by the UA2 Collaboration, and is also intended for the discovery of the intermediate vector bosons. However the UA2 does not possess the capability for finding muons.

The UA1 detector is a multi-function detection device. With this device it is possible to identify charged particles such as electrons and muons, as well as uncharged photons and pions, and even high-energy neutral neutrinos, and measure their momenta or their energies. More complex structures, such as jets, can also be measured.

Fig. 3.4 is a diagram of the detector. It consists of various detectors which are arranged around the point of interaction. Each detector component has a specific function to perform. Only by combining the many individual items of information is a complete description of the final state of a proton-antiproton collision, a so-called event, created later.

The central element is a 6 meter long cylindrical drift chamber with 2.2 m diameter, in which charged particles leave their track, and on the basis of which the momenta of the particles are determined. The central detector (CD) is surrounded by calorimeters in which the produced particles deposit their entire energy, which is then measured. The properties of the calorimeters are listed in Table 3.1. The electromagnetic calorimeters in the central region are called "gondolas" because of their shapes, those at the end-caps are called bouchons. These are used primarily for the identification of electrons and photons and neutral pions.

The CD and the electromagnetic calorimeters are surrounded by a coil which produces are largely homogeneous horizontal dipole field of 0.7 T perpendicular to the proton beam in the CD. The charged particles are deflected by this field. This makes it possible to measure the momenta of the charged particles. To shape the field, and for returning the magnetic flux, the coil is surrounded by an iron yoke. This yoke is instrumented with scintillators and photo-multipliers and serves as calorimeter for determining the energies of the hadrons. The hadron calorimeters in the central region are called C's, and those in the front regions are designated as I's.

Additional iron shielding has been placed behind the hadron calorimeters; this shielding was installed as an addition in order to improve the identification of the muons left over after passing through all the absorbers. This shielding is instrumented with several layers of Iarocci detectors, which are counting tubes that are operated in the limited streamer mode, which make it possible to follow the particle tracks through the iron. Thus the Iarocci chambers [46] help with the identification of the muons. These particles are identified using the outermost shell of the UA1 experiment, the muon chambers. Here the tracks of the muons are reconstructed in space, and appended to the tracks found in the central region by means of an extrapolation.

Before passing to a detailed description of the individual components of the detectors it would appear advisable to discuss the coordinate system used and the notation. The following conventions will be used from now on; they are shown in Fig. 3.5:

- The +x axis points in the direction of flight of the antiprotons.
- The +y axis points upward.
- The +z axis points in the direction of the magnetic field.

- θ measures the polar angle with respect to the x axis.
- η is the pseudo rapidity ($\eta = -\ln \tan\theta/2$).
- ϕ measures the angle in the y-z plane with respect to the +z axis.
- λ measures the angle out of the x-y plane.

3.2.1 The Central Detector

The CD is shown in Fig. 3.6. Its properties play a central role in the identification of muons; thus it is worthy of a detailed description. 6 large modules form the main part; surrounding the beam tube there are two additional chambers, the so-called green chambers. In each module there are planes of anode wires alternating with planes of cathode wires, between which the electrons and ions produced by the passage of a charged particle through the gas in the CD drift. The 4 forward modules each have 4 such drift volumes, in the central modules there are 10 drift volumes in each module. The green chambers each contain a single drift volume.

The planes are arranged horizontally in the forward modules and the green chambers, and vertically in the central modules. This configuration has the advantage that particles coming from the point of interaction, the so-called vertex, fly as parallel as possible to the planes, so that the drift direction of the electrons produced by these particles run mainly perpendicular to the path of the primary particles.

The width of a single drift volume is 18 cm. The field wires of the cathode planes aremaintained at a high voltage of -27 kV. Since the electrons produced drift with a speed of 5.3 cm/μs, the result is a maximum drift time of 3.6 μs, just short enough so that the chamber can completely record an event from the next-following beam intersection. Because of the strong B field, the paths of the electrons are inclined by 23^{o} relative to the direction of the E field. Surrounding the anode wires there are still other wires, lying at various voltages, that shape the electric field and compensate for the electrostatic forces that act on the anode wires. These wires are also used to check the gas amplification on the anodes.

The gas in the chambers consists of 60% ethane and 40% argon. When a charged particle passes through, the gas becomes ionized and the primary electrons so liberated wander towards the anode. In the immediate vicinity of the wires the electric field increases very strongly and accelerates the electrons to such a degree that they, in turn, are in a position to ionize the gas in the chamber. A charge avalanche is created which produces a brief charge pulse on the anodes. The time from the beam intersection until the pulse arrives is measured and recorded. By this means a spatial resolution of 250 - 300 μm is achieved. The position along the wire can be measured by means of a comparison of the amount of charge arriving at the two ends of the wire. For this measurement the spatial resolution is dependent on the anode wire length, which varies in the chambers, and amounts to about 1.7% of the length of the wire, typically several cm.

The time and the charge measurements are digitalized, processed by a read-out processor that suppresses the null measurements, and then passed on to the UA1 read-out system. This reduces the amount of data from an original value of about 2 M-bytes per event to about 100 k-bytes. An additional capability of the read-out processor is the recognition of overlapping pulses, which can then in most cases be disassembled into their component original pulses. This makes it possible to separate even tracks that lie very close together. The resolving power for double tracks is typically about 5 mm; without this capability it would be 1.5 cm.

The technique for track reconstruction from the raw data will be described in a separate chapter. It yields criteria for selecting well-measured tracks, which form the basis for reliable selection of muon events.

3.2.2 The Electromagnetic Calorimeters

The electromagnetic calorimeters initially play a subordinate role in the investigation of muon events. They are, however, important if one studies jets or wishes to have information about the energy flux in the event.

The gondolas cover the central region. This corresponds to a pseudorapidity interval of $\Delta\eta = 1.5$ or ± 65°. A total of 48 modules cover the lateral surfaces of the CD. They have a thickness of 22.5 cm, and consist of a sandwich of 1.2 mm thick lead foils and 1.5 mm of scintillator material. Fig. 3.7 shows the arrangement. The longitudinal development of an electromagnetic shower is measured in four so-called samplers which have thicknesses of 3.3, 6.6, 9.9, and 3.3 radiation lengths. With a total thickness of 26.3 radiation lengths essentially every electromagnetic shower is completely absorbed.

The gondolas are read out by photo-multipliers via BBQ wave-length shifters. At each of the four corner points of a given sampler there is one such read-out, so that from a comparison of the signals at the corners it is possible to determine the location where the shower passed through. Making use of the energy profiles in the four samplings it is possible to identify electrons and photons. At the start of data collection the energy resolution of the gondolas amounted to:

$$\sigma_E/E = 15\,\%\,/\sqrt{E}\ \ (E \text{ in GeV}). \tag{3.1}$$

At this time, this energy resolution has decreased by about 22%
due to aging effects as a result of the irradiation. The spatial resolution by signal comparison comes out to be:

$$\sigma_z = 6.3\ cm\,/\sqrt{E}\ \ (E\ in\ GeV). \tag{3.2}$$

Since the gondolas cover an angle of nearly 180°, it is important to achieve good angular resolution by signal comparison. It amounts to:

$$\sigma_\phi = 0.24\ rad\,/\sqrt{E}\ \ (E\ in\ GeV). \tag{3.3}$$

In the case several electrons or jets are incident on one gondola, ambiguities do arise.

The bouchons have a similar longitudinal structure as the gondolas. Since, however, they are positioned in the front region their segmentation in ϕ is different. They cover an interval in the pseudo-rapidity connected to that of the gondolas and extending to $\eta = 3.0$, and are subdivided into 32 segments in the shape of sectors of circles. The samplers in this case are composed of layers of 4 mm of lead and 6 mm of scintillator, and are read out on their outer corners. The light collectors have a attenuation length of 80 cm, so that the light collected by the photo-multiplier is proportional to the transverse energy.

$$E_t = E \cdot \sin\theta \tag{3.4}$$

In order to obtain exact information about the energy deposited by a shower, the bouchons also contain a position detector consisting of proportional tubes; this allows a spatial determination with a precision of $\sigma_x = \pm 2$ mm.

Further along the forward direction there are still other calorimeters, the Calcomp, the "Forward" and the "Very Forward" calorimeters. The Calcomp has a special significance. In it the influence of the main magnetic field of the circulating proton and antiproton beams is compensated, since it induces into the beam tube a strong B field in the direction opposite to that of the central magnetic field.

3.2.3 The Hadron Calorimeters

Fig. 3.8 shows the structure of one of the 16 modules which, because of their shape, are simply called C 's. The module is divided into 12 sections. Each section, in turn, consists of two samplers, the so-called front stack and back stack, each with a thickness of 2.5 interaction lengths. The sampler is a sandwich made of iron plates 5 cm thick, each followed by 1 cm of scintillator material, which is observed by two photo-multipliers. The energy resolution of the hadron calorimeters was measured to be

$$\sigma_E/E = 80\ \%\ /\sqrt{E}\ \ (E \text{ in } GeV). \tag{3.5}$$

The angular acceptance of the C's is the same as that of the gondolas.

The hadron calorimeters at the front faces, simply called I's because of their shape, are very similar to the C's. Per front face there are 6 modules with 6 sections each, consisting of 2 samplers. The sections which are closest to the beam tube are further divided into 4 sub-divisions. Their sample thickness amounts to 3.3 interaction lengths, and their energy resolution is the same as that of the C's. The solid angle coverage of the I's corresponds to that of the bouchons. Again, there are additional hadron calorimeters in the regions of relatively large rapidity.

When performing muon analysis the energy content of the back stacks was used for verification of a muon candidate. It was required that the energy of a minimum-ionizing particle be deposited in the back stack.

3.3 The Muon Detector

The outermost shell of the UA1 detector is formed by the muon detector (see Fig. 3.9). In the ideal case only muons can penetrate that far, since the muons feel only the weak and electromagnetic interactions. Thus they do not lose their energy in the iron calorimeters by producing a hadronic shower. Since the critical energy for muons amounts to almost one TeV, they also do not produce electromagnetic showers. They lose only the energy of a minimum-ionizing particle, in other words, just a few GeV. Nevertheless, because of their charge they can be detected in the muon detector, after they have left the calorimeters. This detection device does not only operate passively, but rather it is also in a position to recognize a muon track in the detector within 4 μs. We can thus trigger for muons without dead-time.The muon detector consists of a total of 58 drift chambers, which are grouped into 34 modules and cover an area of more than 500 m^2. Each chamber measures about 4 m x 6 m and contains four layers of drift tubes in two orthogonal double planes. In each plane the drift tubes, which are 15 cm wide and 4.5 cm high, are placed adjacent to one another. The planes are relatively displaced by one half tube width in order to avoid ambiguities in track reconstruction. A second chamber is placed 62 cm distant, so that in every projection a muon will hit at least 3 drift tubes. Fig. 3.10 shows the arrangement. The chambers in the floor region (bottom) are constructed somewhat differently; in this region four layers of drift tubes are arranged in parallel, but the tubes are read from both ends. The coordinate along the wires is obtained by comparing the signals at the two ends. From the time difference of the two signals the length coordinate along the anode wire may be obtained since the signal spreading rate along the wire is known.

Fig. 3.11 shows a cross section through a drift tube. The diagram also shows the electric field lines that reach the anode, in other words, the sensitive volume. The anode wire, made of stainless steel 50 μm thick, is clamped firmly in a PVC holder. The cathodes and the field shaping cathodes are inserted in a PVC fitting, which is inserted into the tube body made of extruded aluminum. The selected geometry and the electric voltages are optimized for the gas mixture in the tube. This optimization had to satisfy a number of requirements:

- The gas used should be the same as in the central detector, i.e. 40% argon and 60% ethane.

- The electric field strength should everywhere be greater than 0.5 kV/cm, so as to achieve as uniform as possible a drift speed of 50 μm/ns.

- The maximum drift time should not exceed 2 μs so that the drift information can be used to make a trigger decision before the next beam crossing.

- The thickness of the sensitive region should everywhere be large enough so that sufficiently many primary electrons will reach the anode.

- The sensitive volume should remain narrow enough so that the spatial resolution for particles entering in a skew direction will not become too bad.

The properties of the drift tube were established using a pion beam [47, 48]. For a particle incidence angle of up to 40^0 an individual tube measures to better than 0.5 mm. Once a chamber consisting of many tubes has been cemented together the relative precision with respect to reference points attached to the outside of the chamber is still better than 1 mm. Even after the chambers have been assembled into modules and hung in their racks, a track in two chambers can be determined with similar precision. It is difficult, however, to fit the tracks to those from the rest of the UA1 detector. The other components are not precisely enough aligned to the muon detector to achieve a precision of better than several mm in defining a combined muon track in space. In the chapters dealing with track reconstruction and the calibration using cosmic rays, this subject will be taken up in more detail.

The anode wire signals are acquired using current-sensitive preamplifiers [49] that are capacitively coupled to the wires. The equivalent threshold of the amplifier is 150 μV. This low signal amplitude has two reasons: First, the drift tubes are operated at the upper end of the proportional region, thus the gas amplification at the wire is only moderate; second, at the narrowest place the sensitive volume is only a few mm thick, so in the primary ionization only about 20 electrons are produced. After preamplification the signals are converted into digital pulses and are fed to the time digitizers in a balanced fashion through twisted-pair cables. Each of the approximately 7000 tubes is connected to one channel of the MTDs (multiple time digitizers) [136], which are capable of digitalizing several pulses from a tube with an accuracy of 6 ns over a time window of 2 μs. The digitizers are then read via a REMUS bus [137]. The data processing system is described in more detail in

Appendix A. Ahead of the MTDs are high-impedance signal channels that feed the pulses from the muon chambers to the fast muon trigger "FT" (FT = fast trigger).

3.4 The Muon Trigger

In normal operation a beam crossing happens in the UA1 detector every 4 μs.[1] Each such collision may produce interesting interactions. However the events searched after by UA1, which are described in my work, are extremely rare; in most cases the end state does not interest us. The UA1 trigger system makes a preselection of the events [50].

The trigger system has only 4 μs to make its decision, but, depending on the luminosity it must achieve a reduction of the event rate from 10^3 to 10^4, in order for enough time to be available to write the characteristics of the collisions of interest to us on a magnetic tape completely. In addition to the muon trigger there are also other triggers, such as an electron trigger and various jet triggers, as well as a so-called minimum-bias trigger. The latter forms the basis for all the further triggers; it tells us that an inelastic interaction has indeed taken place in a proton-antiproton collision. Furthermore it is capable of suppressing undesired events, such as collisions between incident particles with gas atoms in the beam tube. By combining this trigger with the muon trigger it helps to reject the background due to cosmic-ray muons. The minimum-bias trigger is also referred to as the pre-trigger.

Symmetrically along both front sides of the detector there are scintillator hodoscopes in an angular region from 0.6° to 25° from the beam axis. A

---

[1] This value holds for operation with 6 bunches. However, up to now we have operated with a maximum of 3 bunches; this increases the time between crossings to 7.6 μs.

coincidence signal from these hodoscopes activates the pre-trigger if it arrives synchronously with the moment of beam crossing plus the time of flight of a particle from the interaction point to the hodoscope (see Fig. 3.12).

If no pre-trigger is present, all the other triggers are ignored by the central trigger processor. If, for example, in addition to the pre-trigger the muon trigger triggers, all the UA1 detectors are kept on and the event is read out. Otherwise, or when this read-out has been completed, the detectors are released again. At a luminosity of $L = 10^{29}$ $cm^{-2}s^{-1}$, the pre-trigger rate is about 3.75 kHz; about four events per second are written on magnetic tape. Table 3.2 contains a summary of the trigger rates with muons.

The muon trigger [50] performs a simple track recognition. First the orthogonal projections from the drift chambers are individually examined, then track candidates from these projections are combined into a track in space. If this track points to the interaction point (briefly called the "vertex") within an angle of about 200 milli-rad, then a muon event has been found, and the FT activates. The basis for track recognition is the pattern of the drift tubes that registered hits. The muon trigger cannot make its yes/no decision until the maximum drift time of 1.5 μs has passed. For each hit tube an individual bit is placed in a buffer memory. The drift time, which would allow a considerably more precise determination of the location where a particle has passed through the detector, is not utilized here, since the electronics expenditure to do so would be too large, and a calculation of the track parameters could not be carried out by a microprocessor within just a few μs.

Inside a projection the tubes of the innermost layer are designated as reference tubes. Nine additional tubes are associated with each reference tube, so that the entire configuration point to the vertex [52]. For each reference tube individually all the combination of other tubes are selected that correspond to an allowed track. The ten signals from the tubes form one address of a 1024 x 1 bit memory, which is freely programmable, and in which the allowed patterns are stored.

Various memory sets may be loaded, that point to the vertex more or less precisely. Making too sharp a track definition on the basis of the tubes does not make sense, since due to multiple scattering in the absorbers, and due to magnetic deflection the muons do not come in a straight line from the point of collision. Furthermore, the vertex can vary by 30 cm along the beam. Fig. 3.13 shows the schematic of the track logic.

The results of single projections are now combined and gathered by zones. The zones are so designed that they correspond to a projection of the hadron calorimeter blocks lying in front of them onto the chambers. The FT signal from a given zone is brought into coincidence with the signa of the hadron calorimeters that fire as soon as a minimum-ionization particle has passed through them. Fig. 3.14 shows the schematic.

The sensitive time of the calorimeter amounts to only 200 ns, in contrast to the 2 μs of the muon chambers. The coincidence suppresses the background stemming from cosmic-ray muons. This reduction is, of course, strongly dependent on the location and on the direction from the vertex; a careful investigation of this effect was meantime undertaken by M. Preischl in a Diploma Thesis [53]. Fig. 3.15 shows the angular resolution of the FT for various pre-stored decision patterns.

In order not to exceed a given maximum value of the trigger rate, which is set by the writing speed of the magnetic tape unit, as the luminosity increases, it is possible to reduce the active area of the FT in the front regions (see Fig. 3.16). This requires auxiliary cards that see only a part of the detector area. It is possible to assign to each of the four muon triggers (namely the inclusive muon trigger, the muon-jet trigger, the muon-electron trigger, and the two-muon trigger) one each of four areas of different sizes (called EA, EB, EC, and FT). Fig. 3.17 shows the rapidity coverage of the trigger regions.

In order to achieve a further reduction of the event rate we have installed a second trigger stage. After the events have passed through the read-out system they are brought to 5 additional computers of the type 168E. These machines emulate the central processors of IBM 168 Computers. In the first stage external points in the muon detector at which a muon track is suspected on the basis of several hits, are tracked down; this algorithm (MUTUBE [58]) is independent of the FT. If two or more activities are recognized the event is written out in any case, since this is a candidate for a two-muon event. If a single external point is found, it causes a very much simplified track reconstruction in the central detector, which is limited in the x-y plane to a region around a straight line from the external point to the vertex. In the 1985 period a new algorithm was introduced which examines the quality of the muon detector track more closely (MUTIME [57]). To this end the track is first reconstructed with full resolution in the muon unit. In both projections the spatial displacement of the track that was found is then compared with the theoretical track of a muon with 45 GeV/c transverse momentum. In effect one thus achieves a cut on the transverse momentum of the muons p_t^μ. The lower the muon momentum is, the greater will be the displacement of the track due to multiple scattering and deflection in the magnetic field. If the displacement exceeds a minimum value, which was determined for a mesh of points on the muon detector by simulation calculations, by a factor of 8 or more, the event is rejected. The maximum value is a critical parameter which was established in such a way that muons with $p_t^\mu > 5$ GeV/c are 100% included, while muons with $p_t^\mu < 5$ GeV/c are effectively suppressed. Fig. 3.18 shows the dependence of the suppression factor and the efficiency on the transverse momentum [59].

3.5 Track Reconstruction

The reconstruction of the particle tracks takes place in several stages: First the various raw data from the individual detectors are transformed to a standardized data format. One tries to translate the measured values as quickly as possible into physical parameters of the particle candidates, such as, for example, momentum, energy, and charge. It is necessary to input the calibration constants of the detectors, which are stored in an external data bank, into the reconstruction calculation. In the case of the calorimeter signals the zero level is subtracted and the amount of deposited energy is then determined with the aid of a transformation factor. In the case of the drift chamber detectors, the drift times must be corrected for the exact point in time of the event and for the non-linear place-time relation. Then the particle tracks in the sub-detectors can be precisely reconstructed. In another step these data are combined, and used to identify the particle.

3.5.1 Track reconstruction in the Central Detector

To be as independent of calibration constants as possible one begins inside the drift volumes by finding track candidates, by searching for small chains of associated tracks. The chains, once found, are then combined into track candidates in the entire central detector, taking drift velocity and drift angle into account, and using the internal calibration constants, which are determined anew on a daily basis. Thereupon one performs a circle fit in the x-y plane, and eliminates hits that lie more than four standard deviations away from the fit. Additionally, one uses the measured z-coordinate of the points and makes a helix fit in space. All tracks whose distance from the beam axis is less than about $\approx$ 200 mm are used to fit the vertex in the x-y plane. All tracks that terminate less than three standard deviations from the vertex are designated as associated, and for these the helix fit is repeated making use of the vertex as additional point. At the end the goodness of a track is derived from two χ^2 values:

- χ_z^2 is the normalized sum of the squares of the distances in the z-coordinate.

- χ_{xy}^2 is the normalized sum of the squares of the distances in the x-y plane

Instead of χ_{xy}^2 we use the derived quantity χ_s^2 :

$$\chi_s^2 = \sqrt{2\chi_{xy}^2} - \sqrt{2N-1} \tag{3.6}$$

N designates the number of degrees of freedom in the x-y fit. For large N this variable has normal distribution with variance 1 and mean value 0, if the measurement errors are correctly described. χ_s^2 is not only a measure for the goodness of the track fit, but it also yields a test of the hypothesis that the track was really caused by a <u>single</u> particle. Reconstruction problems due to overlapping tracks usually lead to bad χ_s^2 values. Two pieces of track caused by the decay of a particle in flight, and which the track reconstruction program has erroneously fitted together into a single track may be recognized in some cases by a cut on χ_s^2.

3.5.2 Track Reconstruction in the Muon Detector

In the first reconstruction stage the raw data obtained is first re-coordinated and sorted. The we correct the drift times by a time difference, the difference by which the zero point of the drift time spectrum of a tube is displaced relative to the zero point of the sensitive time window of the time digitizer. Then the points of penetration of the muon through the individual tubes are transformed from the raw drift times using a linear place-time relation. Unfortunately the design of the drift tubes yields an ambiguity in the reconstruction, since it is initially not clear whether a particle flew by to the left or the right of the anode wire. Thus a muon that passes through a projection of four layers produces a maximum of 8 measured points.

Then begins the track reconstruction separately in each projection. By combinatorial analysis one tries to find all candidates for which four measured points lie within a band 6 mm wide, which makes at most an angle of 60^{0} relative to the perpendicular to the chamber. After the angle of incidence has been determined, the drift times can be corrected in an angle-dependent and drift-time-dependent fashion; then a straight-line fit is made to the points used. The points, once used, are no longer available for the next search. The next search then looks for tracks with only three points; these are also allowed, since there are dead spaces between the tubes and the tubes are not 100% sensitive. In the last step the tracks from the two projections are combined into tracks in space. All possible combinations are stored, as well as the quality of the tracks expressed as a χ^2.

3.5.3 The Method of Combined Momentum Fits

We can make use of the good precision of the track reconstruction in the muon detector to improve the momentum measurement of the muons. For this purpose use is made of the deflection of the muons in the iron absorber. Two effects play a role, if the momentum of the muon is to be measured a second time outside the central detector:

a) On the one hand, an additional magnetic field must be traversed to achieve a bending of the track. For this purpose we use the hadron calorimeters in which the magnetic field of our dipole field is returned. In addition, the external absorber walls in the lateral region are magnetized, where we suffer most from poor central detector measurement. After leaving the iron the tracks have received a defined deflection.

b) On the other hand, the muons undergo multiple electromagnetic scattering as they pass through the magnet yoke and the external absorber. The magnitude of this scattering is inversely proportional to the momentum of the muon, and occurs incidentally. As a result of the scattering statistically fluctuating angular deflections and displacements are observed when the muon leaves the absorber.

Important information is obtained when one uses the Iarocci chambers, which make it possible to follow the track through the external absorber. For 1985 these measurements are included in the fit. If one compares the angle of the track and the total displacement at the entrance of the muon into the external field, and at its exit from it, then a fit may be applied to determine the momentum of the muon[2] [113]. (See Fig. 3.19.)

The defined deflection can be pretty well separated from the statistical deflection. At small momenta the precision of the method is dominated by the strong multiple scattering, so that there no improvement over the exact measurement in the central detector is possible. However, for large momenta the method leads to a more precise determination of the muon momentum. Since the shape of the external field is complicated in some regions of the detector, and since its strength could not be measured everywhere, this procedure must be calibrated using cosmic-ray muons. So far we have applied this method only to the data from 1984 on, since in the period before that time no additional absorber had been installed.

The good behavior of the combined momentum fit becomes apparent when one considers the so-called "stretch" function s, which provides a measure for the agreement between the momentum measurement in the central detector and the calculation using the combined method:

$$s = \frac{1/p_{CD} - 1/p_{OMF}}{\sigma_a} \tag{3.7}$$

$$\sigma_a = \sqrt{\sigma^2(1/p_{CD}) - \sigma^2(1/p_{OMF})} \tag{3.8}$$

The parameter σ_a gives the weight assigned to the additional information from the muon detector and the Iarocci chambers in the combined fit. Fig. 3.20 shows the "stretch" function for 77 muon tracks from identified W and Z^0 decays. The distribution is compatible with a Gaussian curve with width 1.

The following may be said concerning this procedure:

---

[2] This procedure is also called OMF, for short, which stands for "overall momentum fit".

1) The momentum measurements with the central detector alone and with the combined momentum fit are correlated; the measurements agree within the statistical errors.

2) The errors in 1/p are reduced by about 20%.

3.6 The Reconstruction of Jets and Neutrinos

A jet is never as clearly defined as a single particle, since it is composed of both charged and uncharged components, which arise from the fragmentation of quarks or gluons. We therefore attempt in the UA1 to define a jet starting with the topology of the energy flux. By a jet we mean a configuration in which a concentrated energy bundle is emitted into a limited solid angle. To measure the jet energy we assign to the center of each calorimeter cell a direction vector from the vertex, whose length is given by the energy content of the cell. We thus define energy vectors. We then sum together those vectors that lie close together (see Fig. 3.21).

The precision of the direction measurement of the jet is limited by the granularity of our calorimeters. If several adjacent calorimeter cells indicate energy, we assume that a jet exists there. In the proton-antiproton collisions in our energy range we observe the inelastic collision of the partons in the nucleons. The collision partners carry only a part of the nucleon momentum, which is expressed by the structure functions. Hence the partons in the nucleon in general will have a different momentum than those in the antinucleon. From the conservation of momentum it follows that this difference can also be observed after the collision. In other words, the products of the reaction have experienced a certain Lorentz boost along the beam axis. In particular, the particle density distribution, expressed in spherical coordinates, is no longer constant. However, for a sensible jet definition one requires a coordinate system in which the particle density is everywhere the same. Such a system is set up using the angle ϕ and the rapidity y of a particle, where at high energies we neglect the particle mass and use, as an approximation, the pseudorapidity η.

$$y = \frac{1}{2}\ln\left(\frac{E+p_l}{E-p_l}\right) \tag{3.9}$$

$$\eta = \ln\left(\cot\frac{\theta}{2}\right) \tag{3.10}$$

As the three-dimensional distance in space between two particles we then define:

$$\Delta R = \sqrt{\Delta\eta^2 + \Delta\phi^2} \tag{3.11}$$

In a normal event without jets fluctuations may arise that produce a local energy concentration, without, however, a jet being present. We thereforeadd a definition of an initiator for a jet $E_{t,Init}^{thr}$ for a jet, in other words, a leading particle of a certain minimum energy around which we then sum the energies in the neighboring cells above a threshold E_t^{thr}, up to a maximum distance R^{max}. In forming the sum one begins with the summation at the largest initiator. The following values are used:

- $\Delta R^{max} = 1.0$
- $E_{t,jet}^{thr} = 1.5\ GeV$
- $E_t^{thr} = 100\ MeV$.

In a similar manner it is possible to sum the momentum vectors from the central detector; we therefore will briefly distinguish between the calorimeter jets and the CD (central detector) jets. The measurement in the CD has the disadvantage that no neutral particles can be observed; however the two methods of measurement complement each other in a very clever way. Both the calorimeter and the CD suffer from acceptance losses. But, due to the geometry, the losses are complementary; the CD has its best acceptance in the poor calorimeter regions, and vice versa. Nevertheless, the UA1 jet algorithm makes use only of the calorimeter information.

In contrast to the longitudinal motion, the transverse momentum is very small prior to the collision. If we assume that the transverse momentum sum vanishes prior to the collision, we would expect, due to the conservation of momentum, that after the collision the sum of the transverse momenta is still 0. If a neutrino is produced in our machine, perhaps in the decay of a W boson into a muon and a neutrino, the neutrino can escape undetected, since its interaction length is so very large that a reaction in the calorimeter is very improbable. It carries its energy away from the event unseen. This creates a visible energy imbalance that we designate as "missing transverse energy." If the missing transverse energy is distinctly different from zero, then this is a certain indication for a neutrino.

The UA1 detector is capable of measuring the energy flux down to an angle of 0.2^{0} relative to the beam axis. We sum the transverse energy vectors, as they have already been defined for the case of jet reconstruction, over the entire detector. Unfortunately the gaps between the calorimeters are so big that it is necessary to correct for the energy loss through these gaps. Because of the fluctuations in the calorimeter measurements it is possible for small amounts of energy to be apparently missing, where this is not in fact the case. Such apparent but unreal energy losses have a negative impact on the significance of the neutrino measurement. It turned out that the relative precision in determining the missing energy becomes better as the total transverse energy deposited in the detector, in other words the scalar sum of the transverse energy, increases. We have:

$$\Delta E_t^{miss} = 0.7 \times \sqrt{\sum E_t} \; (E_t \text{ in GeV}) \tag{3.12}$$

Thus the typical error is only a few GeV. Fig. 3.22 shows the result of the measurements.

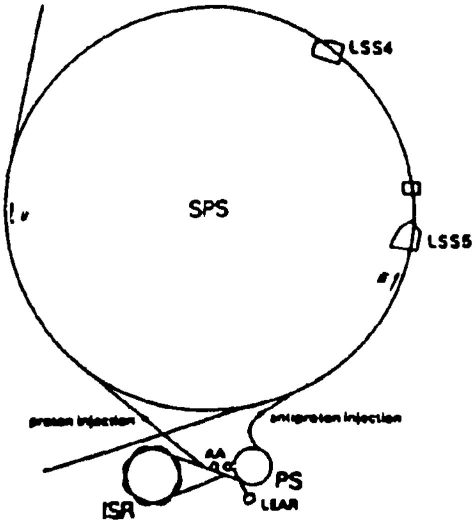

Fig. 3.1: The CERN Storage Ring Facility SPPS

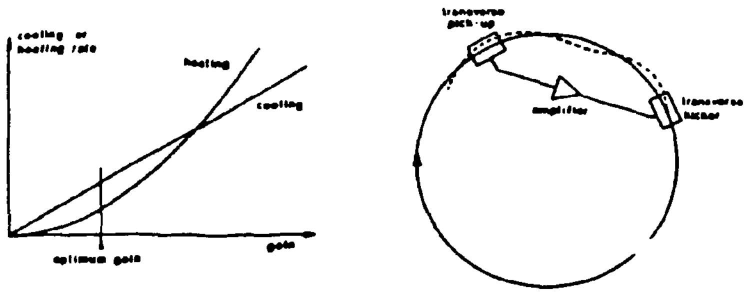

Fig. 3.2 On the Optimum Cooling Rate

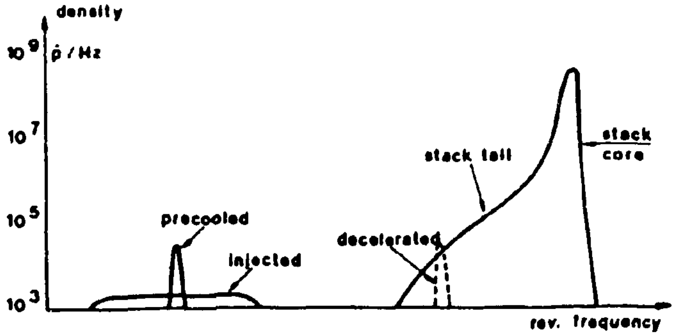

Fig. 3.3: The Particle Density in the AA as Function of the Frequency

A proton packet injected with low revolution frequency is initially pre-cooled, and this creates a bundle with sharply peaked frequency, which is to say that all the particles in the bundle have about the same speed. After pre-cooling this packet is slowed down and mixed into the collected "stack" which is revolving at higher frequency. In the stack the particles in the tail of the distribution are then cooled faster than those in the center. By applying this procedure repeatedly an intensive "stack core" of well-cooled antiprotons is created.

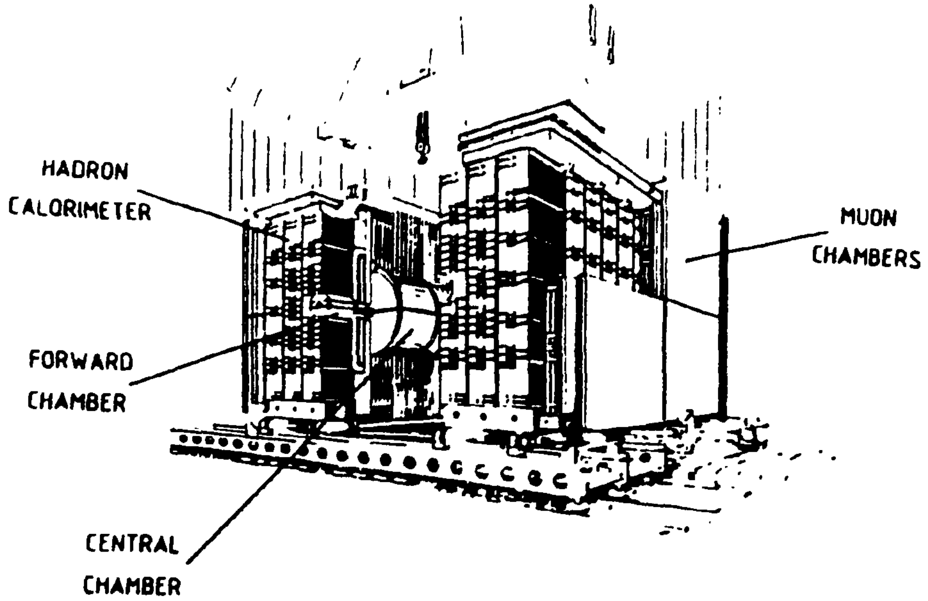

Fig. 3.4: The UA1 Detector

The central drift chamber lies in a dipole magnetic field of 0.7 T. The muon chambers in the forward direction are omitted for reasons of clarity.

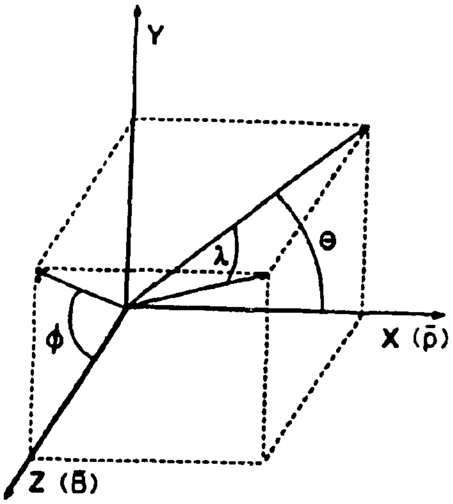

Fig. 3.5: The Coordinate System Used

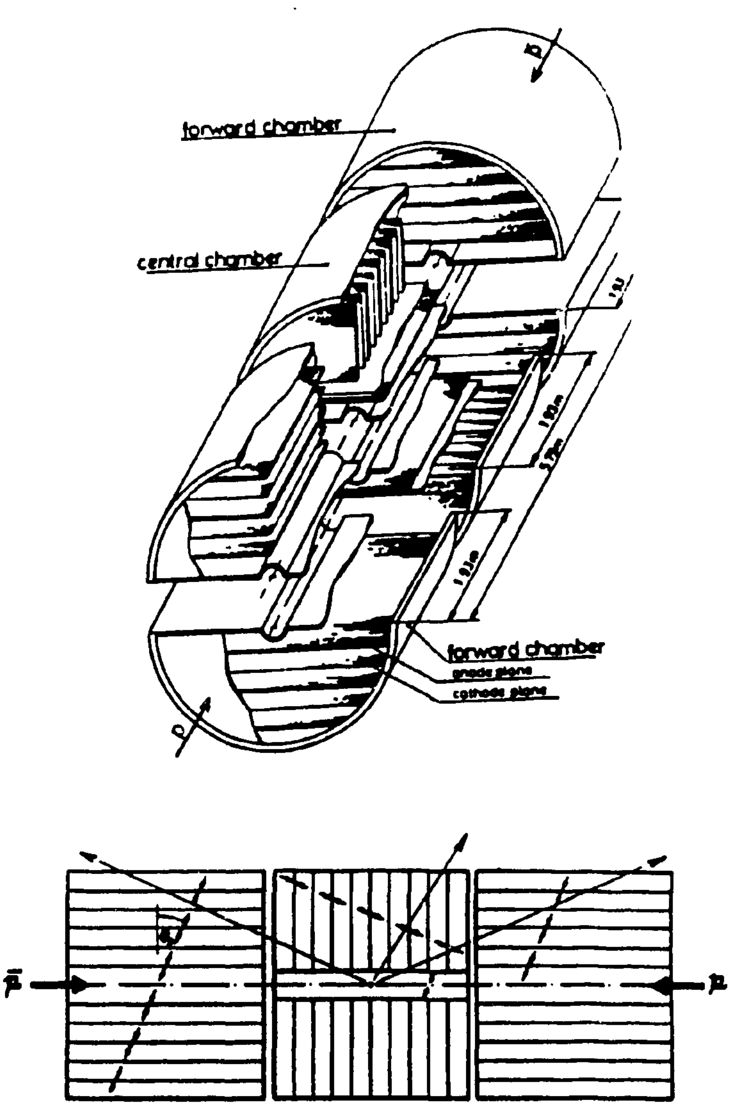

Fig. 3.6: The Central Detector

The upper picture shows an exploded view. The lower diagram shows a lateral view in which two particle tracks and the drift directions under the influence of the electric and magnetic fields are drawn in.

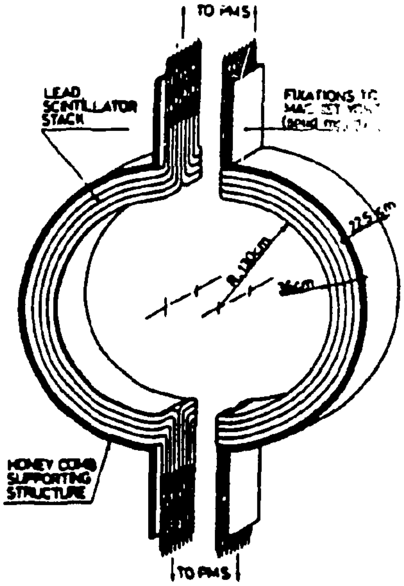

Fig. 3.7: Two Elements of the Central Electromagnetic Calorimeter

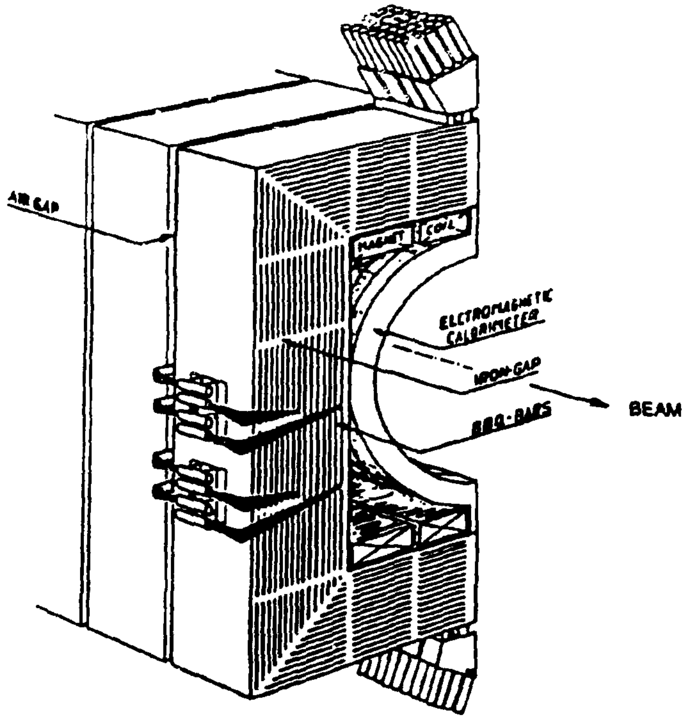

Fig. 3.8: One Element of the Central Calorimeter

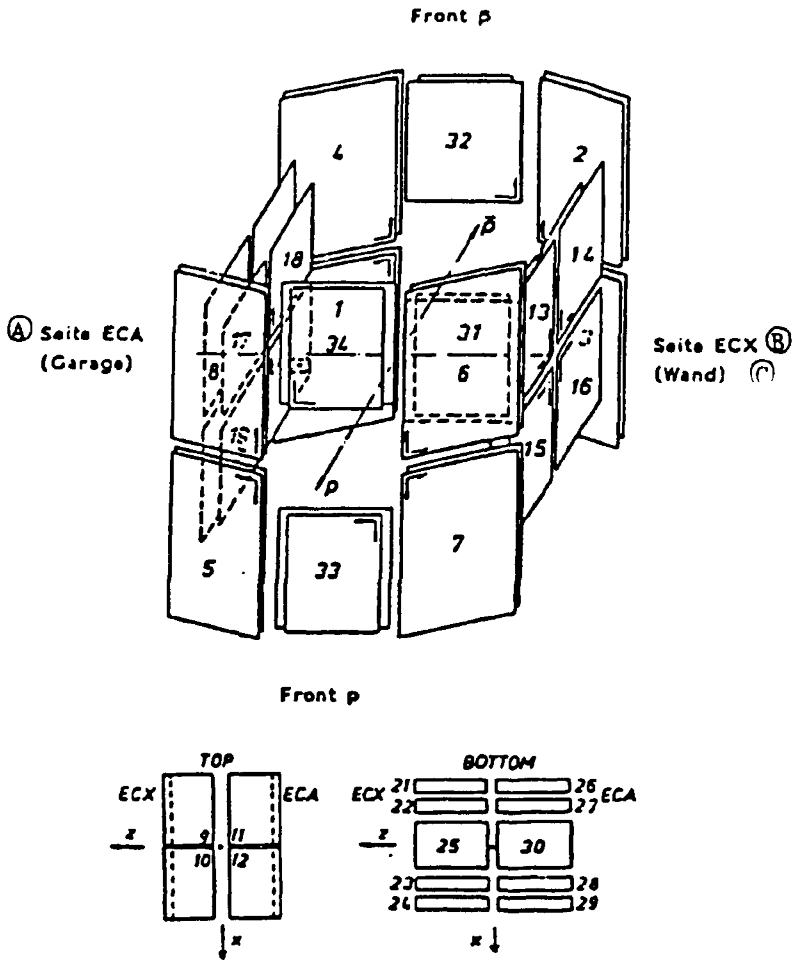

A. ECA side
B. ECX side
C. (wall)

Fig. 3.9: The Arrangement of the Drift Chambers of the Muon Detector Since 1985

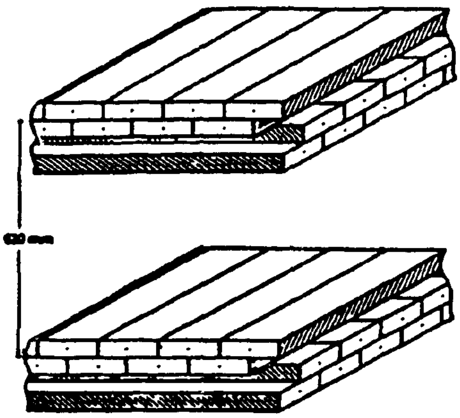

Fig. 3.10: Schematic Design of a Muon Chamber

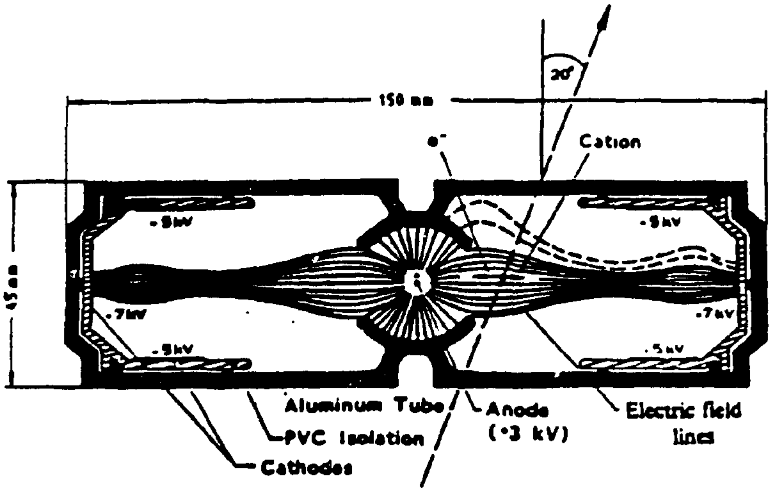

Fig. 3.11: Cross Section Through a Drift Tube of the Muon Detector

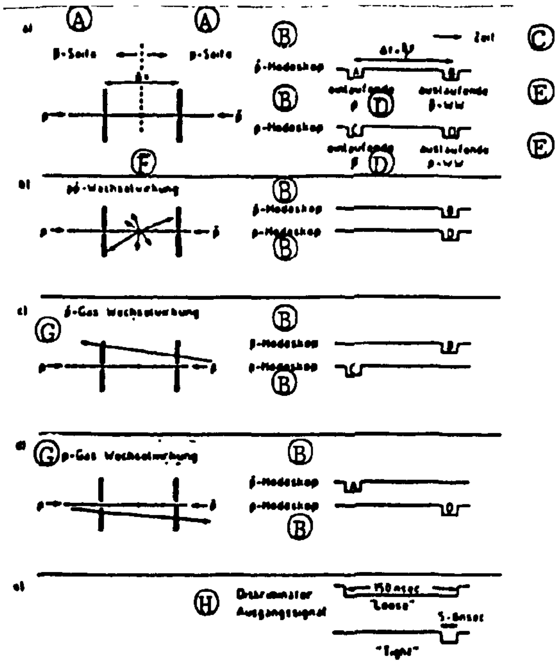

A. _side
B. _ modoscope
C. time
D. entering
E. exiting
F. interaction
G. gas interaction
H. discriminator
output signal

Fig. 3.12: On the Trigger Logic

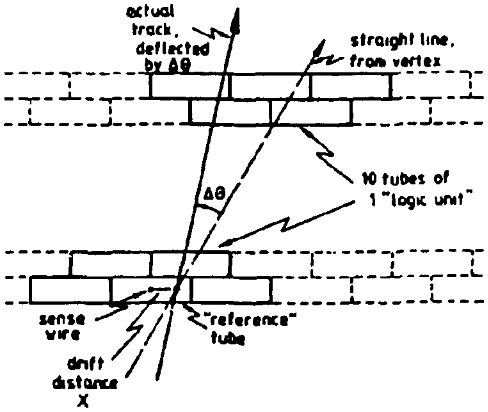

Fig. 3.13: The Grouping of Tubes for Defining a Muon Trigger

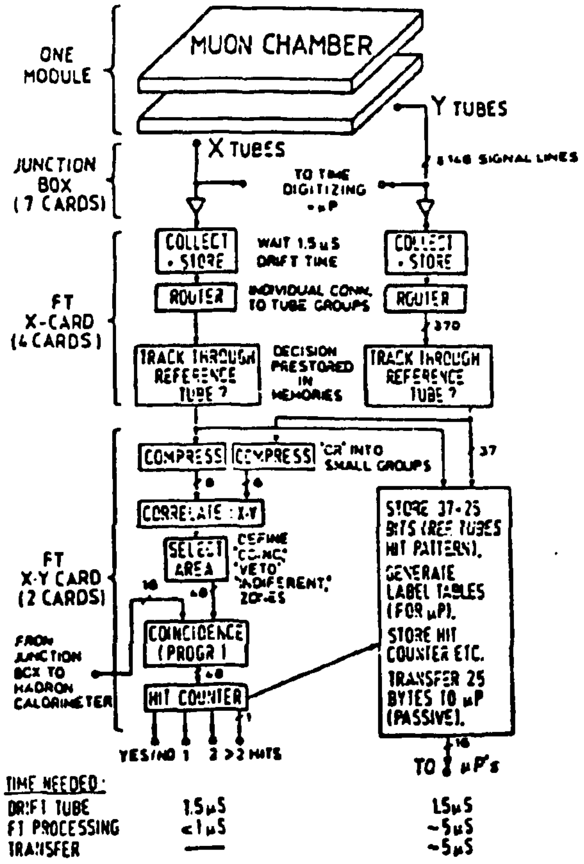

Fig. 3.14: Block Diagram of the Muon Trigger

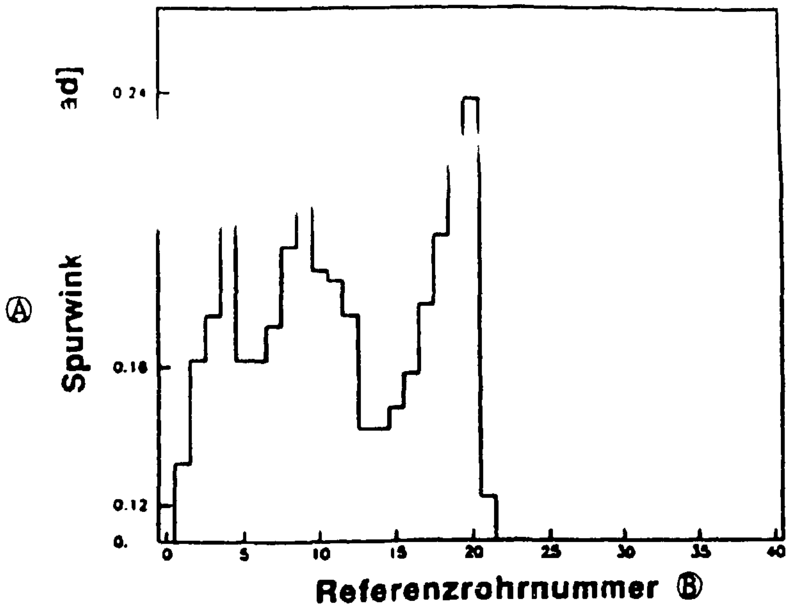

A. Track angle
B. Reference tube number

Fig. 3.15: The Angular Resolution of the Muon Trigger

The average fillings, as they were used in 1984 and 1985 are used. At each reference tube, this configuration leads to an effective angle cut with 90% acceptance of all muon tracks from the vertex. This limit angle is plotted against the reference tube number for one projection. The long reference tubes from Module 9 are included in the plot. Other modules, of course, exhibit a somewhat different resolution. The angular acceptance is analyzed in detail in [54].

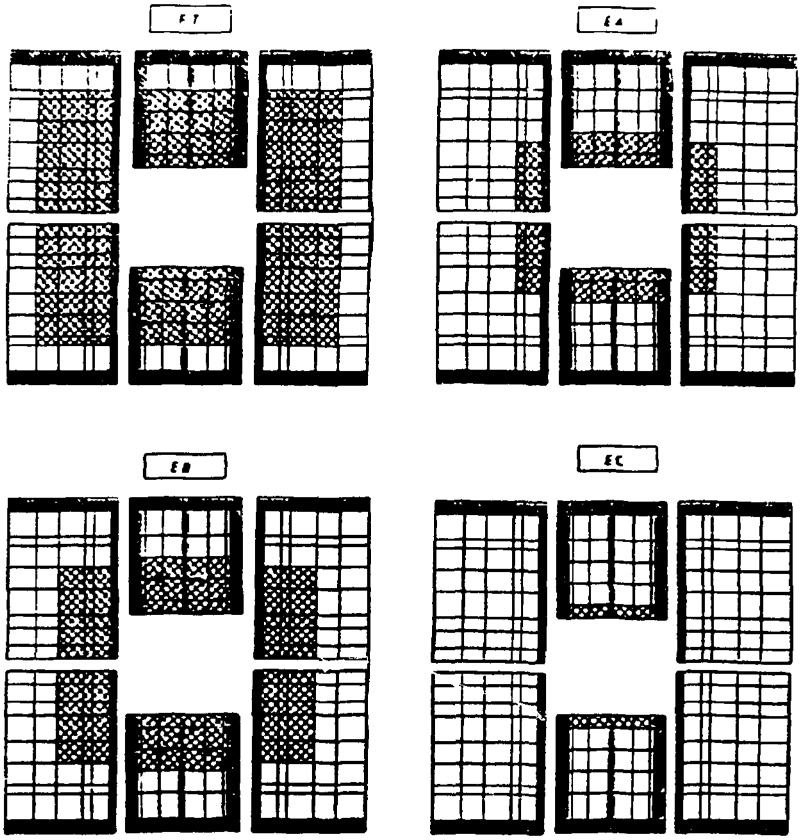

Fig. 3.16: The Muon Trigger Areas That Were Used

What are shown are the zones of the front chambers active in the trigger for various area definitions. Areas that are excluded are shown cross-hatched (from [135, 55]).

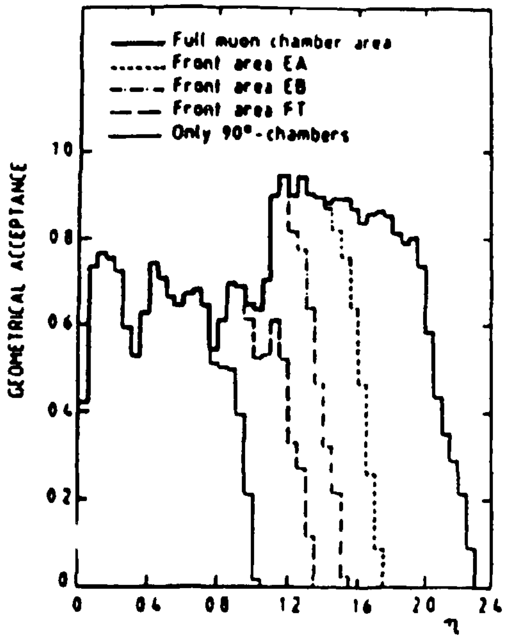

Fig. 3.1[illegible] The Acceptance as Function of the Rapidity of the Muon Trigger Regions

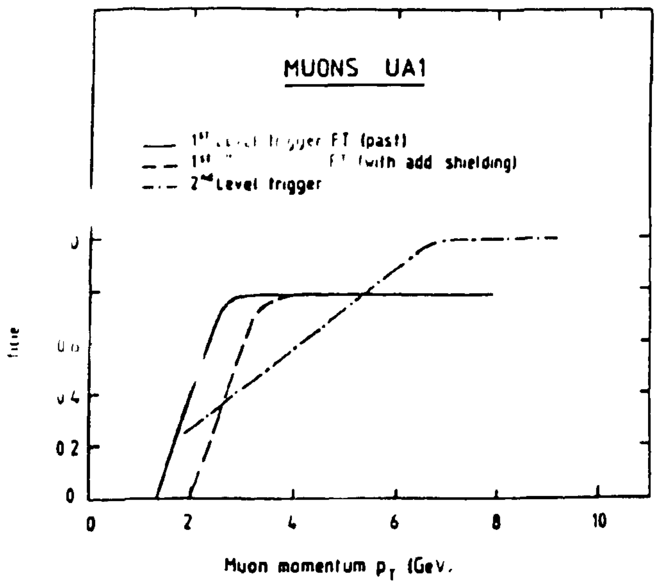

Fig. 3.18: The Efficiency of the Muon Trigger in the First and Second Levels

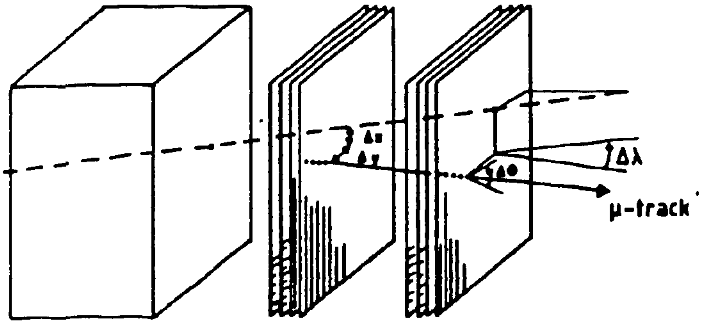

Fig. 3.19: On the Technique of the Combined Momentum Fit

A particle track entering this picture from the left would follow the dashed line if there were no deflection or scattering in the absorber. The position displacement Δx, Δy, and the angular deflection $\Delta\lambda$, $\Delta\Phi$ may be measured in the local coordinate system of the muon chambers. From these parameters one can reach conclusions about the momentum of the particle.

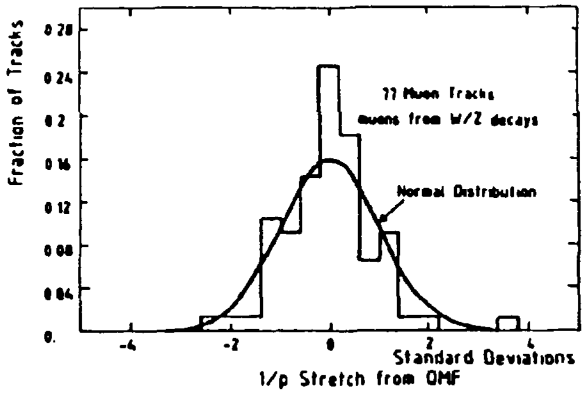

Fig. 3.20: Comparison of the Momentum Measurements in the CD and with OMF

The "stretch" function of the combined momentum fit is shown for 77 muon tracks from identified W and Z^0 decays. The quantity of data and the integral of the curve are both normalized to unity.

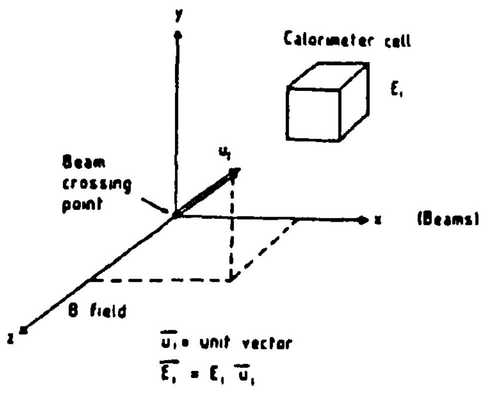

Fig. 3.21: On the Construction of Energy Vectors

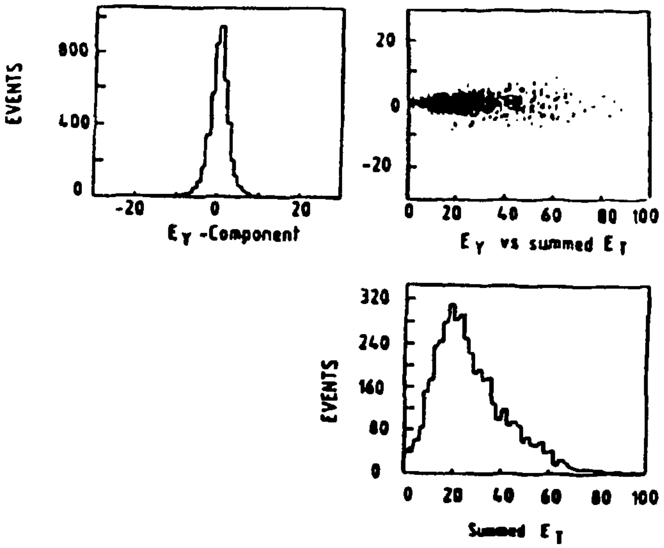

Fig. 3.22: The Precision of Neutrino Momentum Measurement

The Figure shows a scatter plot of the scalar transverse energy E_t versus one component of the vectorial energy sum, as well as the two projections.

Calorimeter	Gondolas	C's	Bouchons	I's
Plate thickness	1.2 mm	5.0 cm	4.0 mm	5.0 cm
Scintillator thickness	1.5 mm	1.0 cm	6.0 mm	1.0 cm
Thickness at normal incidence	$26.4\ X_0$ $1.1\ \lambda$	$5.0\ \lambda$	$26.7\ X_0$ $1.2\ \lambda$	$7.1\ \lambda$
Cell size $\Delta\phi$ x $\Delta\eta$	$180^\circ \cdot 0.1$	$15^\circ \cdot 0.3$	$11^\circ \cdot 1.5$	$15^\circ \cdot 0.4$
Number of cells	48	232	64	128
Long. segmentation	4	2	4	2

Absorber	Top	Floor	Side	Front
Thickness of added iron absorber	60 cm	40 cm	80 cm	100-120 cm
Maximum rapidity	0.9			2.4

Table 3.1: Properties of the Calorimeters and the Iron Absorbers

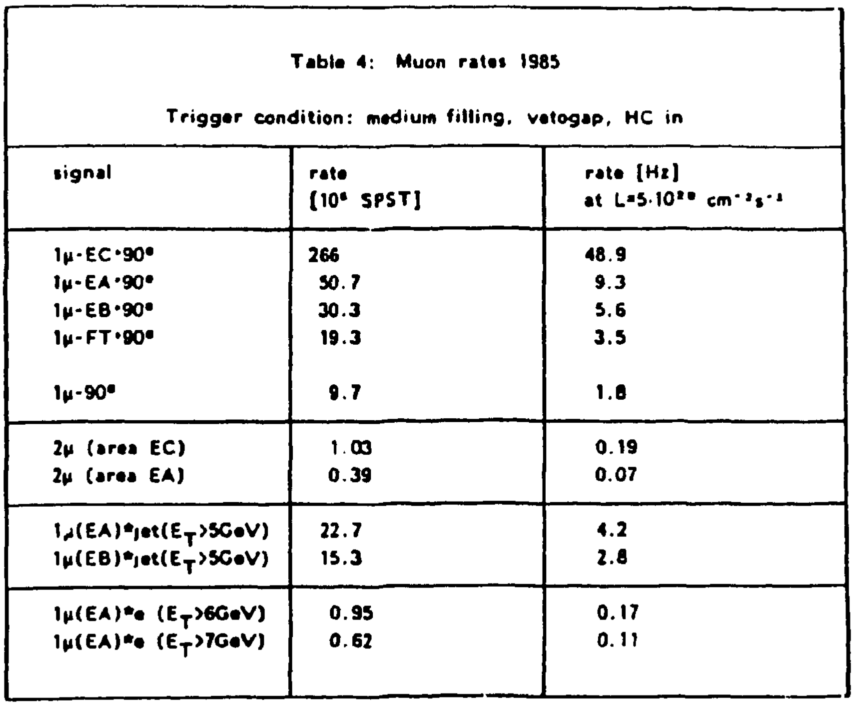

Table 4: Muon rates 1985

Trigger condition: medium filling, vetogap, HC in

signal	rate [10^6 SPST]	rate [Hz] at $L=5\cdot10^{29}$ $cm^{-2}s^{-1}$
1μ-EC·90°	266	48.9
1μ-EA·90°	50.7	9.3
1μ-EB·90°	30.3	5.6
1μ-FT·90°	19.3	3.5
1μ-90°	9.7	1.8
2μ (area EC)	1.03	0.19
2μ (area EA)	0.39	0.07
1μ(EA)*jet(E_T>5GeV)	22.7	4.2
1μ(EB)*jet(E_T>5GeV)	15.3	2.8
1μ(EA)*e (E_T>6GeV)	0.95	0.17
1μ(EA)*e (E_T>7GeV)	0.62	0.11

Table 3.2: The Muon Trigger Rates for 1985 (From [55])

Chapter 4

Selecting the Z^o Events

4.1 The Production of Muons

Proton-antiproton collisions may lead to prompt pairs of muons by the Drell-Yan process. In this process an incident quark-antiquark pair annihilates to form a virtual photon which, in turn, decays into a $\mu^+\mu^-$ pair. It is known from the electroweak theory that the photon interferes with the Z^0. A resonance sits on the strongly falling mass spectrum of the virtual photon at the location of the Z^0 mass. The Drell-Yan process leads to central muon pairs, i.e. muon pairs that are produced at small rapidities. In the case of the Z^0 resonance we expect leptons with transverse momenta between 20 and 80 GeV/c.

Events with a quasi-prompt muon can arise when heavy quarks are generated in the final state. In the course of the fragmentation of these quarks, which follows immediately, weak semi-leptonic decays may also occur. Because of the complicated dynamics of the strong interaction many processes contribute to such decays. Bound states such as Υ or J/Ψ, which decay into muon pairs,
may also be produced.

The processes described so far are, however, relatively rare in comparison to another important source of muons, the decay of light quarks (u d, s). Because of the high multiplicity in proton-antiproton collisions, these decays produce by far the highest muon rate. It is true, though, that the muons from these reactions mostly have relatively small transverse momenta.

Fig. 4.1 shows the transverse momentum spectrum of the inclusive muon events with $p_t^\mu > 6$ GeV/c. One first notes the steep fall-off towards high momenta. The calculated back-ground is also shown in the plot; it consists mainly of the decays of light quarks. At low transverse momenta pion and kaon decays are dominant, at intermediate momenta the heavy quarks play a dominant role. Events with muon pairs are about 100 times rarer than events with only a single muon. Finally, at the highest transverse momenta the signal from prompt muons has only a minor background; we are in the domain of the muons from W and Z production.

4.2 The Principle of Muon Detection

In order to identify a muon it is not enough to rely only on the track in the muon detector. It is true that the muon is identified there, but to measure its momentum we also need the central detector. The individual sub-detectors are tied together by means of the UA1 reconstruction programs, and the physical parameters of the particles are determined. Only by using all the detector information is a muon identified [60].

All the calorimeters form a particle filter through which muons and neutrinos may pass, but in which all other particles are absorbed. The filter effect is characterized by a material property, the absorption length. The quantity of material that a muon must pass through amounts to 8.2 absorption lengths in the forward region, and 6.1 absorption lengths in the central region. The additional iron shielding amounts to 3.6 absorption lengths at the sides, 2.4 absorption lengths at the top, and 7.0 absorption lengths in the front region. Thus the particles must pass through at least 8.5 absorption lengths to reach the muon chambers. For muons this is easy, since they do not interact; hadrons, on the other hand, are suppressed by a factor of $e^{-8.5} \approx 2 \times 10^{-4}$. In addition, the muons lose energy as they pass through the absorber. This energy loss leads to a natural minimum momentum of 2 to 3 GeV/c, which the muons must have to reach the chambers at all.

First of all, the momenta of all particles are determined in the central detector. Then all tracks are extrapolated through the calorimeters and the absorbers. In doing this the deflection due to the magnetic field, the multiple scattering, and the energy loss in passing through matter are all taken into account. If the energy of the particle is exhausted, the extrapolation ends. In case the particle has sufficient energy to reach the muon chambers, a test is made at the point where the extrapolation impacts the chamber to see whether a track was reconstructed in the chamber near the point of extrapolation. If a muon candidate is indeed encountered there, the displacement between the extrapolation and the reconstructed track is established in each chamber projection. The difference in angle is determined in the magnetic deflection plane, the x-y plane, and out from this plane ($\Delta\Phi$ and $\Delta\lambda$). As a measure of the goodness of the agreement one uses the ratio of the deflection of the point found by the extrapolation to the theoretically expected precision. A χ^2 test is made for the position and the angle, and then an average is formed of the two values. Of course the displacement and the angular deflection are functions of the transverse momenta of the muons, since these are deflected in the absorber my multiple scattering, and more strongly so at lower momenta. Not all tracks can be extrapolated as far as the muon chambers with the same precision. Based on the design of the central detector and the orientation of the magnetic field, tracks which lie along the direction of the magnetic field are extrapolated with larger errors than are tracks perpendicular to the field. We therefore calibrate the procedure that tests the agreement between the extrapolation and the found track by using cosmic-ray muons. Furthermore, errors in the absolute position determination of the central detector and the muon chambers, lead to position-dependent systematic errors, for which corrections are made. The total error σ for the extrapolation thus contains a constant base error:

$$\sigma^2 = \sigma_{CD}^2 + \sigma_\mu^2 + \sigma_0^2 \tag{4.1}$$

The calorimeter information is also used for identification, but only in those cases in which the muon is isolated, in other words, there is no other particle in the vicinity. As will be shown below, that is, however, the case for the Z^0 events. Fig. 4.2 shows muon identification based on a track in a Z^0 event. The mean expected energy loss of the muon amounts to ≈ 0.6 GeV in the gondola and 2.0 GeV in the C module for perpendicular incidence. This energy deposition must be taken into account in the energy analysis of the event. For this reason, when a muon has been identified as such, the mean expected energy deposition, which was determined by a calibration of the calorimeters in a test beam, is subtracted from the calorimeter energy.

To complete the process of a good muon identification, the last step is an inspection of the event by a physicist at a graphics station. At this stage reconstruction errors may be noticed and perhaps removed by correcting obviously wrong measured values and repeating all the fitting procedures. Many of the off-line procedures for event reconstruction were derived from the visual inspections.

4.3 Calibration With Cosmic Radiation

During each measuring period our experiment collected about 1 million events stemming from cosmic radiation. This radiation consists to a great part of muons with energies up to the TeV range [61, 62], which are ideally suited for calibrating the apparatus. We triggered for this radiation outside the time of the $p\bar{p}$ beam period in order to obtain an independent event sample for calibrating our equipment. Around the detector there are scintillation counters which are operated in coincidence with the calorimeter cells located in the diagonally opposite direction, in order to trigger on cosmic-ray particles. Fig. 4.3 shows the arrangement. In addition the bouchons are used to obtain horizontal muons in the forward direction.

Individually, the following needs were met by using such events:

- Checking the energy calibration of the calorimeters,
- determining the systematic error in the CD measurement of the direction and momentum of a charged particle,
- determining the relative positions of the central detector and the muon chambers, and
- determining the magnetic field in the iron yoke, especially at locations that could not be reached by other methods.

All points are relevant for our analysis, because all detector components that we need for muon identification are made to be interrelated.

Cosmic-ray muons with a momentum greater than 10 GeV/c are used to measure systematic displacements of the central detector and the muon chambers from their nominal positions. These displacements were found to lie in the coordinates perpendicular to the magnetic field (x, y, Φ) and to amount to about 1 cm and 5 milli-rad. They were interpreted as true displacements of the two detectors relative to each other. The systematic differences in the parallel coordinates, on the other hand, are larger and are correlated with each other. These may be explained as systematic errors in the measurement of the z coordinate in the central detector.

Furthermore, a momentum dependence of the coordinate difference was observed; it stemmed from an inadequate knowledge of the magnetic field, which systematically influences the extrapolation of tracks through the calorimeters. A field correction was obtained from the data analysis of the cosmic-ray events.

Using the correction tables thus obtained it was possible to center the spectra of location and angle displacements between the CD and the muon chambers. From the widths of these spectra we learn the precision with which we can measure the agreement between the central detector track and the muon chamber track. This precision is the base error, given above, in the definition of σ^2.

In the case of the high-energy muons from the cosmic radiation we obtain a reconstruction coefficient of 97% if the cut-off is made at four standard deviations in all the quality criteria (χ_x^2, χ_y^2, χ_λ^2, χ_ϕ^2). In selected events with one muon from a jet only 75% of the muon candidates survive the requirements. Thus the quality characteristics turn out poorer than in the correct measurement of a prompt, isolated muon. We see that the cut-offs in the track-agreement suppress background to the muon signal. A falsified momentum measurement is also obtained when particle tracks overlap or when mesons decay unseen, since in such a case the particle track is wrongly extrapolated through the calorimeters and the absorber.

The inelastic cross section for proton-antiproton collisions is about 50 mbarn [63]. In contrast with this value, the theoretically expected cross section, multiplied by the branching ratio in the leptonic decay channel of the Z^0, turns out to be about 50 pbarn, smaller by 9 orders of magnitude. The task of filtering out individual events of interest out of a billion uninteresting events is solved in two stages. The

50 pbarn, smaller by 9 orders of magnitude. The task of filtering out individual events of interest out of a billion uninteresting events is solved in two stages. The trigger of the experiment achieves a reduction of 10^3 to 10^4, depending on the luminosity. After the remaining events have been stored on magnetic tape, off-line selection is begun. The reduction capability of these two stages will now be described (see also [64, 65]).

4.4 On-Line Selection

The quality of the muon trigger has been considerably improved in the course of the years. While in 1983 the work was still done at low luminosity, the luminosity increased considerably in the years 1984 and 1985. In order to be able to keep in step with the increased trigger rate, two improvements were undertaken. For one, the passive iron shielding was made thicker. This additional iron was also instrumented, so as to make it possible to follow a muon candidate through the absorber.

The second measure consisted of taking two measures to modify the fast muon trigger. At the higher luminosities the intermediate fillings, rather than the wide ones, were used. This caused a sharper cut-off with respect to the direction of the muon to the point of interaction. Because of the momentum dependence of the Coulomb scattering in the absorber, this measure, in effect, causes a higher p_t cut-off for the muons. A still sharper cut-off by using the narrow fillings would have meant a reduction of the signal from good muons, without a further strong reduction of the background. Further, additional trigger cards were developed with which the active trigger area in the front regions could be dynamically reduced when the muon trigger rate exceeded its allowed maximum rate of 60% of the total trigger rate, thus introducing too much dead-time.

4.4.1 The Geometric Acceptance

In 1984 the main areas active in the one-muon trigger were FTOLD, EA, and EB. However, mostly these areas were additionally reduced in effective size by a veto zone around the beam tube. In the year 1985 the most used areas of the one-muon trigger were areas FT and EA. In the two-muon trigger in 1985 the largest area EC was uniformly used, whereas in 1984, due to insufficient electronics we still worked with the old areas EA and a reduced area FTOLD, based on the one-muon trigger. It is true that, due to electronics problems, more complicated triggers were still used in both years, on which, however, only a small amount of integrated luminosity was incident. A table of the most important conditions and their contributions to the total luminosity is shown in Table 4.1. In the muon trigger actually used, a total of 255 nbarn^{-1} of integrated luminosity were recorded in 1984; for 1985 this figure was 195 nbarn^{-1}. [Translator's note: The first digit in the number 195 is almost illegible in the manuscript and may be in error.]

For the reasons described, the geometric acceptance is different in each of the three periods. This quantity is determined using Monte Carlo events. In this method Z^0 events are generated and then a test is performed to check how often the muons from the decay of the Z^0 are incident on the sensitive area of the trigger. In this connection it is necessary to take into account both the two-muon acceptance and the one-muon acceptance, since we also include Z^0 events in which only a single muon is found by muon detector, while the other muon can be identified by the rest of the apparatus.

Thus there were a total of four possible trigger sources during 1984. If each of these is weighted by its applicable luminosity, the geometric acceptances given below result:

a) Both muons fall within the three-dimensional acceptance of the muon detector. However, one muon lies in the veto region of the front zone. Hence the one-muon trigger is activated instead of the two-muon trigger.

$$\epsilon_{geo,84}^{1(2)} = 9.4 \pm 0.9\,\% \tag{4.2}$$

b) One muon passes through one of the open gaps in the muon detector. Again, only the one-muon trigger is started.

$$\epsilon_{geo,84}^{1(1)} = 46.2 \pm 0.3\,\% \tag{4.3}$$

c) Both muons are fall within the trigger acceptance EA and fire the two-muon trigger.

$$\epsilon_{geo,84}^{2(2),EA} = 23.9 \pm 0.9\,\% \tag{4.4}$$

d) Both muons fall in the trigger acceptance FTOLD and activate the two-muon trigger.

$$\epsilon_{geo,84}^{2(2),FTOLD} = 12.6 \pm 0.5\,\% \tag{4.5}$$

In the year 1985 the conditions were simpler, since the largest possible area, EC was used in the two-muon trigger. This eliminated one channel in which a muon falls within the veto zone, while the other muon hits the sensitive one-muon region. Thus in this case not the one-muon trigger, but the two-muon trigger is activated. This yields the following acceptances:

a) One muon is found in the one-muon trigger; the other passes through a gap in the muon detector

$$\epsilon^{1(2)}_{geo,as} = 49.3 \pm 0.3\,\% \tag{4.6}$$

b) Both muons fall within the acceptance of are EC.

$$\epsilon^{2(2)}_{geo,as} = 46.7 \pm 0.5\,\% \tag{4.7}$$

4.4.2 The Efficiency of the Detector and the Trigger

The efficiency of the drift tube detector can be directly determined from a comparison of 3-hit and 4-hit tracks in one projection [56]. I we let $p_{3,4}$ be the number of 3-hit and 4-hit tracks, then one finds for the efficiency in one layer ϵ_{tE}, the efficiency in one projection ϵ_{tP}, and in the chamber ϵ_{tK}:

$$\begin{aligned} \epsilon_{tE} &= \frac{1}{1+\frac{p_3}{4p_4}} \\ &= 91.4 \pm 0.8\,\% \end{aligned} \tag{4.8}$$

$$\begin{aligned} \epsilon_{tP} &= \epsilon_{tE}^4 + 4 \cdot (1-\epsilon_{tE}) \cdot \epsilon_{tE}^3 \\ &= 96.1 \pm 0.7\,\% \end{aligned} \tag{4.9}$$

$$\begin{aligned} \epsilon_{tK} &= \epsilon_{tP}^2 \\ &= 92.4 \pm 1.3\,\% \end{aligned} \tag{4.10}$$

The efficiency of the fast muon trigger was investigated with a simulator which, from the given drift tube data and the calorimeter information imitates the algorithm wired into the hardware. Initially Monte Carlo events, that contain a complete detector simulation, were used. Additionally other data were utilized that stemmed from other trigger sources but nevertheless contain a reconstructed muon. The latter types of events were searched for possible muon triggers that the electronics had missed, either because an error occurred in the hardware, or because the track points inaccurately to the point of interaction. There was agreement between real events and Monte Carlo events, with both yielding a fast trigger efficiency of 90% based on the fillings; the real data with calorimeter trigger contribute an inefficiency of about 8% to this number, due to electronics errors; of this 5% stem from the muon trigger and 3% from the calorimeter interface. Accordingly the total efficiency of the fast muon trigger is:

$$\epsilon_{FT} = 82 \pm 3\% \qquad (4.11)$$

The algorithms of the second trigger level[3] were also investigated with respect to their efficiencies. Data that were collected without this trigger were required in exactly the same manner. Such a sample is formed of events with one muon and a jet that were written onto the magnetic tape without application of the second trigger. It was found that the finding of an external point using the MUTUBE algorithm is very efficient.

$$\epsilon_{ext.P} = 99.6\% \qquad (4.12)$$

The efficiency of the VENI algorithm, which was used directly afterwards, which measures the momentum of the muon candidates in the central detector was

---

[3] These algorithms are briefly described in the chapter on the equipment.

determined with the aid of the subset of events with one isolated muon with a momentum greater than 10 GeV/c, such as are also available in a Z^0 event.

$$\epsilon_{VENI} = 89.9 \pm 1.1\,\% \tag{4.13}$$

In the year 1985 the algorithm MUTIME was used instead of MUTUBE and VENI. Studies with the 1984 data indicate complete efficiency.

$$\epsilon_{MUTIME} = 100\,\% \tag{4.14}$$

4.5 Off-Line Selection

The method for selecting W and Z events changed in the course of data acquisition. Initially practically all events were examined and classified at the scan table. Unambiguous scanning prescriptions were only gradually worked out in the course of time. Later the prescriptions thus developed were converted to algorithms that allowed the replacement of visual scans by computer programs. The underlying philosophy of such selection programs even underwent some changes during production operation. The required steps needed for separating the signals of good events as efficiently as possible from undesired background were established gradually.

One large advantage of automated selection lies in its reproducibility and its controllability, since it substitutes objective criteria for the subjective decision of the scanner. Only in this way is a determination of the efficiency and the included background possible.

The off-line selection is carried out in four stages: 1) loose inclusive muon selection, 2) tight selection, 3) loose W/Z selection, and finally 4) Z^0 selection.

The selection criteria are sharpened from state to stage, and thus the identification is improved. The first three stages are described in detail in the Technical Notes of the experiment [67. 68, 69].

In the loose selection a muon is defined by the fact that a track is found in the muon chamber, and a track that fits with it is found in the central detector, for which $P_t > 3$ GeV/c. The agreement between the two tracks does not have to be very good, since at the point in time when the loose selection is made, the exact geometry of the apparatus, which will only be obtained by calibration with cosmic rays, is not yet precisely known.

The TKDLOO processor [71] tries to recognize cosmic-ray muons in the events. To do this the track of a muon candidate is separated from the vertex in the central detector, by removing that point from the fit, and the track is again fitted without the vertex point. If the new fit shows that the track now passes by the vertex, a search is done for a second track which extends the first-found track after this first track has been released from the vertex. If this is the case, the event is discarded.

At the same time, a check is also carried out to determine whether the track in question passed through the central detector exactly at the moment in time when the interaction occurred. A small time difference manifests itself as a displacement of the track sections at the boundaries of the drift volumes, at which the drift direction reverses. This procedure recognizes a large fraction of the cosmic-ray muons, without affecting the signal from the prompt neutrons. Using Monte Carlo events it was established that of 790 Z^0 events not a single one was rejected.

After the muon definition has been established, selections into event classes are undertaken: The two-muon events, the muon-electron events, the J/ψ candidates and the inclusive Muon events with $P_t^\mu > 6$ GeV/c.

The tight selection that starts with the inclusive muon sample makes use of the exact geometry of the apparatus [70]. Now a better agreement between the muon chamber track and the central detector track is required. Furthermore, the final calibration of the central detector is used in the reconstruction. Fiducial cut-offs are applied using the CLIQUE processor [72], and all events that show noticeable activity in the regions of the gaps and of the edges of the detector are rejected. An additional processor eliminates events in which a knee is found in the muon track in the central detector, which would indicate a decaying meson [73] (see Fig. 4.4). This serves efficiently to suppress secondary muons from such decays.

The loose W/Z selection then selects all those events that include a muon with transverse momentum $p_t^\mu > 15$ GeV/c. This makes the process, on the one hand, efficient in finding vector bosons, while, on the other hand, the background is still only very weakly represented. It is from this sample that at the end the Z^0 candidates are sought. Table 4.2 is a summary of the sizes of the samples after each of the individual selection stages.

The Z^0 candidates are now filtered out of the inclusive muon events with $p_t^\mu > 15$ GeV/c by using the following cut-offs:

a) A muon with $p_t^\mu > 15$ GeV/c, which has activated the muon trigger, is required.

b) In the central detector the track must satisfy the following quality criteria:

1) The track length projected onto the x-y plane must be longer than 40 cm.

2) The number of points on the track must be greater than 30.

3) χ_s^2 must be smaller than 3.

4) χ_z^2 (<u>the number of degrees of freedom</u>) must be less than 9.

5) $\chi_{CD\text{-}\mu}^2$, which is a measure of the agreement between the central detector track and the muon chamber track, must be less than 15.

c) It is required that in addition an further track be found in the central detector, whose transverse momentum is greater than 10 GeV/c. This track must exhibit minimum ionization in the calorimeters, but does not necessarily have to point to a track in the muon chambers if it goes towards the edge of the acceptance of the chambers or even a gap in the muon detector. In such a case the Iarocci chambers in the additional iron absorber help to identify the track as a muon.

d) This second track need only satisfy less stringent quality criteria in the central detector: $\chi_s^2 < 6$, χ_z^2/(<u>number of degrees of freedom</u>) < 9, projected track length $\geq$ 30 cm, number of points $\geq$ 25.

e) The invariant mass of the two muons must amount to more than 30 GeV/c^2.

f) The events with a mass between 30 GeV/c^2 and 50 GeV/c^2 are included with the class of muon pairs with small and intermediate mass [74], and thus fall outside the Z^0 sample.

g) All events must pass an examination by experienced physicists at the graphics screen. They are checked once more in order to recognize possible background events.

4.5.1 The Efficiency of the Selection Programs

The efficiency of the selection programs was determined using real data, with the help of a Monte Carlo method. Full understanding of hard proton-antiproton collisions is still a subject for research; hence a complete simulation of such events is naturally model-dependent and incomplete. In particular, the properties of the spectator quarks and gluons that participate in the collision are not precisely enough known. But just these have a strong influence on the part of the event that is not directly connected with the production of the Z^0. We also call this part the underlying event or the rest of the event. We therefore made the decision to have recourse to real data in measuring the efficiency of the selection programs. As initial sample we select the group of events in which the reaction $W \rightarrow e + \bar{\nu}_e$ has been identified. Then the W, in other words, the electron and the anti-neutrino are artificially removed from the event. Then one inserts a Z^0 in place of the W, and lets the Z^0 decay into two muons. These muons are then simulated in the detector. With such events the efficiency of the programs can then be calculated.

If the two-muon trigger has fired, only one of the muons has to pass the tight quality criteria in the central detector. The efficiency for this amounts to:

$$\epsilon_{CD}^{1(2)} = 79.5 \pm 11.9\,\% \tag{4.15}$$

The transverse momentum criterion which is then applied lets about 89% pass.

$$\epsilon_{\mu}^{1(2)} = 89.1 \pm 3\,\% \tag{4.16}$$

If the event stems from the channel with the one-muon trigger, then that muon itself must pass the quality criteria. For this case we undertook a more searching investigation. The simulated track of this muon was modified in such a manner that the length of the track and the number of points in the central detector would be compatible with tracks from a sample of high-energy isolated pions. Afterwards the efficiency was determined. It turned out to be:

$$\epsilon_{CD}^{1(1)} = 63.8 \pm 2\,\% \tag{4.17}$$

The transverse momentum criterion which was then imposed was passed by about 95%.

$$\epsilon_{\mu}^{1(1)} = 94.7 \pm 1\,\% \tag{4.18}$$

These values were used for 1984 and 1985.

4.6 The Total Efficiency of Selection

The total selection efficiency can now be calculated from the individual factors.[4] The result is:

1985:

$$\begin{aligned}\epsilon^{1\mu,2\,\mu in Spalt} &= \epsilon_{tK}^{1(1)} \cdot \epsilon_{FT}^{1(1)} \cdot \epsilon_{CD}^{1(1)} \cdot \epsilon_{\mu I}^{1(1)} \cdot \epsilon_{geo,85}^{1(2)} \cdot \epsilon_{MUTIME}^{1(1)} \\ &= 22.5 \pm 1.1\,\% \end{aligned} \tag{4.19}$$

$$\begin{aligned}\epsilon^{2\mu,EC} &= \epsilon_{tK}^{2(2)} \quad \epsilon_{FT}^{2(2)} \cdot \epsilon_{CD}^{1(2)} \cdot \epsilon_{\mu I}^{1(2)} \cdot \epsilon_{geo,85}^{2(2),EC} \\ &= 19.0 \pm 3.1\,\% \end{aligned} \tag{4.20}$$

$$\epsilon_{85}^{total} = 41.5 \pm 1.7\,\% \tag{4.21}$$

1984:

$$\begin{aligned}\epsilon^{1\mu,2\cdot\mu in Veto} &= \epsilon_{tK}^{2(2)} \cdot \epsilon_{FT}^{1(2)} \cdot \epsilon_{CD}^{1(2)} \cdot \epsilon_{\mu I}^{1(2)} \cdot \epsilon_{geo,84}^{1(2)} \\ &= 4.7 \pm 0.9\,\% \end{aligned} \tag{4.22}$$

$$\begin{aligned}\epsilon^{1\mu,2\,\mu in Spalt} &= \epsilon_{tK}^{1(1)} \cdot \epsilon_{FT}^{1(1)} \cdot \epsilon_{CD}^{1(1)} \cdot \epsilon_{\mu I}^{1(1)} \cdot \epsilon_{geo,84}^{1(1)} \cdot \epsilon_{VENI}^{1(1)} \cdot \epsilon_{ext,P}^{1(1)} \\ &= 18.9 \pm 0.9\,\% \end{aligned} \tag{4.23}$$

$$\begin{aligned}\epsilon^{2\mu,EA} &= \epsilon_{tK}^{2(2)} \cdot \epsilon_{FT}^{2(2)} \cdot \epsilon_{CD}^{1(2)} \cdot \epsilon_{\mu I}^{1(2)} \cdot \epsilon_{geo,84}^{2(2),EA} \\ &= 9.7 \pm 1.6\,\% \end{aligned} \tag{4.24}$$

---

[4] The index 1 (2) signifies that the corresponding efficiency must be calculated for one of the two muons: $\epsilon^{1(2)} = (2 - \epsilon^{1(1)}) \cdot \epsilon^{1(1)}$, 2(2) signifies the efficiency for both: $\epsilon^{2(2)} = \epsilon^{1(1)} \cdot \epsilon^{1(1)}$

$$
\begin{aligned}
\epsilon^{2\mu,FTOLD} &= \epsilon_{IK}^{2(2)}\ \epsilon_{FT}^{2(2)}\ \epsilon_{CD}^{1(2)} \cdot \epsilon_{pt}^{1(2)} \cdot \epsilon_{geo,84}^{2(2),FTOLD} \\
&= 5.1 \pm 0.9\,\%
\end{aligned}
\tag{4.25}
$$

$$
\epsilon_{84}^{total} = 38.4 \pm 2.2\,\% \tag{4.26}
$$

84, 85:

$$
\epsilon_{84,85}^{total} = 40.1 \pm 2.8\,\% \tag{4.27}
$$

(luminosity weighted averaged)

1983:

$$
\epsilon_{83}^{total} = 37.0 \pm 5\,\% \tag{4.28}
$$

We also checked to see whether the acceptance of our equipment, the trigger, and the selection depend on the transverse momentum of the Z^0. For this purpose the ISAJET program was used to generate Z^0 events followed by a muonic decay, and these Z^0 events were then subjected to a complete detector simulation. The result was that the acceptance is lower at low and high values of the p_t than at intermediate p_t. The behavior at very small transverse momenta is understandable from the detector geometry, since in that case the decay muons are rather back-to-back in the transverse plane; if one muon misses the chambers, the second muon will probably do so also. At intermediate values of p_t the probability that at least one muon hits the chambers increases. It is true, however, that an even stronger influence on the acceptance is exerted by our method of determining the transverse momentum of the vector boson solely from the calorimetry; this procedure will be described in more detail in the chapter on the production properties of the Z^0. We find: The transverse momenta that are in truth small are displaced towards higher values in the measurement, due to the limited energy resolution in the calorimeters.

In contrast, at the really high transverse momenta of the vector bosons, the recoil energy, which we measure in the calorimeter, becomes more and more jet-like. Thus we measure the energy spectrum of the recoil jet, which in reality has a steeper shape than our measurement. In the acceptance curve this is manifested by a slight fall-off at high transverse momenta. Furthermore, the acceptance decreases at high P_t since there it less more probable that both muons pass the transverse momentum criterion at the same time.

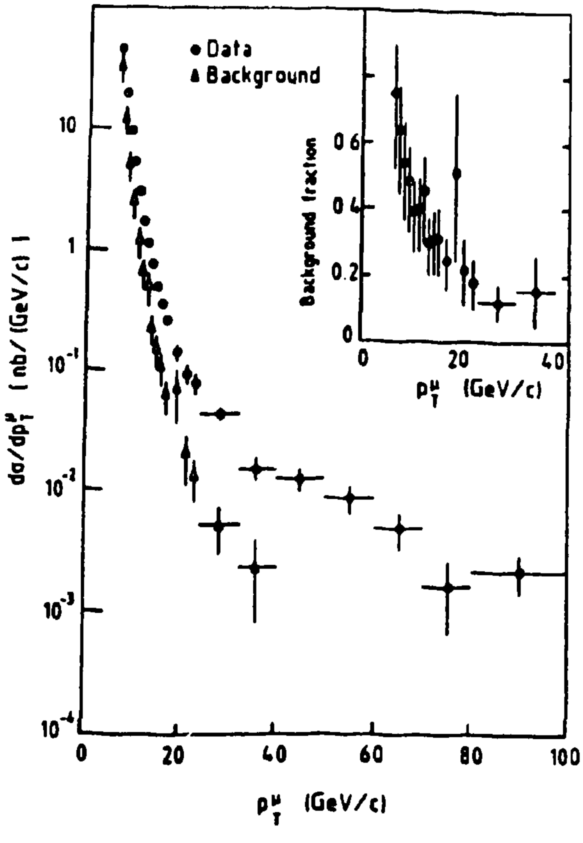

Fig. 4.1: The Transverse Momentum Spectrum for the Inclusive Muon Events

The plot shows the frequency of all reconstructed muons with transverse momentum greater than 6 GeV/c. The background was calculated using the hadron momentum spectrum measured with the UA1 [77] and the complete detector simulation.

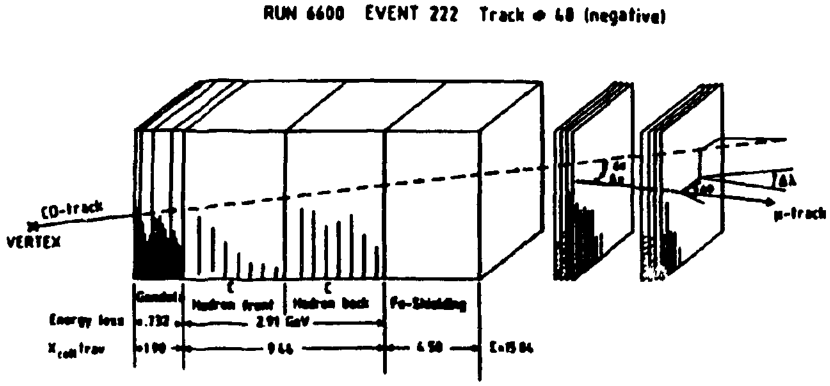

Fig. 4.2: The Identification of Muons

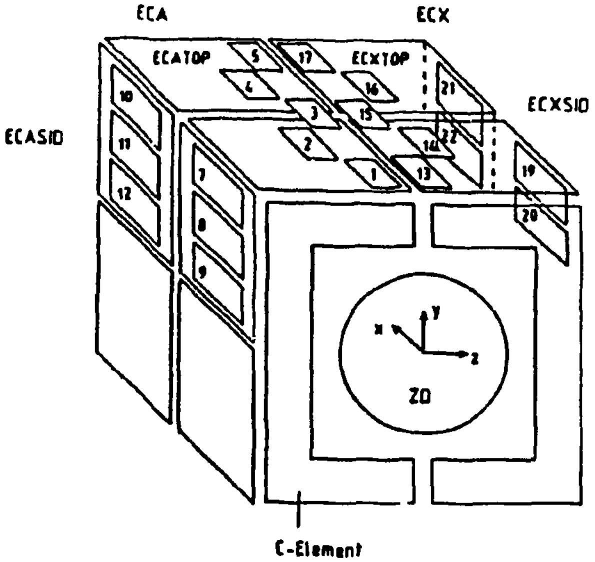

Fig. 4.3: The Placement of the Cosmic-Ray Counters

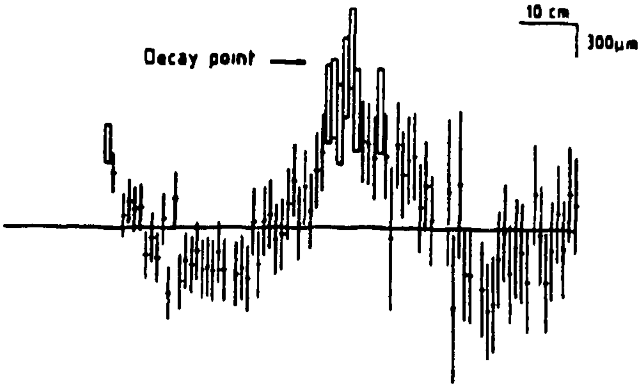

Fig. 4.4: Example of a Muon Decay in the Central Detector

The reconstructed track points in the central detector are shown, together with their errors; The vertex is at the left, the vertical and horizontal scales are different. The straight line is the result of the track reconstruction. A meson with small transverse momentum decays under such an angle that the program does not recognize it, and it combines the two low-energy tracks before and after the decay into a single high-energy track.

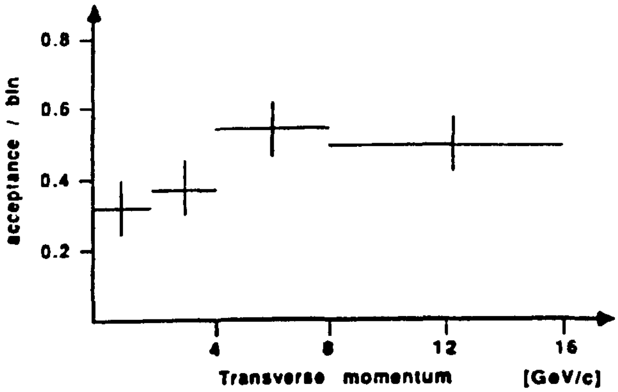

Fig. 4.5: The Acceptance as Function of $p_t(Z^0)$

The errors shown for the acceptance are of purely statistical nature Above 16 GeV/c we apply no correction.

Ⓐ **Relative Anteile der Triggerflächen an der integrierten Luminosität in %**

1984	1μ	2μ	1985	1μ	2μ	$\mu \cdot jet$
FTOLD	12.9	34.8	EC	0.0	96.4	0.0
EA	25.2	62.8	EA	51.7	0.0	69.0
EB	13.0	0.0	EB	0.0	0.0	27.3
FT	4.8	0.0	FT	44.7	0.0	0.0
Ⓑ EA ohne Modul 31-33	10.4	0.0				
Ⓒ FTOLD ohne Modul 31-34	17.5	0.0				
90° – *Region*	8.0	0.7	Ⓓ			
Ⓓ sonstige	8.2	1.7	sonstige	3.6	3.6	3.6

A:	Relative contributions by the trigger areas to the integrated luminosities in %
B:	EA without Module 31-33
C:	FTOLD without Module 31-34
D:	other other

Table 4.1: The Significant Muon Trigger Regions in 1984 and 1985. The areas were presented in the detector description.

		1983	1984	1985
Ⓐ	integ. Luminosität	$108\,\mathrm{nb}^{-1}$	$255\,\mathrm{nb}^{-1}$	$296\,\mathrm{nb}^{-1}$
Ⓑ	Myonentrigger	$\approx 4 \times 10^5$	$\approx 2 \times 10^6$	$\approx 4 \times 10^6$
Ⓒ	Lose Selektion	3200	20000	21000
Ⓓ	Enge Selektion	2300	8000	12000
	$p_t^\mu > 15\,\mathrm{GeV}/c$	≈ 100	≈ 450	411

A: Integ. Luminosity

B: Muon trigger

C: Loose selection

D: Tight selection

Table 4.2: Number of Events According to the Individual Selection Steps

Chapter 5

The Z^o Data Sample

5.1 The Result of the Selection

For 1985 the described selection from 411 events of the sample with $p_t^\mu >$ 15 GeV/c yielded 21 Z^O candidates before the visual inspection. 2 events were recognized at the graphics screen as cosmic rays that mimicked a Z^O. In 10 events the second track could be identified as belonging to a jet. In one event both muons are accompanied by hadronic energy. This case led to an erroneous reconstruction in the central detector; in truth, this event has two equally charged muons with an invariant mass of 15 GeV/c^2. Thus 8 Z^O events remain. The final sample includes 2 additional events: One event (19208,17)[5] comes from a sample that was collected with reversed magnetic field. Another event (15971,770) barely fails the P_t^μ cut. We consider it as a good Z^O event, but do not count it in calculating the cross section. Thus we have a total of 10 events for 1985.

The selection for 1984 cannot be presented so clearly, since the data sample was subdivided into several smaller subsets. In the years 1984 and 1985 considerable improvements were still being introduced in the UA1 standard programs. The techniques that were used in doing so had to be learned in the course of making the selections, a process during which individual steps in the selection process had to be repeated several times in some cases, so as to eliminate mistakes that were

---

[5] The numbers indicate run and event numbers.

recognized. The samples were processed in a number of institutions, with the cuts presented above, in part, applied in different sequential orders. The only thing that can be compared is the result of the selections. 6 Z^0 events were found.

A similar selection process for 1983 yielded 5 events. The calculation of the acceptance and the cross section was done separately. One additional event in this sample, also, failed to pass all the quality cuts in the central detector, but is nevertheless regarded as a good Z^0, although it was not included in the calculation of the cross section. Here we shall merely make use of the results of the calculations done at that time [75, 76] without presenting the details yet one more time.

For the entire period of measurements the results thus are a total of 21 Z^0 events. The rapidity spectrum of the muons is shown in Fig. 5.1; the central production of the Z^0 is clearly observable. Fig. 5.2 shows the transverse momentum spectrum of the muons. The mean transverse momentum comes out to be 36 GeV/c. The shape of the spectrum corresponds to our expectation. From the spectrum of the total energy, shown in Fig. 5.3, it will be recognized that our detector system collects about 2/3 of the center-of-mass energy released in the production of the Z^0; about 300 Gev stems from the non-participating quarks and the gluons, $\approx$ 90 GeV are locked up in the mass of the Z^0, which, in the case of muonic decay in the calorimeter escapes without being observed. Table 5.1 is a summary of the most important event parameters. It contains the muon momenta from the measurement in the central detector, as well as the two-muon mass reconstructed from it. The transverse momentum of the Z^0 shown in the Table stems from the measurement of the missing transverse energy in the calorimeter. Table 5.1 also contains the missing transverse energy for the event, corrected for the recognized muons; in the table this missing energy is simply labelled "neutrino". Normally this energy should be in accordance with the transverse momentum of the Z^0, within the limits of error. If there is a significant difference between the two parameters it indicates that one or both of the transverse momenta of the muons were determined in error, either because the measurement in the central detector was in error, or because one muon did not hit the muon detector, and thus could not be recognized by the program as a muon. Using the scalar sum of the transverse energies we can draw a conclusion about the precision of the measurement of the missing transverse energy.

$$\Delta E_t^{miss} = 0.7 \cdot \sqrt{\sum E_t} \quad (E_t \text{ in GeV}) \tag{5.1}$$

The following events exhibit peculiarities:

- One event (7428,1110) failed the required selection because both tracks in the central detector are too short. This event was therefore not counted in calculating the cross section.

- One event (15951,770) failed the selection because the identified muon originally possessed to small a transverse momentum. If one eliminates the reconstruction problems in the central detector caused by overlapping tracks, a sufficiently high transverse momentum results. The other muon flew into a gap in the muon detector. One again, this event was not included in the calculation of the cross section. Nevertheless, because of its high two-muon mass we count it as a Z^0 event.

- One event (12039,1267) exhibits a two-muon mass, as measured in the central detector by itself, of only 53 GeV/c^2, but has missing energy.

A better measurement (see the chapter on the determination of the mass of the Z^0) yields a value of 91 GeV/c^2, with the calorimeter measurement also included in the calculation. Because of the low two-muon mass the event may also be taken to be a candidate for the reaction:

$$Z^0 \rightarrow \tau^+\tau^- \rightarrow \mu^+\mu^- + 4\nu$$

This event will be presented in more detail in the course of our discussion of the $\tau^+\tau^-$ background.

- Two events (6636,509 and 18517,1469) each have a two-muon mass of about 65 GeV/c^2. But in each event, near one of the muons there is also a high-energy photon. If one forms the three-body mass from the two muons and the photon, one finds values that are well compatible with the Z^0 mass. These two events will be discussed in more detail later.

5.2 The Sample Background

After the total efficiency was determined in the discussion on the selection of data, it is possible to decide the total event quantity of the reaction $Z^0 \rightarrow \mu^+\mu^-$. Up to now, however, it is not known whether the sample that was found is contaminated by unwanted reactions. Since the principal sources of background have already been presented earlier, we shall now determine what contribution they make to our sample.

5.2.1 Meson Decays

The background contribution that π and K decays contribute to the sample of events with high-energy muons was possible to calculate by means of a Monte Carlo study [78]. We start here with the inclusive hadron spectrum measured b UA1 [79] and a relative component of 58% pions and 23% kaons in this spectrum [80, 81]. The pion-to-kaon ratio may be considered to be constant over a wide momentum range [82].

It was determined that in the 411 events of 1985, in other words, the inclusive sample of the $p_t^\mu > 15$ GeV/c events, we must count on 1.7 events in which the muon actually stems from a decayed meson. However, these events will pass all the quality cuts and cause a muon trigger. Thus the background in this sample is 0.4%. The Z^0 events form a true sub-set of the ($p_t^\mu > 15$ GeV/c) sample. We make the assumption that the background is equally strongly represented in the muons of the Z^0 sample. It should be noted in this connection, that a Z^0 event will be mistakenly observed if even one of the two muons stems from a meson decay. In a total sample of 21 events, thus, we expect (21 events) x 0.8% = 0.17 ± 0.01 events as background due to meson decays.

5.2.2 Unabsorbed Hadrons

Hadrons that are incident on a calorimeter have two possibilities for causing a particle track in the muon detector, and thus imitate a muon. For one, it can happen that a hadron does not undergo any observed interaction in the calorimeter, or, as the second possibility, a hadronic cascade may penetrate all the way into the muon chambers.

Since our detector is at least 9 absorption lengths thick in all regions, the probability of finding a non-interacted muon in the muon detector is less than 10^{-4} per incident hadron, and is therefore negligible. Since we verify compatibility with minimum ionization in the calorimeters for our muons at the scan table, a hadronic shower could at most just be started in the very last part of the calorimeters. However, if that happens, it will exhibit high multiplicity in the muon chambers, and will be correctly identified there. The gaps in our apparatus due to the way they are designed are taken into account in the selection of the data. By means of a fiducial cut those events that exhibit activity in the gaps are separated out. Unabsorbed hadrons do not make any contribution to the background.

5.2.3 Cosmic Rays

It is possible for a background in the Z^0 data sample due to cosmic rays to arise if a high-energy muon passes through the detector at the time of the $p\bar{p}$ collision and happens to fly right through the interaction point. The part of the track which, starting from the vertex, correspond to the muon flying outward will be reconstructed exactly like a muon created by an inelastic collision. The part of the muon track leading from the point of incidence to the vertex will, however, be reconstructed as a particle leaving the vertex, but with reversed electric charge. Thus, such a cosmic-ray muon mimics a $\mu^+\mu^-$ pair that was created promptly. If one calculates the invariant mass of such an imitation pair, then, because of the high energy of the cosmic-ray muons and because the momentum resolution of our equipment becomes progressively poorer as the momenta increase, one will obtain a value for the invariant mass which, within the limits of error, will be quite compatible with the mass of the Z^0, typically 100 ± 50 GeV/c^2.

Initially it would appear as though such events would form a dangerous background to the Z^0 decays that result in the formation of $\mu^+\mu^-$ pairs. But a way exists for recognizing such events. For one thing, such false cosmic-ray muon pairs look like events where the muons are exactly collinear. Hence the false two-muon pair has vanishing transverse and longitudinal momenta in the detector system. This is very unlikely for a true Z^0, but not impossible. In the description of the selection process an automatic procedure in the off-line section is described that is capable of recognizing most of the cosmic muons [71].

For another thing, a cosmic-ray muon gives itself away by its transit time through the detector. In the 1984 data sample one event was selected, for which it is necessary to apply a subtle method to be able to see that, in reality, one is dealing with a cosmic-ray muon, rather than a Z^0. M. Schröder developed this procedure, which improves the quality of the reconstructed tracks in the muon chambers [83].

In this procedure the start time of the time digitizer is varied in a fitting process, and from this variation the χ^2 of the track is minimized. This is necessary in order to correct for the transit time of the signals along the anode wires in a given chamber; at the same time, this fit also compensates for local differences in the cabling. Once these local differences are known, this variation method may also be used to determine the true time point at which a particle passed through the chamber. If a cosmic-ray particle flies through the chamber it may arrive in one chamber at the same time as particles from the $p\bar{p}$ interaction, but in the other chamber there must necessarily be a time displacement by the amount of the flight time through the detector, typically 40 ns, which can be determined in the detector. For the questionable Z^0 event (13190,1019) this was the case . Fig. 5.4 shows the result of the fit in the muon chamber before and after the correction.

This procedure was thereafter used to test all Z^0 events. No events were found in the sample that stemmed from cosmic rays.

5.2.4 $\tau^+\tau^-$ pairs

$\tau^+\tau^-$pairs form an additional leptonic decay channel of the Z^0 with almost the same kinematics as in the muonic channel. However, the τ is very short-lived (3.4×10^{-13} s) and mainly decays hadronically. However the reaction $\tau \rightarrow \mu\nu\bar{\nu}$ also competes with a branching ratio B = 18.5% [84]. Hence $\tau^+\tau^-$ pairs represent a possible source of background in our sample. if both the taus decay into muons. If both muons and taus are coupled to the Z^0 with the same strength, this background is suppressed by $B^2 = 3.5\%$. To this it must be added that the tau decay is accompanied by the emission of two neutrinos. If the mass of the muon pair is reconstructed from the tau decay the resonance peak is no longer seen at the Z^0 mass but at about 35 GeV/c^2; the spectrum is also considerably broadened. Only at most a quarter of all events reach masses of more than 50 GeV/c^2. Thus, based on Monte Carlo calculations we would expect about 0.18 ± 0.04 such events in our sample.

Indeed, we observed one event (12039,1267) that is compatible with the reaction

$$Z^0 \rightarrow \tau^+\tau^- \rightarrow \mu^+\mu^- + 4\nu$$

This event has already been mentioned in the description of the data sample (see also [86]). Fig. 5.5 shows a view of this event in the transverse plane, together with the transverse energy and momentum vectors as well as the rapidity distribution of the muons, the jet in the event, and the neutrino, in other words, the distribution of the missing energy, corrected by the momentum carried off by the muons. The transverse momentum of the two-muon system, derived from the momenta in the central detector, amounting to 12.8 GeV/c, ius not completely compensated by the recoil jet on the other side, with a corrected transverse jet energy of 23.9 GeV. Two interpretations may be advanced for this topology:

1) If one assumes that we are observing the decay of a Z^o into two muons, the missing transverse energy of 19.5 GeV/c must correspond to the p^t of the Z^o, And indeed, within the error limits the transverse energy of the recoil jet does agree with this value. It is therefore possible that the neutrino shown in the plot is wrongly suggested by an erroneous momentum measurement of the muons in the central detector. If all the detector information is utilized, which ill be presented later in the mass determinations of the Z^o as "overall momentum fit" and energy balance, then the decay object has a probable mass value of 91 GeV/c^2.

2) Of the Z^o decays into a $\tau^+\tau^-$ pair, which in turn decays into muons and four neutrinos, the finding a two-muon mass of more than 50 GeV/c^2 is already not very probable. Furthermore, this interpretation is made even more difficult by the topology of the event. Since the two muons are found at an angle of almost 180° relative to each other, the taus should also have been generated at a large relative angle. But in such a case the energies of the four neutrinos would have to compensate mutually. The case where the resultant transverse energy of all four neutrinos sums up to 10 GeV is very rare.

Since the expected $\tau^+\tau^-$ rate in our sample is only about 0.2 events, and the topology of this event reduces the probability for a true $\tau^+\tau^-$ decay even more, we are of the opinion that this event should be assigned as a $Z^o \rightarrow \mu^+\mu^-$ event in which the muon momenta were poorly measured in the central detector.

5.2.5 Drell-Yan Pairs

The muon pairs in our sample are produced via the Drell-Yan mechanism. In this process the photon and the Z^o interfere with each other. The Z^o resonance sits on the continuum of electromagnetic production. The question may be posed how many muon pairs under the resonance come from a virtual photon instead of a Z^o, i.e. are part of the continuum rather than the resonance. Such muon pairs are indistinguishable in principle from muon pairs stemming from the Z^o decay due to photon-Z^o interference.

In Drell-Yan production the spectrum initially falls in proportion to M^{-3}. In addition the spectrum becomes even steeper due to the impact of the structure functions of the quarks. In our experiment the cross section for Drell-Yan pairs was measured, and the mass spectrum was parameterized in the range up to $M = 40$ GeV/c^2 [74, 85]. If one extrapolates this spectrum and multiplies by the acceptance of the Z^o selection, one would expect in the continuum 0.06 ± 0.024 events, allowing for a 40% error in the parameterization and the statistics of the Drell-Yan sample.

5.2.6 The Total Background

There are no other sources that could possibly deliver a significant contribution. The total background to the Z^0 decay for two-muon events with a mass $M_{\mu\mu} > 50$ GeV/c^2 is therefore estimated to be 0.4 ± 0.2 events.

Thus our data sample is practically without background.

5.3 Radiative Z° Events

In both collider experiments, UA1 and UA2, some events were observed whose physical interpretation is not completely clear to date. These events have topologies with two leptons and one high-energy photon, whose energy lies in the region about 30 GeV. [76, 124, 125, 60]. The mass of the three-body system lies astoundingly exactly at the Z^0 mass of 95 GeV/c^2. Table 5.2 lists the parameters of these 4 events. All the events pass the selections for the Z^0 in the corresponding channels, such as were described above, for example, for muons, since in all cases the momenta of the leptons alone are sufficiently large to form an unusually high mass. A total of 93 Z^0 events have been collected in either the UA1 or UA2 experiments to date which were detected by their purely leptonic decay.

It appears reasonable to ask, first of all, how well the three particles can be discriminated from each other. In the case of muons, this is easy, since the photon is recognized as energy deposition in the electromagnetic calorimeter without a charged-particle track in the central detector, while the muons are detected totally independently in the muon detector. Fig. 5.6 shows such an event.

In the UA2 event the three particles are recognized in the calorimeter, and, in fact, each of the three in different cells, so that here too the measurements are uncorrelated. The situation is different for the electron event in the UA1. While one lepton was easy to recognize in the CD and in the calorimeter, the other lepton poses a problem: The track in the central detector does not point directly to the center of mass of the energy deposition. The conclusion drawn from this fact is that in addition to the electron a hard photon was also emitted, and reconstructs the event parameters under this hypothesis. The lepton energy is taken from the CD measurement and the photon energy from the difference between the calorimeter measurement and the momentum measurement of the charge particle track in the central detector. This event thus has a somewhat smaller persuasive weight than do the other three.

It is notable that in the other cases the gamma energies agree astoundingly well (28.3 ± 1.0, 29.3 ± 1.0, and 24.4 ± 1.4 GeV). The topological similarity of the events (UA1: 18517,1469) and (UA2:C), both as to energy and as to angles, are equally confusing. The masses of the $l^+l^-\gamma$ system are compatible with the Z^0 mass within the limits of error. Using the total event samples the following proportions of the radiative events result:

$$\text{UA1},\mu\text{: } [2\ (\text{radiative})]/[21\ (\text{all})] = 0.095 \tag{5.2}$$

$$\text{UA1,e: } [1\ (\text{radiative})]/[33\ (\text{all})] = 0.030 \tag{5.3}$$

$$\text{UA2,e: } [1\ (\text{radiative})]/[39\ (\text{all})] = 0.026 \tag{5.4}$$

It must further be said that events with such topology would also be expected in the decay channels of the W, since these decay via the same Drell-Yan production mechanism at comparable momentum transfers. Nevertheless, the selections in the UA1 have to date found no radiative W candidates [126]. The search for exotic processes and radiative decays of the intermediate vector bosons in the UA2 has similarly failed to yield any W candidates [127].

5.3.1 Interpretation as Internal Bremsstrahlung

If one views the hard photon as the result of a bremssstrahlung, then it is necessary to distinguish between internal and external bremsstrahlung. The internal bremsstrahlung arises from the electromagnetic radiative corrections that contribute to the total reaction rate of the process $Z^0 \rightarrow \mu\mu\ (+\gamma)$. In the case of external bremsstrahlung it is a requirement that an outgoing lepton radiates off a brems-quantum due to the Compton effect. We have investigated both processes as possible sources.

We turn first to the internal bremsstrahlung for which there is a probability estimate by Berends et al., using a Monte Carlo method [128]. In this calculation a photon is considered hard if it has an energy greater than about 1.5 GeV. The calculation was based on a p_t spectrum of the W's or Z's, such as was measured in UA1, and a center-of-mass energy of 450 GeV. Only graphs to first order in the electromagnetic radiative corrections were used, virtual corrections by weak processes were neglected. Furthermore, only bremsstrahlung in the final state was considered.

We obtain the following result: In the electron channel a photon with energy greater than 20 GeV will be produced in 4% of all events. In the muon channel the number is 2%. Fig. 5.7 shows the fraction of the energy carried by the photon. The weak fall-off, starting as low as 5 GeV should be noted. The distribution of the angle between the photon and the nearest lepton is also very flat in the region between 10^0 and 90^0; this dependence is shown in Fig. 5.8. From the combination we can state for each event, with a pre-selected confidence, the probability for photons with at least the energy of the photon in the event, and which also have at least the angle of emission measured in the event, to be radiated off, by integrating over the probability distributions, starting with the measured values. With 95% confidence we obtain the following:

UA1(6636,509)(μ) $p_{\mathrm{intern}}^{\mathrm{Brems}} \approx 0.018$
UA1(18517,1469)(μ) $p_{\mathrm{intern}}^{\mathrm{Brems}} \approx 0.017$
UA1(6059,1010)(e) $p_{\mathrm{intern}}^{\mathrm{Brems}} \approx 0.020$
UA2(c)(e) $p_{\mathrm{intern}}^{\mathrm{Brems}} \approx 0.017$

For its event UA2 arrived at the same result [129].

Fleischer and Jegerlehner performed an analytic calculation [130]. Electroweak first-order terms (1 loop) were also taken into account, as well as effects stemming from the emission of several lighter photons. In carrying out the integration over the energy of the photons and the angle of emission, they neglected terms of the order $O(\alpha(m_l^2/M_Z^2)$ and higher. The production probability calculation uses the minimum energy that a photon must have in order to be identified with certainty as a photon. In the UA1 this threshold lies at about 18 - 20 GeV. The approximations used in the calculations done to date, that the photon energy is negligible in comparison to M_Z, are no longer valid for energies of this magnitude. Therefore these authors come to a result about 10% higher than that found in UA1 and UA2 [128, 129].

We can now calculate the total probability W, that k gamma events appear in a sample of n Z^o-events, if the individual probabilities p are known:

$$W(k,n,p) = \binom{n}{k} \cdot p^k \cdot (1-p)^{n-k} \tag{5.5}$$

With the assumption of this Poisson distribution, with which an explanation based on internal bremsstrahlung applies, the following total probabilities result:

- 1 event with $p = 0.020$ at UA1 in the electron channel out of a total of 33: $W = 35\%$

- 1 event with $p = 0.017$ at UA2 in the electron channel out of a total of 39: $W = 35\%$

- 2 events with $p = 0.018$ at UA1 in the muon channel out of a total of 21: $W = 4.8\%$

- The probability that all 4 events stem from internal bremsstrahlung amounts to: $W = 6.1\%$

Thus internal bremsstrahlung represents an acceptable explanation of our radiative events.

5.3.2 Interpretation Via External Bremsstrahlung

The probability for external bremsstrahlung can be calculated in the final state if one knows the mass of matter that the outward-bound leptons have passed through; this matter consists particularly of the walls of the beam tube and the central detector; In the region of interest to us these amount to between 0.02 and 0.04 radiation lengths [132]. According to Rossi and Greisen [133] the probability for the appearance of a photon of energy k, from an electron of energy E, after passing through x radiation lengths of material, under external bremsstrahlung, in the limit case of "complete screening" is calculated to be:

$$P(E,k)dk = x\frac{dk}{k}F(E,k) \tag{5.6}$$

$$F(E,k) = 1 + \left(1-\frac{k}{E}\right)^2 - \frac{2}{3}\left(1-\frac{k}{E}\right) + a\left(1-\frac{k}{E}\right) \tag{5.7}$$

$$a = \frac{1}{9\ln\left(\frac{183}{Z^{1/3}}\right)} \tag{5.8}$$

$$= \frac{1}{37.5} \text{ (für unseren Apparat)} \quad \text{(for our machine)} \tag{5.9}$$

If we integrate over the photon energy from 20 GeV up to the maximum electron energy of 70 GeV, then the probability that an electron makes external bremsstrahlung turns out to be a few percent. However, this bremsstrahlung is emitted with a strong preference in the direction of the lepton. The mean scattering angle here does not depend on the energy of the photon, but only on the energy and mass of the lepton:

$$\langle\theta\rangle = \frac{mc^2}{E_l} \tag{5.10}$$

For muons in our energy range this angle is always less than 1 milli-rad.

A Monte Carlo calculation was performed for the muon events. For an angular range which typically corresponds to the size of a calorimeter cell, the entire photon energy was collected together. The external bremsstrahlung is summed; internal bremsstrahlung is excluded. Photons that fall within this angle window from the underlying event are also added, as are photons from a Landau distribution that describes the energy loss of the muons in the calorimeter. Fig. 5.9 shows the dependence; it will be seen that photons with an energy of about 30 GeV occur with a probability of less than 0.01%. We therefore rule out external bremsstrahlung as cause of the radiative events.

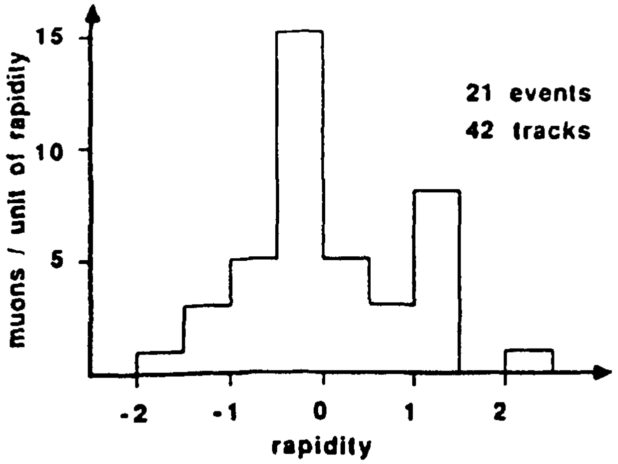

Fig. 5.1: The Rapidity Spectrum of the Muons from Z^0 Decay

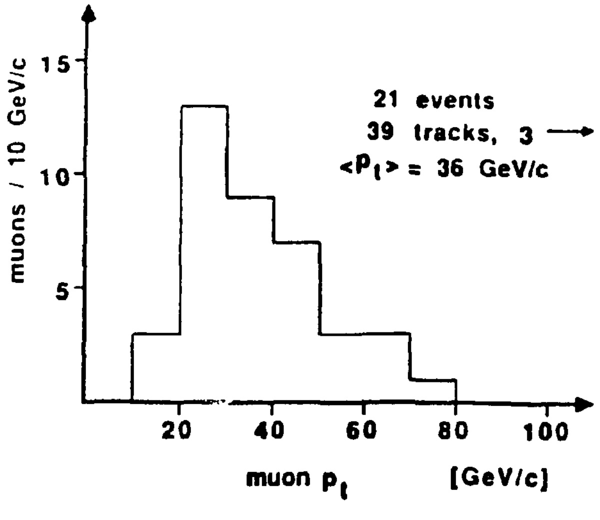

Fig. 5.2: Transverse Momentum Spectrum
of the Muons from Z^0 Decay

The plot shows the transverse momenta as determined solely from the measurement in the central detector. In the mass determination of the Z^0 the improved momenta from the "Overall Momentum Fit" are used.

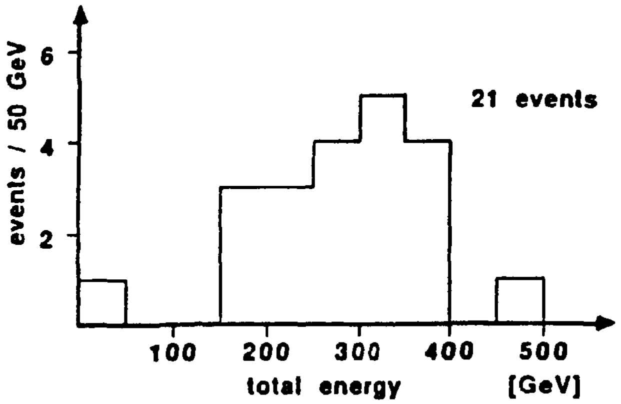

Fig. 5.3: The Total Calorimeter Energy in Z^0 Decays

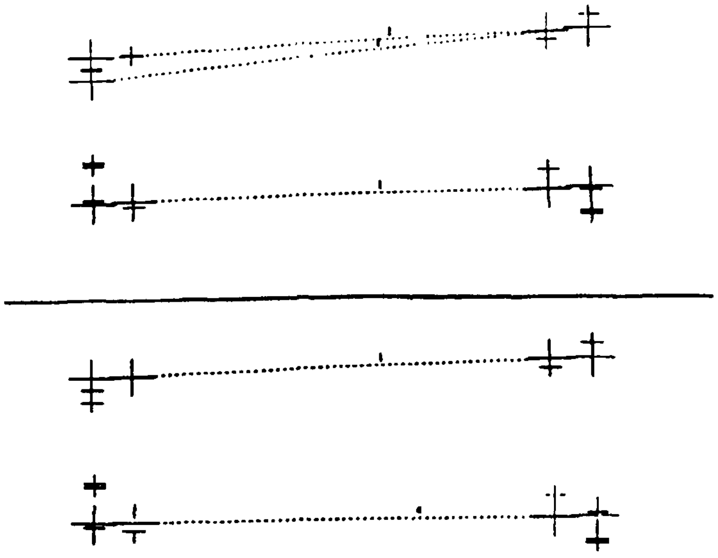

Fig. 5.4: Hit Distribution Before and After the Time Fit in the Chamber

The cosmic-ray origin of the track can be inferred from the variation of the start time of the event. The upper image shows, for both projections, the hits and the reconstructed tracks before the time variation fit; the lower image shows it after the time variation fit. It will be noted that, first, the track ambiguity in the one projection is resolved, and that in the other projection the χ^2 of the track is decreased. This makes it quite clear that the particle creating the track did not fly through the apparatus exactly at the moment of the $p\bar{p}$ collision. It can only be a cosmic-ray muon [83].

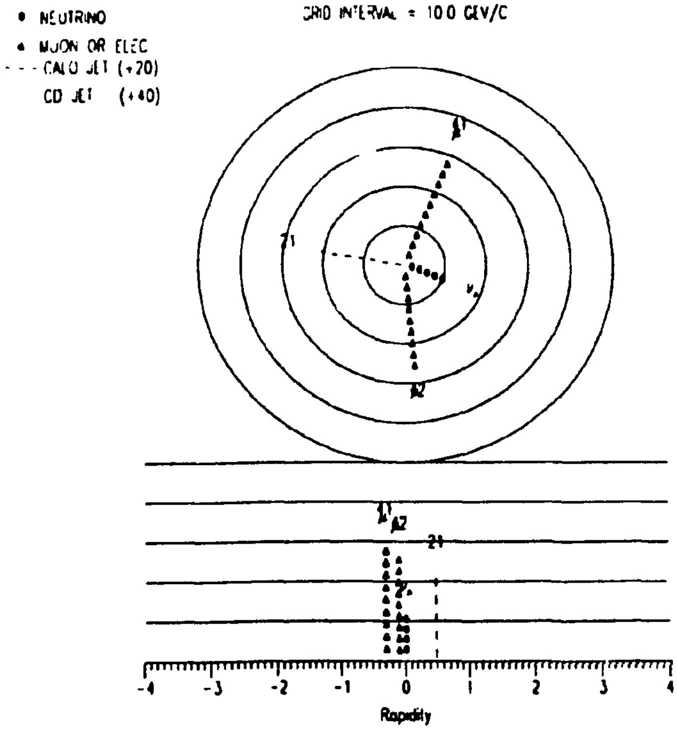

Fig. 5.5: View of Event (12039,1267)

The momenta of the muons, the energy of the recoil jet, and of the supposed neutrino are shown. The top diagram shows the transverse plane, the lower figure shows the event along the rapidity axis.

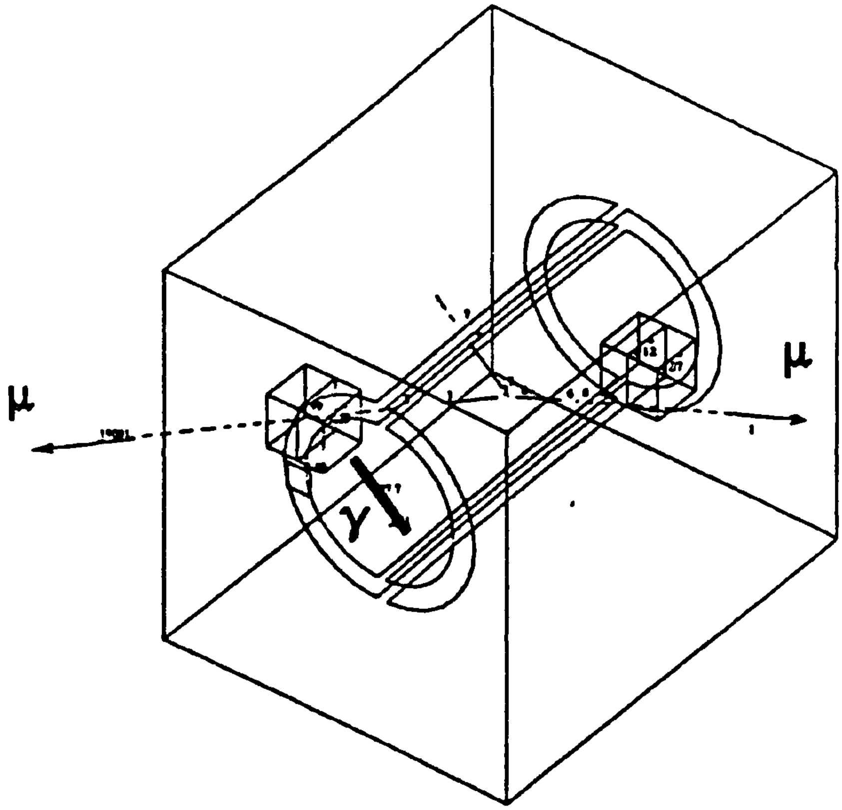

Fig. 5.6: View of the Radiative Z^0 Candidate

(UA1:18517,1469) $Z^0 \rightarrow \mu\mu\gamma$.

The photon lies closely beside the muon in the gondola. It can be recognized by the large energy deposition in the electromagnetic calorimeter.

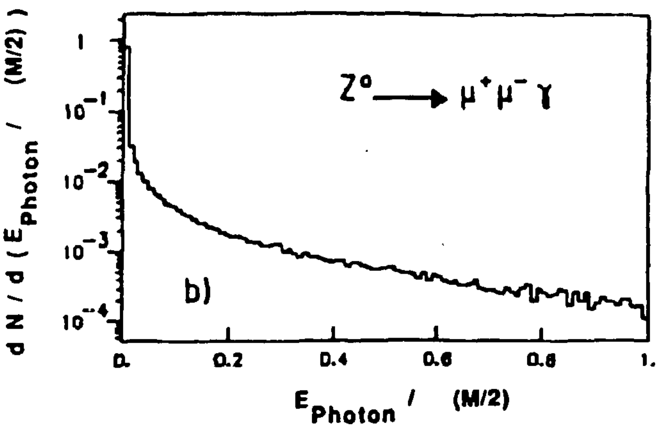

Fig. 5.7: Energy Distribution of the Photon in Internal Bremsstrahlung

The integral of the distribution is normalized to 1. (From [128]).

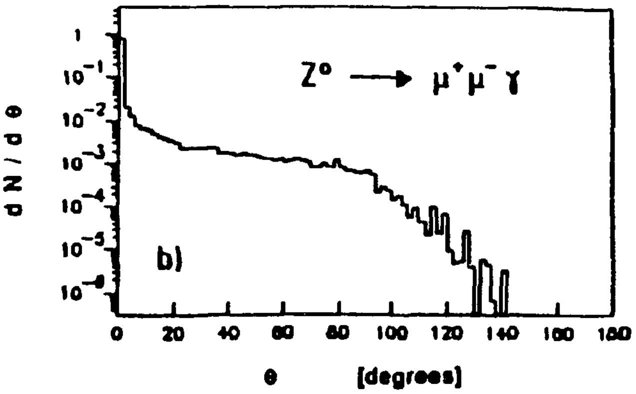

Fig. 5.8: Angle Distribution Between the γ and the Nearest Lepton

The integral of the distribution is normalized to 1. (From [128])

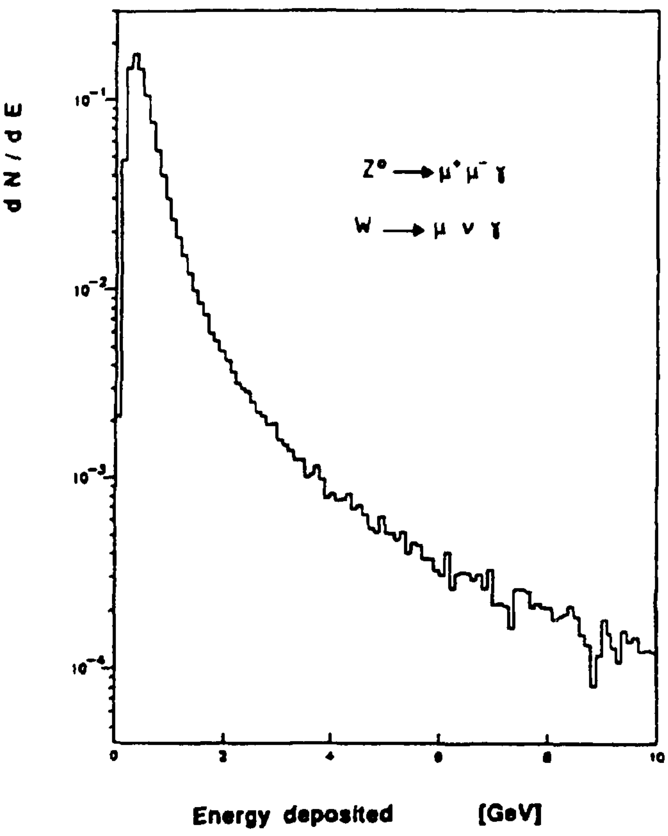

Fig. 5.9: Probability of External Bremsstrahlung for $Z^0 \to \mu\mu$

The plot also contains photons from the underlying event, as well as Landau fluctuations in the energy deposition of the muon in the calorimeter. The integral of the distribution is normalized to 1. (From [128])

Ⓐ	Ⓑ	Ⓒ	Ⓓ	Ⓔ	Ⓕ	Ⓖ	Ⓗ	Ⓘ
Run/ Ereignis	Ladung · Impuls [GeV/c]	Transv.- Impuls [GeV/c]	Rapi- dität	M (Z0) [GeV/c/c]	Pt (Z0) [GeV/c] kalorim.	E total [GeV]	Trans.- En.(tot) scal.	Neu- trino [GeV]
6219/	33 +/- 5	21	-1.0	74	12	392	81	22
947	-43 +/- 9	34	0.6	+/- 10				
6600/	62 +/- 7	34	1.1	209	19	162	44	162
22	-211 +/- 30	204	-0.2	+/- 152				
6636/	57 +/- 2	23	-1.5	66	64	397	87	71
505	-32 +/- 14	32	-0.2	+/- 14				
7428/	35 +/- 20	33	-0.1	130	6	308	33	84
1110	-127 +/- 300	123	-0.2	+/- 158				
8523/	51 +/- 7	37	-0.8	82	2	269	25	2
831	-41 +/- 13	41	-0.1	+/- 15				
9323/	73 +/- 36	71	-0.2	116	11	162	27	36
93	-48 +/- 14	48	-0.1	+/- 33				
10605/	49 +/- 29	43	-0.5	96	7	301	46	33
890	-50 +/- 5	27	1.2	+/- 29				
11619/	32 +/- 3	25	-0.7	87	13	310	60	8
518	-61 +/- 5	29	1.3	+/- 6				
12039/	29 +/- 5	28	-0.3	52	20	186	46	10
1267	-26 +/- 9	26	-0.1	+/- 10				
12287/	52 +/- 2	22	1.4	104	0.3	294	27	9
30	-53 +/- 16	31	-1.1	+/- 16				
12530/	31 +/- 8	28	-0.4	98	10	302	55	15
937	-83 +/- 19	47	1.1	+/- 17				
15621/	-249 +/- 489	249	0	266	11	278	55	190
137	-74 +/- 35	67	-0.4	+/- 269				
15951/	86 +/- 3	22	-2	144	9	322	34	39
770	-67 +/- 48	54	0.7	+/- 51				
16039/	107 +/- 19	42	-1.6	81	5	236	30	42
474	-16 +/- 2	12	0.8	+/- 8				
16201/	57 +/- 6	32	1.1	80	15	361	60	90
30	-78 +/- 13	50	1	+/- 8				
17027/	43 +/- 21	43	-0.1	75	12	495	72	24
255	-33 +/- 7	33	-0.1	+/- 21				
18046/	45 +/- 36	42	-0.3	108	15	267	33	8
99	-64 +/- 33	62	0.2	+/- 51				
18451/	68 +/- 10	28	1.4	74	23	363	101	18
851	-22 +/- 4	18	-0.8	+/- 9				
18517/	55 +/- 25	55	0	65	20	202	35	21
1469	-22 +/- 7	18	-0.6	+/- 60				
18580/	116 +/- 18	61	1.2	133	11	201	27	13
344	-41 +/- 10	36	-0.5	+/- 19				
19208/	125 +/- 13	27	2.2	78	1	46	10	4
17	-24 +/- 6	24	0 2	+/- 10				

A:	Run/ Event
B:	Charge Momentum [GeV/c]
C:	Transv. Momentum [GeV/c]
D:	Rapi- dity
E:	$M(Z^o)$ [GeVc/c]
F:	$P_t(Z^o)$ [GeV/c] Calorim.
G:	E_{total} [GeV]
H:	Transv. En.(tot) scalar
I:	Neu- trino [GeV]

Table 5.1: Some Properties of All the Z° Candidates

The parameters shown are the momentum, transverse momentum, and rapidity of the muons, measured in the central detector, after removal of all reconstruction problems; also shown are the mass of the two-muon system and the transverse momentum of the Z°, as determined with the aid of the calorimeters. The Table also contains the total calorimeter energy, the scalar sum of the transverse energies of all calorimeter cells, and the missing energy, which is here designated as neutrino, for short. The large missing energy in Event (6636,509) is due to a problem in one calorimeter cell.

Z0 gamma		83 mu	85 mu	83 el	83 el
Experiment		UA1	UA1	UA1	UA2
Run Nr		6636	18517	8059	
Ereignis Nr		509	1469	1010	C
pos. Lepton	1/p	0.0176	0.0182		
	d 1/p stat	0.0006	0.0326		
	d 1/p sys	0.0025	0.0079		
	d 1/p	0.0026	0.0308		
	p	56.94	54.82	62.60	69.90
	dp	8.37	92.42	1.58	1.80
	px	-52.16	-2.80	35.44	-60.72
	py	-18.97	21.98	47.52	-26.57
	pz	-15.37	50.10	20.12	-22.22
	pt	22.90	54.71	51.60	34.64
neg. Lepton	1/p	0.0310	0.0511		
	d 1/p stat	0.0130	0.0130		
	d 1/p sys	0.0085	0.0095		
	d 1/p	0.0148	0.0152		
	p	32.30	19.58	8.86	11.40
	dp	15.20	5.81	1.40	0.70
	px	-6.88	-11.47	2.06	1.63
	py	17.50	-2.58	-7.37	5.73
	pz	26.26	-15.65	-4.45	9.72
	pt	31.56	15.86	8.61	11.28
Photon	Et	10.01	18.35	41.73	23.96
	dEt	0.90	0.00	1.29	
	E	28.30	29.30	42.90	24.40
	dE	1.06	1.08	1.31	1.40
	Ex	-26.47	-22.90	9.95	4.66
	Ey	-4.70	-13.80	-39.38	21.21
	Ez	-8.83	-12.10	-13.82	11.14
Winkel	cos1	-0.1859	-0.7533	-0.6619	-0.5863
	theta l+l-	100.7	138.9	131.4	125.9
	cos2	0.9906	-0.5265	-0.6690	-0.6415
	theta l+g	7.9	121.8	132.0	129.9
	cos3	-0.1445	0.8501	0.9801	0.8535
	theta l-g	98.3	31.8	11.5	31.4
Massen	mass l+l-	66.04	61.35	42.92	50.28
	d mass l+l-	16.28	52.51	3.44	1.67
	mass l+g	5.51	70.02	94.69	74.83
	d mass l+g	0.42	59.05	1.88	2.35
	mass l-g	45.74	13.11	3.89	9.03
	d mass l-g	10.80	1.96	0.31	0.38
	mass l+l-g	80.53	94.02	104.03	90.60
	d mass l+l-g	14.69	55.75	2.22	2.15

A:	Z° gamma
B:	Experiment
C:	Run Nr.
D:	Event Nr.
E:	Angle

Table 5.2: Event Parameters of the Radiative Z° Candidates

The Table shows the momenta and energies of the leptons and the photon, as well as the angle in space of the three particles relative to each other and the masses of the two- and three-body systems with their errors.

Chapter 6

The Production Properties

6.1 The Partial Production Cross Section

The number N of observed events $Z^0 \rightarrow \mu^+\mu^-$ depends on the coupling strength of the fermions to the Z^0, as well as the matrix element and the branching ratio of the muonic channel. In our experiment we can determine only the product of these parameters for the $Z^0 \rightarrow \mu^+\mu^-$ reaction, in other words, the cross section times the branching ratio. We shall henceforth describe this product as the partial production cross section. We obtain:

$$(\sigma \cdot B)_{Z^0} = \frac{N}{\epsilon \cdot L} , \tag{6.1}$$

where L is the integrated luminosity and ϵ is the total efficiency of our trigger, the apparatus, and the selection. N is the number of events corrected for the background. Measurements were done at two different center-of-mass energies, namely 546 GeV and 630 GeV. Thus we are in a position to test not only the absolute prediction of the theory [87], but also the dependence of the partial production cross section on the center-of-mass energy. Table 6.1 contains a summary of the W and Z samples collected in the UA1 and the UA2.

For the reaction $Z^0 \rightarrow \mu^+\mu^-$ we obtain, individually:

- $\sqrt{S}$ = 546 GeV: 4 events that fall within the described acceptance were observed; one event failed the selection process since both tracks in the central detector are too short. The efficiency is 37 ± 5 %, the background 0.07 ± 0.03 events, and the integrated luminosity is 108 ± 16.2 nb^{-1}.

$$(\sigma \cdot B)^{546}_{Z^0} = 98.4 \pm 49.8_{(stat.)} \pm 19.9_{(syst.)}\,\mathrm{pb} \tag{6.2}$$

- $\sqrt{S}$ = 630 GeV: 15 events were observed; one event failed the selection process, since one muon did not hit the muon detector, and the other muon was initially reconstructed with too low a transverse momentum, due to overlapping tracks in the central detector. The efficiency is 40.1 ± 3 %, the background is 0.34 ± 0.16 events, and the integrated luminosity is 555 ± 83.3 nb^{-1}.

$$(\sigma \cdot B)^{630}_{Z^0} = 65.9 \pm 17.2_{(stat.)} \pm 10.9_{(syst.)}\,\mathrm{pb} \tag{6.3}$$

The statistical error arises solely from the number of events. The systematic error contains uncertainties in the acceptance calculation and, as the main source of error, the systematic error in the luminosity measurement, which amounts to 15%.

One expects an increase in the cross section of about 25% as the center-of-mass energy increases. The theoretical calculation [87] yields:

$$(\sigma \cdot B)^{546}_{Z^0} = 44^{+14}_{-8}\,\mathrm{pb} \tag{6.4}$$

$$(\sigma \cdot B)^{630}_{Z^0} = 53^{+17}_{-11}\,\mathrm{pb} \tag{6.5}$$

Thus both the partial production cross sections lie slightly above the expected values. However, within the error bars we find that they agree with the predictions. The uncertainties in the prediction stem from a lack of information about the actual structure functions and model dependencies in the higher-order terms, which need to be added to the simple Drell-Yan process to describe the radiative emission of gluons [35, 87]. Since the mass of the top quark is still unknown, this quark mass enters into the errors in the theoretical calculation as an unknown parameter. We assume that the Z^o cannot decay into t^+t^-, and that no top quark can be generated in the W decay ($M_{Top} > 80$ GeV/c^2).

6.2 Comparison with Other Measurements

A comparison with the results from the electron channel in our experiment [88], and with the UA2 [89] shows that the theory yields somewhat smaller values in every case [87]; nevertheless, our measurements agree quite well, within the errors, with the theory. Table 6.2 shows the partial production cross sections from both experiments for the Z^o . Fig. 6.1 brings together all the partial production cross sections for the Z^o and the W.

The large difference from theory in the UA1 muon channel and in the electron channel at the UA2 at low center-of-mass energy may be interpreted as statistical outliers. Table 6.1 summarizes the signal, background, and acceptance for all channels. It will be observed that, due to the poorer acceptance, the muon channel is inferior to the electron channel with respect to precision, since fewer events were recorded, and hence the statistical error is greater. The UA2 measurements exhibit a smaller systematic error, since at that experiment the luminosity is determined twice as accurately as at the UA1. An improvement in the statistics, which is to be expected under the future operating conditions of the collider, will not contribute significantly to the improvement of these measurements until success is attained in reducing the systematic error in the luminosity determination at the UA1. Furthermore, the acceptance in the muon channel should be improved. Unfortunately, there seems hardly any possibility for improving the solid-angle coverage of the UA1 detector with muon chambers. We are therefore trying to improve the acceptance of the 1-muon trigger, which will also increase the efficiency for the Z^0 muon channel. The W selection in the muon channel is described in detail in [116].

6.3 Quantum Chromodynamics Effects

Intermediate vector bosons are, in first order, produced via the electroweak interaction via the Drell-Yan process of quark-antiquark annihilation. At our center-of-mass energy and momentum transfer of about 100 GeV/c, the annihilation of valence quarks dominates; the probability for the fusion of sea quarks is minor, typically a few percent [35, 87]. The longitudinal momenta of the bosons yield the product of the parton momentum distributions for momentum transfers of the order of magnitude of the W and Z masses. In the simple Drell-Yan picture the bosons will carry at most a small amount of transverse momentum, which stems from the transverse Fermi motion of the quarks before the collision, and which may perhaps be a few hundred MeV/c. An event of this type is shown in Fig. 6.2. The low activity, both in the calorimeter and in the central detector are very noticeable. Aside from the two muons from the Z^0, no charged track with a momentum greater than 2 GeV/c is to be seen. Apparently the quarks and muons that did not participate in the hard collision escaped in the forward and backward directions through the beam tube.

Since the quarks carry strong color charge, they also couple to the gluons in the nucleon. In a hard collision process a quark may very easily evaporate off a hard gluon as bremsstrahlung. Inversely, a gluon may create a quark pair before the collision, one of these quarks plays a part in the creation of the boson, the other escapes as a hadron. It is true that this Compton term is of lesser significance; it amounts to only about 10% of the gluon bremsstrahlung at our center-of-mass energy [35, 87].

Both this Compton effect and the gluon bremsstrahlung can lead to high-energy recoil products, which are observable as jets. In order to satisfy the conservation of momentum the boson must then also receive a corresponding transverse momentum in the opposite direction. This may lead to an extensive tail in the transverse momentum distribution of the boson. An example of a very active event is shown in Fig. 6.3. Several jets can be reconstructed from the large number of tracks and the calorimeter cells.

We are therefore in a position to recognize deviations from the simple Drell-Yan picture of the production of vector bosons, caused by effects of the strong interaction. We may thus be able to test the predictions of quantum chromodynamics in our energy range. The leptonic decay channels of the bosons are especially well suited for these investigations, since in the final state no quantum chromodynamic effects occur, and the production properties therefore come very clearly into view.

All the theoretical calculations need the momentum distribution of the quarks in the nucleus as input. It therefore makes sense to check, first of all, whether the parameterized structure functions derived from the data of other experiments [92, 93] are compatible with our Z^0 events.

6.3.1 The Longitudinal Motion of the Z^0

The longitudinal motion of the Z^0 can be calculated from the longitudinal momenta of the outgoing leptons since the center-of-mass energy S is known. It reflects, simultaneously, the difference in the structure functions of the annihilating quarks:

$$\begin{aligned} x_Z &= \frac{p_l^{\mu^+} - p_l^{\mu^-}}{\sqrt{S}/2} \\ &= x_q - x_{\bar{q}} \end{aligned} \tag{6.6}$$

From conservation of energy it also follows that:

$$x_q \cdot x_{\bar{q}} = \frac{M_Z^2}{S} \tag{6.7}$$

This yields a mean x_q of 0.17 at $\sqrt{S}$ = 546 GeV, and a value of 0.15 at $\sqrt{S}$ = 630 GeV. The reacting partons are mainly the valence quarks of the proton and the antiproton. Quarks from the sea can be neglected to first order.

In contrast to the case of the W event sample, in the case of the Z^0 decays we are not in a position to recognize whether u or d quarks participated in the inelastic collision [116, 94]. Thus we can say nothing about the structure functions of the individual types of quarks; we see only a superposition of the structure functions of all the participating partons.

In calculating the x_Z we come upon the difficulty that the momenta of the muons, as measured in the central detector, exhibit large errors, and that even a determination of the sign of the charge from the curvature of the track in the magnetic field is not always possible. We therefore use the previously presented "overall momentum fit" which makes use of the deflection of the muon track and its displacement after passing through the iron absorber to yield an improved momentum measurement.

In addition, we apply a new procedure, based on the topology of the Z^0 events, namely the energy balance in the transverse plane. By requiring that in our Z^0 events the remaining missing transverse energy corresponds, within the limits of error, to the transverse momentum of the Z^0, and not to a hypothetical neutrino, we can improve the determination of the muon momenta. The three-dimensional momentum vectors are scaled to the two-dimensional transverse plane by such a balance, which also results in a better determination of the longitudinal components of the muon momenta. To do this we force the decay object, the Z^0, to have a mass of 90.1 GeV/c^2, as we measured it to be in the muon channel. Thus we define a χ^2 which is then minimized:

$$\chi^2 = \left[\frac{(\frac{1}{\hat{p}_1}) - (\frac{1}{p_1})}{\sigma(\frac{1}{p_1})}\right]^2 + \left[\frac{(\frac{1}{\hat{p}_2}) - (\frac{1}{p_2})}{\sigma(\frac{1}{p_2})}\right]^2 + \left[\frac{\hat{E}_m^y - E_m^y}{\sigma(E_m^y)}\right]^2 + \left[\frac{\hat{E}_m^x - E_m^x}{\sigma(E_m^x)}\right]^2 \tag{6.8}$$

(6.9)

where the parameters with the symbol ^ are the parameters to be fitted, from which the measured parameters are subtracted. The fit is performed under the following boundary conditions:

$$E_m^y = p_1^y + p_2^y \tag{6.10}$$

$$E_m^x = p_1^x + p_2^x \tag{6.11}$$

$$\begin{aligned} M_Z &= 90.1 \text{ GeV}/c^2 \\ &= 2p_1p_2(1 - \cos(p_1, p_2)) \end{aligned} \tag{6.12}$$

From this minimization we obtain the best possible muon momenta, which are used to calculate the x_Z. We then eliminate all events in which the charge of the muon could not be determined with certainty. The momentum error can be so large that within one 1σ band $p_\mu - \sigma(p_\mu) < p_\mu < p_\mu + \sigma(p_\mu)$ the signs changes. We cut off at: $p^\mu < 2\sigma(p^\mu)$. The radiative Z^0 candidates are also excluded. Then a weight is assigned to each event; the weight corresponds to the inverse of the acceptance for Z^0 events with the transverse momentum of the event in question. The acceptance dependence on the transverse momentum of the Z^0 has already been presented in the chapter on selection.

12 events remain in the muon channel. They are combined with the 21 events from the electron channel, which are treated identically except for the momentum determination of the leptons. For electrons the momentum can be determined with sufficient accuracy from the electromagnetic calorimeter and the central detector. The x_Z distribution is shown in Fig. 6.4, together with a Monte Carlo prediction which was produced with the ISAJET computer program. In ISAJET the structure functions of Eichten et al. [92] were used, as well as $\lambda_{QCD} = 0.2$ GeV. It is seen that the data are not sensitive to the difference between the two center-of-mass energies, over which we averaged here. Within the error limits the agreement of the measured data with the prediction is good.

6.3.2 The Transverse Motion of the Z^0

The existing quantum chromodynamics calculations of higher order in α_s are based on the fact that the hadrons that are also produced in the production of the vector bosons may be divided into two classes. The first group contains all fragmentation products from the quarks and gluons that participated in the hard collision. For these there now exists a fairly large number of calculations and descriptions based on Monte Carlo methods [34, 87, 123, 95, 96, 97, 98, 99]; these work reliably, especially in the domain of high transverse momenta of the vector bosons. In these calculations various methods are used for integrating over the momentum contributions stemming from soft gluons.

In the second group we find all particles resulting from the interactions of the rest of the incoming partons, the spectator quarks and gluons. While these partons do not contribute to the transverse momenta of the bosons, they do at times make considerable contributions to the transverse energy balance of an event, especially when they manifest themselves as jets. Unfortunately, there are no similarly reliable calculations available for these hadrons, at best we can assume parameterizations which we have ourselves obtained from our minimum-bias data.

Experimentally the reconstruction of the transverse momentum of a vector boson from the outgoing leptons is possible with high precision only in the case of the electronic decays of the Z^0. In the muonic channel the momentum resolution is too poor. In the reconstruction of the W's one runs up against the additional difficulty that a high-energy neutrino leaves the detector without depositing energy or momentum [116, 94]. We therefore decided, for reasons of efficiency, to treat the decay channels of both the charged and neutral bosons in the same manner. We take the missing transverse energy in the detector E_t^m as a measure of the transverse momentum of the vector bosons.

The raw measurement of E_t^m must still be corrected: First the energy deposited by the outgoing leptons in the calorimeter is subtracted in order not to count this contribution twice. For muons this correction is minor, since they are minimum-ionizing particles.

Then a test is made to see whether jets are present in the event. Analogous to the procedure used in the search for the top quark, we changed the definition of a jet, as compared with the standard definition in the UA1 for the purpose of the W/Z analysis. The minimum jet energy was reduced to 7 GeV. In order to protect against accidental energy clusters we require a charged track with $p_t^{track} > 0.5$ GeV/c within a cone of $\Delta R \leq 0.4$ around the jet axis.[6] Using the ISAJET Monte Carlo code we calculated the efficiency of this definition on the basis of $W \rightarrow e$ events, and found it to be 74 ± 3 %. We know also that the inefficiency lies mainly in the region of small E_t^{Jet}; above 15 GeV we are almost completely efficient. We estimate the contamination due to fluctuations of the underlying event to be about 10%. However, the measured jet energy differs from the true jet energy because of the limited resolution of our calorimeter. The necessary corrections were also done using the ISAJET computer program.

It turns out that an equivalent method can be applied for correction of the jets, by modifying the E_t^{miss} distribution by means of a global acceptance and resolution function. Both event fluctuations and also poorly measured jets will finally always lead to values of E_t^m different than 0. If one sets E_t^m equal to the transverse momentum of the vector bosons, the p_t spectrum will appear distorted due to this effect (see Fig. 4.5). With the aid of the ISAJET program and the detector simulation it is possible to study this distortion and thus produce a p_t-dependent acceptance. The data can then be corrected by applying the inverse to the distortion function. Both methods yield consistent results; the corrections are less than 30%. All the corrections are known to a precision of about 10 - 15 %. We assume that the systematic uncertainty on the energy scale is 9%.

Now the missing transverse energy, and hence $p_t(Z^o)$ can be finally computed; Fig. 6.5 shows the spectrum. We observe transverse momenta up to 35 GeV/c. The theoretical curve stems from Altarelli [87], who set $\lambda_{QCD} = 0.2$ GeV, and

---

[6] A reminder: $\Delta R = (\Delta\eta^2 + \Delta\phi^2)^{1/2}$.

used set 1 of the structure functions by Duke and Owens [93]. In the case of the W analysis [116] this choice of parameters yielded the best agreement with the data. The agreement between the data and the theory is satisfactory within the framework of error.

We find a mean transverse momentum of the Z^0 amounting to $<p_t> = 9.7 \pm 1.2$ GeV/c. This figure is obtained by averaging over both leptonic decay channels and over both center-of-mass energies. According to Altarelli the mean transverse momentum in the Drell-Yan production of lepton pairs should increase linearly with increasing center-of-mass energy S [100]:

$$\langle p_t \rangle \propto \alpha_s \sqrt{S} f(\alpha_s, \tau) \tag{6.13}$$

where α_s is the strong coupling constant, and $f(\alpha_s, \tau)$ is a function of α_s at a constant mass of the annihilating $q\bar{q}$ pair of $\tau = x_1 x_2 = M^2/S$. This, if τ is kept fixed we get

$$\langle p_t \rangle \propto \alpha_s \sqrt{S} \tag{6.14}$$

Fig. 6.6 shows this dependence. The calculation for $\sqrt{\tau} = 0.22$ may be compared with data points in the range of $\sqrt{\tau} = 0.13 - 0.17$; within the limits of error the agreement between the prediction and the data is good. Above $\sqrt{S} = 100$ GeV one sees the linear relationship. It is worth noting that the parameterization of Fermilab energies over the ISR region is well fitted up to 630 GeV.

As p_t increases we observe a more frequent occurrence of jets; above p_t = 16 GeV/c all the events have one or more jets (see Fig. 6.5). After the theoretical descriptions of the production properties of the vector bosons so far described turned out so successfully, it seemed reasonable to investigate the jets more closely. Because of the poor statistics we limit ourselves to investigating the jet multiplicity. Fig. 6.7 shows the observed distribution of the jet multiplicity, together with the

ISAJET prediction. Several jets were produced in a single event in the Monte Carlo program due to the inherent radiative emission of many gluons, rather than due to the explicit simulation of processes to higher-order in α_s (see also Appendix B). Nevertheless, ISAJET describes the multiplicity correctly within the errors; the ISAJET method is entirely justifiable theoretically. A theoretical calculation by Ellis et al. [101], which explicitly includes higher orders, shows that the production of a second jet is not correlated with the production of the first jet, if one ignores the decrease in the energy available.[7] For the probability of finding N jets, one has

$$p(N\ Jets) = p^N(1\ Jet) \tag{6.15}$$

Both our data and the ISAJET Monte Carlo computer code results are thus in agreement within our errors and our resolution.

---

[7] This holds specifically only for our geometry and the cut-off criteria used for the boson selection at the UA1.

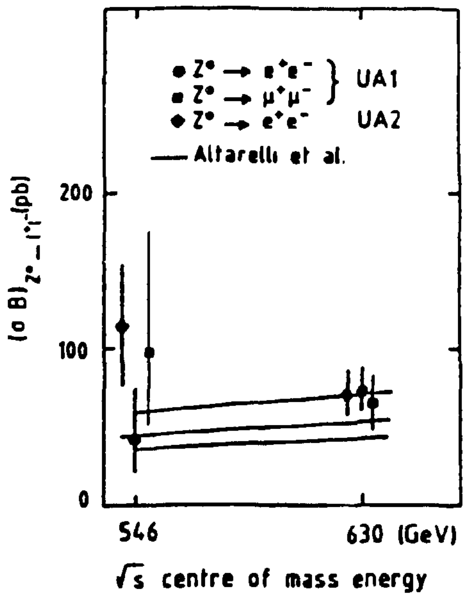

Fig. 6.1: The Partial Production Cross Sections of the Neutral Vector Bosons

The theoretical prediction is the middle one of the three lines; its uncertainty is shown by the upper and lower lines. It stems from Altarelli et al. [87].

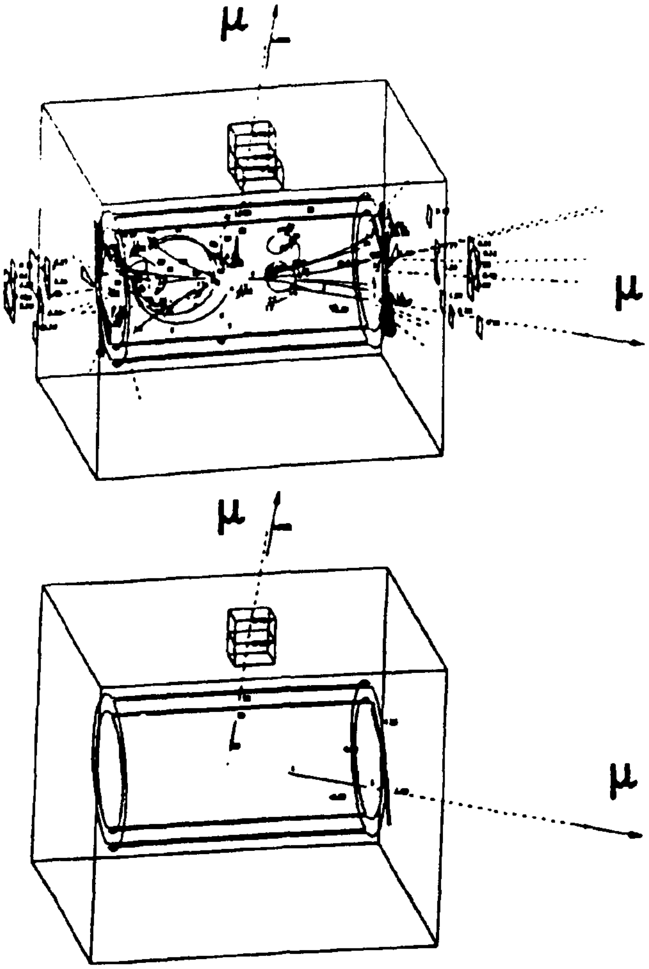

Fig. 6.2: A Quiet Z^0 Event (19208,17)

The figure shows a perspective view of the event; the upper diagram does so without any cut-off criteria for either the energy or the momentum of the particles, the lower figure shows the same event with a cut-off criterion of 1 GeV/c on the transverse momentum and 0.5 GeV on the transverse energy in the calorimeter cells. The muons can be identified by the arrows that indicate the reconstructed tracks in the muon chambers. After the cut-off criteria are applied, only the muons from the Z^0 decay remain.

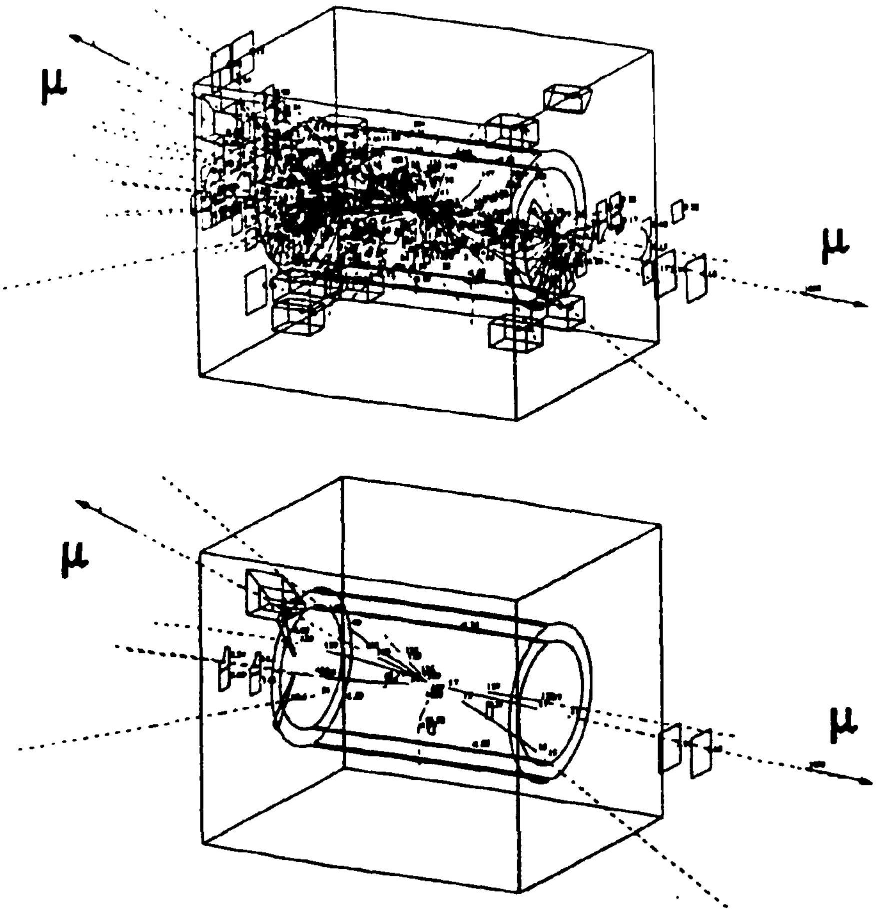

Fig. 6.3: An Active Z^0 Event

The figure shows a perspective view of the event; the upper diagram does so without any cut-off criteria for either the energy or the momentum of the particles, the lower figure shows the same event with a cut-off criterion of 1 GeV/c on the transverse momentum and 1.0 GeV on the transverse energy in the calorimeter cells. The muons can be identified by the arrows that indicate the reconstructed tracks in the muon chambers. Even after applying the cut-off criteria several high-energy tracks, other than the muons, remain; these belong to jets.

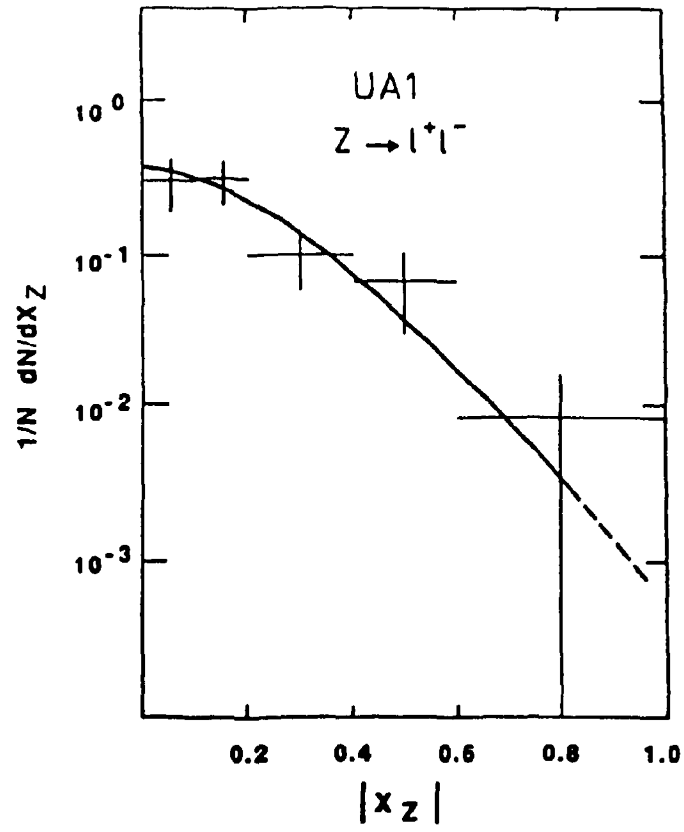

Fig. 6.4: Longitudinal Momentum Distribution for the Z^0

21 events stem from the electron channel, 12 from the muon channel. The data have been corrected for acceptance losses and detector resolution. It includes only lepton pairs for which the charges of both leptons could be well determined. Furthermore, only Z^0's with transverse momenta of less than 15 GeV/c were admitted. The solid curve represents the prediction of the ISAJET computer code; this curve has been normalized to the number of events.

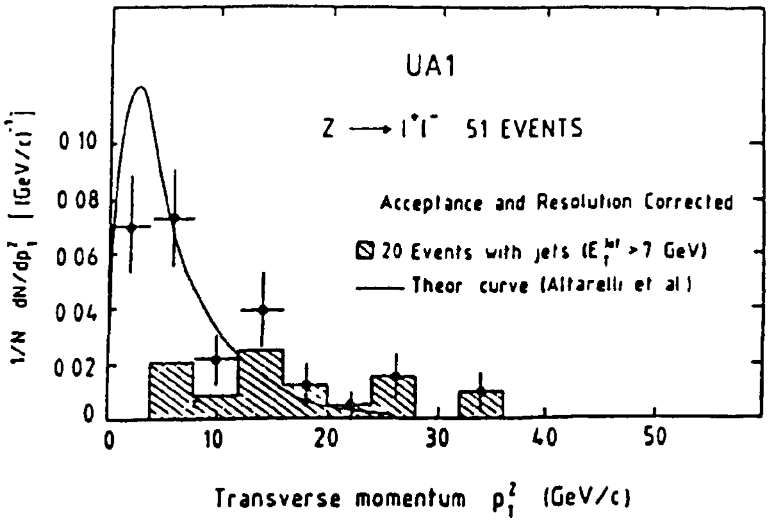

Fig. 6.5: The transverse Momentum Spectrum of the Z^0's

32 events stem from the electron channel, and 19 events from the muon channel. The radiative candidates are excluded. The theoretical prediction stems from Altarelli [87]; it has been normalized to 51 events. The shaded area designates those events in which a jet was found. The definition of a jet is explained in the text.

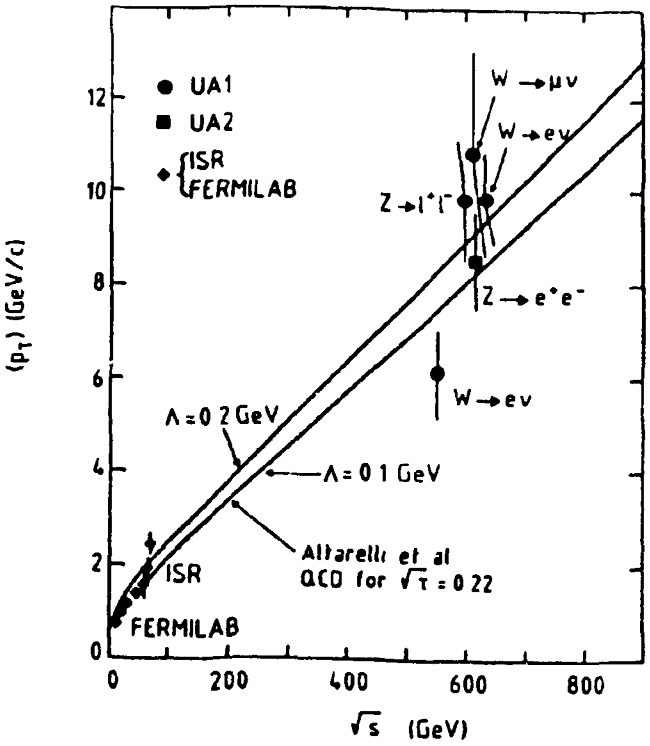

Fig. 6.6: Mean Transverse Momenta of Drell-Yan Lepton Pairs

The prediction by Altarelli is shown for two different values of λ_{QCD} for $\sqrt{\tau} = (M^2(l^+l^-)/S)^{1/2} = 0.22$. The value for $Z^0 \rightarrow l^+l^-$ has been averaged over both center-of-mass energies and over the electron channel and the muon channel. For comparison we also show data from ISR and from Fermilab. The goodness of the theoretical model by Altarelli [35, 87] can be seen.

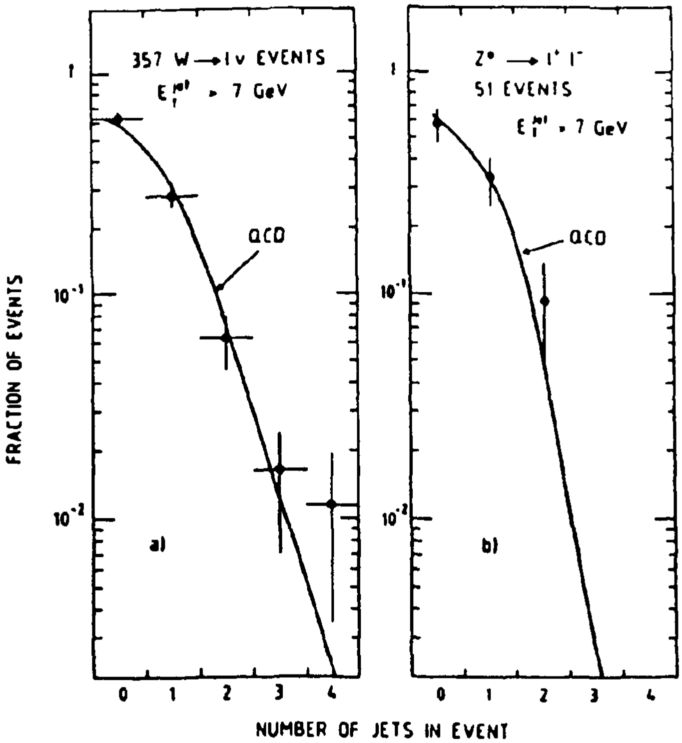

Fig. 6.7: Multiplicity Distribution of the Jets

These figures are based on 357 W events and 51 Z^0 events. The theoretical curve represents the ISAJET prediction. Both prediction and data have been normalized to the same number of events. The ISAJET data have been corrected for acceptance and resolution.

Ⓐ W- und Z^0- Sample

Ⓑ Experiment	$\sqrt{S}$ (GeV)	Ⓒ Reaktion	Ⓓ Luminosität (nb^{-1})	Ⓔ Ereignisse	Ⓕ Untergrund	Akzeptanz Ⓖ (%)
UA1	546	$Z^0 \to e^+e^-$	136	4	≤ 0.1	69 ± 3
UA2	546	$Z^0 \to e^+e^-$	142	9	0.2	53.5 ± 2.5
UA1	546	$Z^0 \to \mu^+\mu^-$	108	4	0.07	37 ± 5
UA1	630	$Z^0 \to e^+e^-$	568	29	0.2	69 ± 2
UA2	630	$Z^0 \to e^+e^-$	768	30	1.1	51.7 ± 2.5
UA1	630	$Z^0 \to \mu^+\mu^-$	555	15	0.35	40.1 ± 2.8
UA1	546	$W \to e\bar{\nu}_e$	136	59	6.8	69 ± 3
UA2	546	$W \to e\bar{\nu}_e$	142	42	4.1	44 ± 4
UA1	546	$W \to \mu\bar{\nu}_\mu$	108	10	0.7	16 ± 2
UA1	630	$W \to e\bar{\nu}_e$	568	240	19.3	61 ± 2
UA2	630	$W \to e\bar{\nu}_e$	738	206	21.4	44 ± 4
UA1	630	$W \to \mu\bar{\nu}_\mu$	551	57	3.3	15 ± 1
UA1	546, 630	$W \to \tau\bar{\nu}_\tau$	686	32	2.7	6.8 ± 0.5

A: W and Z^0 Sample

B. Experiment

C: Reaction

D: Luminosity (nb^{-1})

E: Events

F: Background

G: Acceptance (%)

Table 6.1: Parameters of the W and Z^0 Samples

The error in the luminosity is 15% in the UA1, while for the UA2 it is only 8%. In the tau channel of the W, only the values averaged over both energies are shown.

Ⓐ Partielle Produktionwirkungsquerschnitte

Experiment Ⓑ	Reaktion Ⓒ	$\sqrt{S} = 546\ GeV$ $\sigma \cdot B$ (pb)	$\sqrt{S} = 630\ GeV$ $\sigma \cdot B$ (pb)	$(\sigma \cdot B)^{(630)}/(\sigma \cdot B)^{(546)}$
UA1	$Z^0 \rightarrow \mu^+\mu^-$	$98^{+78}_{-44} \pm 20$	$66 \pm 17 \pm 11$	0.7 ± 0.4
UA1	$Z^0 \rightarrow e^+e^-$	$41^{+33}_{-20} \pm 6$	$74 \pm 14 \pm 11$	1.8 ± 0.9
UA2	$Z^0 \rightarrow e^+e^-$	$116 \pm 39 \pm 11$	$73 \pm 14 \pm 7$	0.6 ± 0.3
Theorie Ⓓ	$Z^0 \rightarrow l^+l^-$	44^{+14}_{-8}	53^{+17}_{-11}	1.25
UA1	$W \rightarrow \mu\bar{\nu}_\mu$	$560 \pm 180 \pm 120$	$630 \pm 80 \pm 110$	1.18 ± 0.40
UA1	$W \rightarrow e\bar{\nu}_e$	$550 \pm 60 \pm 90$	$630 \pm 50 \pm 100$	1.15 ± 0.19
UA2	$W \rightarrow e\bar{\nu}_e$	$610 \pm 100 \pm 70$	$570 \pm 40 \pm 70$	0.95 ± 0.18
UA1	$W \rightarrow \tau\bar{\nu}_\tau$	$610 \pm 130 \pm 120$		
Theorie Ⓓ	$W \rightarrow l\bar{\nu}_l$	460^{+150}_{-70}	590^{+160}_{-80}	1.23

A.	Partial production Cross Sections	D	Theory
B:	Experiment		Theory
C.	Reaction		

Table 6.2: Partial Production Cross Sections

The first error is the statistical one, the second, the systematic one. The theoretical predictions stem from Altarelli et al. [87]. It was assumed that no background due to the top quark was present in the W sample ($M_{Top} > 80$ GeV/c^2).

Chapter 7

Tests of the Standard Model

7.1 The Determination of the Z^o Mass

The invariant mass of the Z^O is reconstructed from the two four-vectors of the measured decay muons. The direction of the emitted muons can be measured in the central detector with practically arbitrary precision. However the momentum of the muons is only imprecisely determined there. Since the muons carry a momentum of about 30 - 80 GeV/c, they are only slightly deflected by the magnetic field. In determining the radius of curvature of the track, which is proportional to the inverse of the momentum, the systematic uncertainties of the measured track points dominate in the central detector, so that for a momentum of about 40 GeV an error of 100% is reached. Such uncertainties are, for example, imprecisely known displacement in the transition from one module to another, or even from one drift volume to another. Furthermore, individual drift volumes exhibited difficulties in their read-out electronics. When the error in 1/p becomes greater than the value of 1/p even the charge determination of the muons becomes uncertain.

An additional difficulty arises from the geometric arrangement of the detector in the magnetic field. In the central area, in the side regions, the tracks make small angles with respect to the field; they are therefore bent only to a small degree. Just in this region, unfortunately, the mean track length and the number of points along a track are also the least. The more the muons point forward, the more exact will be the momentum measurement in the central detector. Unfortunately, however, the muon detector has gaps at the boundary of the front region and very far forward.

We searched for an improved momentum measurement technique in order to be able to determine the mass of the Z^0 with the smallest possible error. It is in fact possible to determine the momentum of a high-energy muon even outside the central detector, if one uses the long lever arm which is represented by the muon chambers with their very precise position measurements, to determine the deflection in the magnetic field. [60]. This method of combined momentum fits (OMF - overall momentum fit) has already been presented in connection with the description of the track reconstruction process. An additional improvement in the mass determination can be achieved if one assumes that there is no neutrino in the Z^0 event. Then it is possible to use an energy balance from the calorimeter to obtain additional information about the transverse momentum of the Z^0, which can then, in turn, be used to improve the muon momenta. The method has already been presented in connection with the determination of the momentum of the Z^0. Of course now we must not carry out the energy balance with the boundary condition of a fixed value of the mass of the Z^0; this value must now be the end result of a fit as a parameter. In doing the momentum determination of the Z^0 from the calorimetry we had fixed the mass of the Z^0 in order to correct the muon momenta as well as the calorimeter measurements. Now we assume that we measure the transverse momentum of the Z^0 correctly within the errors by calorimetry, and use it to optimize the muon momenta without a prior fixing of the mass of the Z^0.

It must be noted that the measurement of the energy sum is also burdened with a error. Hence the method of energy balance presented above is also always a fitting procedure, aimed at minimizing a χ^2. It functions best when the muons in the transverse plane are as close as possible to being mutually perpendicular and if the vector sum of missing energy is not too large. If the muons in the transverse plane form an angle close to 180°, and if the missing energy vector is perpendicular to both of them (a so-called T configuration), the procedure converges very poorly, since the muons end up with enormously high momenta. The reconstructed mass is the almost infinite. Of course the procedure also delivers a wrong result if a part of the event escapes through one of the gaps in the calorimeters.

7.1.1 The Mass Fit

In the mass fit [114] the methods of momentum measurement described above are combined into a single procedure. In this process every event is tested to see the degree to which the methods of the combined momentum fit and the energy balance are applicable. Special treatment is needed for events in which the second muon did not enter the muon chambers; the standard UA1 computer programs are not prepared to deal with such configurations.

The mass is determined by a likelihood method [115]. It is calculated from the muon momenta to be:

$$M_{Z^\bullet} = \sqrt{2 \cdot p_1^{\mu} \cdot p_2^{\mu} \;, \cdot (1 - \cos\theta_{\mu\mu})} \tag{7.1}$$

where $\theta_{\mu\mu}$ is the angle enclosed by the muons. Since only the reciprocal momenta have Gaussian errors, we fit the inverse square of the mass:

$$R = 1/M^2 = r_1 \cdot r_2 \cdot K \tag{7.2}$$

where the constant $K = 1/[2 \cdot (1 - \cos \theta_{\mu\mu})]$ can be measured as accurately as desired in the central detector. Each individual measurement is assigned a weight w_1,calculated from the errors of the measured momenta. We have found that the best description of the momentum errors in the central detector is derived from the systematic error and the statistical error as follows:

$$\sigma_{tot} = \sqrt{\sigma_{syst} + 0.83\ \sigma_{stat}} \tag{7.3}$$

The resolution function with which the averaged mass is obtained from the i measurements is therefore:

$$f(M|R_i) \sim e^{-\frac{1}{2} w_i (R_i - R(M))^2} \tag{7.4}$$

where M is the weighted average of our measurements. This function is now folded with a Breit-Wigner function, since the true mass is not sharply defined, but rather has the shape of a resonance of width Γ about the central value M_0:

$$B(M_0|M) \sim \frac{M_0 \cdot M}{(M_0^2 \cdot M^2)^2 + M_0^2 \cdot \Gamma^2} \tag{7.5}$$

We must now test to see with which Breit-Wigner curve for a given mass M_0 our measured probability function is compatible with the greatest probability. For this reason we define a likelihood function which will then be minimized. It reads as follows:

$$
\begin{aligned}
\mathcal{L} &= \prod_i \int B(M_0|M) f(M|R_i) dM \\
&= \prod_i \int \frac{M_0 \cdot M_i}{(M_0^2 - M_i^2)^2 + M_0^2\Gamma^2} \, e^{-\frac{1}{2} w_i (R_i - \frac{1}{M_i})^2} \cdot dM
\end{aligned}
\tag{7.6}
$$

Table 7.1 lists all the masses, with and without energy balance. The mass fit will now first be done without the energy balance. In order to achieve better convergence, the event with the lowest mass (12039,1267), at 53 GeV/c^2, is excluded by means of a cut-off criterion in the Z^0 mass at 60 GeV/c^2. The events with masses above 160 GeV/c^2 have low weights because of their large errors. The effect of the mass cut-off is corrected in a correction which is performed subsequently. The masses in the radiative events (6636,509) and (18517,1469)) are computed from three decay particles. The calculated total error in the mass has different behavior in these instances than for two-body decay; therefore we excluded these two events from our fit.

Without applying the energy balance we find the following result from the minimization of the likelihood function (Figure 7.1):

$$
M_0^{fit} = 94.7^{+[illegible]}_{-[illegible]} \, \mathrm{GeV}/c^2 \tag{7.7}
$$

Fig. 7.2 shows the spectrum of the masses obtained in this manner. The plot contains 15 events that exhibit masses between 60 and 160 GeV/c^2. The three events with still higher masses have associated errors of more than 50 GeV/c^2, and therefore exert almost no weight in the fit.

If one attempts to apply the energy balance, four events are noted in which particles escaped through gaps in the detector, or that a light-pipe was hit, which falsifies the energy measurement.[8] In addition, the event (15621,138) was rejected because in this event the muon charges could not be determined with certainty; because of a convergence problem in the fit, this event yields a non-sensical mass of 277 ± 518 GeV/c^2 without the energy balance. In these cases we used the mass values without the energy balance in the fit, instead of the surely erroneous values based on energy balance. For consistency, we also excluded again those events with one high-energy photon.

Once the muon momenta had been corrected wherever possible by using the energy balance, the likelihood function is again minimized. For the raw mass, based on 18 events, the result was:

$$M_0^{Eb} = 93.1^{+5.2}_{-4.8}\,\mathrm{GeV}/c^2 \qquad (7.8)$$

The mass spectrum for the 14 events in which energy balance was used is shown in Fig. 7.3.

7.1.2 Corrections to the Mass Fit

The effect of the mass cut-off on the fit was examined using a Monte Carlo simulation. Z^0 events were generated in the ISAJET computer code, and then a complete detector simulation was performed. It is found that according to the simulation the value obtained using the mass fit, with and without energy balance, deviates systematically from the initial value in ISAJET. A more detailed study shows that this shift is due only to a simulation problem that does not exist in the real data [117]. In the present study the systematic mass determination error as determined by impulse measurement of muons is about 3%.

---

[8] (6600,222), (12530,937), (16039,474), and (17027,255).

We arrive at a real correction when we investigate the effect of the mass cut-offs with these Monte Carlo data. The mass without energy balance must be displaced by -0.6 ± 0.4 GeV/c^2; with the energy balance a correction of -0.9 ± 0.2 GeV/c^2 results.

An additional correction was able to be determined using the ISAJET Monte Carlo events and the complete detector simulation, a correction that becomes necessary when the energy balance is used. Because of energy fluctuations in the underlying event and systematic effects in the energy reconstruction in the calorimeter we find that applying the energy balance results in a systematic displacement of the reconstructed Z^0 mass of -1.4 ± 0.5 GeV/c^2; this correction was also made. This correction has essentially the following cause: There is no such thing as a negative missing energy; statistical fluctuations always lead to a finite energy vector in a chance direction.

7.1.3 The Result of the Mass Calculation

The measurement error cited so far is of purely statistical nature. The systematic error in the mass measurements has two significant sources, one systematic error in the momentum measurement, and one systematic error in the energy scale. From Monte Carlo studies and the W analysis [116] we estimate the systematic error of our measurements to be 2.8 GeV/c^2 without energy balance and 3.2 GeV/c^2 with energy balance [114]. Finally after applying all the corrections we find

$$M_{Z^0} = 94.1^{+8.1}_{-6.4}\,(stat.) \pm 2.8\,(syst.)\ \mathrm{GeV}/c^2 \quad \text{(without energy balance)} \tag{7.9}$$

$$M_{Z^0} = 90.7^{+5.2}_{-4.8}\,(stat.) \pm 3.2\,(syst.)\ \mathrm{GeV}/c^2 \quad \text{(with energy balance)} \tag{7.10}$$

By means of the energy balance procedure all information available from our apparatus concerning the Z^0 is optimally utilized. Therefore we prefer 90.7 GeV/c^2 for our final mass value. Table 7.2 also lists, for comparison, the Z^0 masses as determined in the electron channel by UA1 and UA2. The results there lie a little higher, but within the limits of error all the results fit together excellently.

Fig. 7.4, finally, is a logarithmic plot of the mass spectrum of 2-muon events with isolated muons with unequal charge. The resonance peak at the Z^0 mass is clearly visible, as well as the distance to the start of the continuum of Drell-Yan events, above which at low masses the peaks of the J/ Ψ and the Υ meson clearly jut out.

7.2 The Determination of Sin^2 $_W$ from the W and Z Masses

Once the masses of the intermediate vector bosons are known, we are in a position to determine two fundamental parameters of the standard model, namely the weak mixing angle, expressed as $\sin^2 \theta_W$ and the parameter ρ with which the isospin of the Higgs sector is fixed. In UA1 and UA2 the W and Z masses were measured in various decay channels; they are summarized in Table 7.2. Good agreement is observed, both between decay channels and between the experiments.

If one bases the calculations on the lowest-order diagrams, the standard model makes the following prediction about the mass of the W:

$$M_W = \frac{A_0}{\sin\theta_W} \tag{7.11}$$

$$A_0 = \sqrt{\frac{\pi\alpha}{G_F\sqrt{2}}} \tag{7.12}$$

$$= 37.2810 \pm 0.0003\,\mathrm{GeV}/c^2 \quad , \tag{7.13}$$

where α is the fine structure constant and G_F is the Fermi coupling constant. From a number of neutrino scattering experiments at low energy an average value for the electroweak mixing angle has already been derived [30]:

$$\sin^2\overline{\theta_W} = 0.233 \pm 0.003_{(exp)} \pm 0.005_{(theor)} \tag{7.14}$$

With this value we find for the mass of the W particle $M_W = 77.2$ GeV/c^2 . It is clear that the measured value of the mass of the W, at about 82 GeV/c^2 lies distinctly higher than the value given by this Born approximation. We must therefore correct the simplest order calculation by applying radiative corrections, which are summarized by the parameter Δ r. The result is:

$$A = \frac{A_0}{\sqrt{1-\Delta r}} \tag{7.15}$$

$$\sin^2\hat{\theta}_W = \frac{A^2}{M_W^2} \tag{7.16}$$

$$= \frac{A_0^2}{M_W^2}\frac{1}{1-\Delta r} \tag{7.17}$$

These radiative corrections are the subject of extensive theoretical investigations [118, 119, 120]. They are, for all practical purposes, insensitive to the mass of the Higgs boson over a range up to 1000 GeV/c^2 . In contrast, there is a strong dependence on the mass of the top quark; at m_{Top} = 270 GeV/c^2 Δr becomes equal to 0 (see Fig. 7.5). For Z masses between 91 and 95 GeV/c^2 Δr varies by about 5%. We assume that m_{Top} = 35 GeV/c^2, m_H = 100 GeV/c^2 and M_Z = 93.5 GeV/c^2. Then the theory yields

$$\Delta r = 0.0711 \pm 0.0013 \tag{7.18}$$

With this fixed value of Δr and the mass of the W as measured by us, we find the following results for the weak mixing angle:

$$\sin^2\theta_W = 0.22 \quad \text{(UA1 averaged)} \tag{7.19}$$

We are also in a position to determine the mixing angle from the ratio of the W and Z masses, if we assume that we have $\rho = 1$:

$$M_Z = \frac{M_W}{\sqrt{\rho}\cos\theta_W} \tag{7.20}$$

$$\sin^2\theta_W = 1 - \frac{M_W^2}{M_Z^2} \tag{7.21}$$

This method has the advantage of being independent of systematic errors, such as, for example, the energy calibration of the detector; it is, however, less accurate than the first method, even though it is able to do without a theoretical model of the radiative corrections. In the UA1 we obtain:

$$\sin^2 \bar{\theta}_W = 0.211 \pm 0.025 \quad \text{(Elektronkanal)} \tag{7.22}$$

$$187 \pm 0.025 \quad \text{(Myonkanal)} \tag{7.23}$$

Table 7.3 summarizes the results. It will be observed that both methods give results that are consistent with the value derived from neutrino scattering experiments at relatively low Q^2.

7.3 Determining the Radiative Corrections

With both of the definitions of the weak mixing angle presented above we can, on the other hand, determine the magnitude of the radiative corrections experimentally, by using, on the one hand, the mixing angle from the neutrino experiments and, on the other, the mixing angle from the W and Z measurements:

$$\Delta r_1 = 1 - \frac{A_0^2}{M_W^2} \frac{1}{\sin^2 \theta_W} \tag{7.24}$$

$$\Delta r_2 = 1 - \frac{A_0^2}{M_W^2} \frac{1}{\sin^2 \bar{\theta}_W} \tag{7.25}$$

In the electron channel we obtain:

$$\mathrm{UA1}: \quad \Delta r_1 = 0.038 \pm 0.100\,(\mathrm{stat.}) \pm 0.076\,(\mathrm{syst.}), \tag{7.26}$$

$$\mathrm{UA1}: \quad \Delta r_2 = 0.125 \pm 0.021\,(\mathrm{stat.}) \pm 0.057\,(\mathrm{syst.}). \tag{7.27}$$

$$\mathrm{UA2}: \quad \Delta r_1 = 0.068 \pm 0.087\,(\mathrm{stat.}) \pm 0.030\,(\mathrm{syst.}), \tag{7.28}$$

$$\mathrm{UA2}: \quad \Delta r_2 = 0.068 \pm 0.022\,(\mathrm{stat.}) \pm 0.032\,(\mathrm{syst.}). \tag{7.29}$$

Unfortunately these measurements are quite insensitive, but it is possible to say that positive values are preferred. This leads to two conclusions:

- First, radiative corrections seem to be necessary.
- Second, We can state a weak limit on the mass of the top quark: $m_{\mathrm{Top}} \leq 250$ GeV/c^2 for a Higgs mass range up to 1 TeV/c^2.

The mass determinations may be utilized for a consistency test of the standard model, if one plots the mass difference between the W and the Z against the mass of the Z. For the mass difference we find:

$$\mathrm{UA1}: \quad (M_Z - M_W)_e = 10.4 \pm 1.4\,(\mathrm{stat.}) \pm 0.8\,(\mathrm{syst.})\ \mathrm{GeV}/c^2 \tag{7.30}$$

$$\mathrm{UA1}: \quad (M_Z - M_W)_\mu = 8.7^{+7.4}_{-7.7}\,(\mathrm{stat.}) \pm 1.9\,(\mathrm{syst.})\ \mathrm{GeV}/c^2 \tag{7.31}$$

The results are summarized in Fig. 7.6, where the uncertainties in the mass determinations of the W and the Z are plotted in the $[M_Z - M_W, M_Z]$ plane. Both experiments are in accord with the prediction of the standard model. A sensitivity to radiative corrections is difficult to recognize, nevertheless, the UA2 measurement seems to prefer the solution containing the radiative corrections. Unfortunately, due to the large errors, the measurement in the muon channel is very insensitive.

7.4 The Determination of Sin^2 θ_W From the Asymmetry

In deep inelastic scattering processes an asymmetry in the polar angle distribution (for definition see Fig. 7.7) in the center-of-mass coordinate system is always observed when one succeeds in determining the polarization of the incoming particles. The polarization is an axial vector; in contrast, the momenta of the particles are vectors. The two quantities transform differently under spatial mirror inversion; whereas the vector flips its sign, the polar vector maintains its direction. Because of their V-A character weak interactions with charged currents act exactly like a projection operator of the polarization $1/2(1 \pm \gamma^5)$. The coupling constants g_A and g_V are both equal to 1/2, both for the coupling to the leptons and for the coupling to the quarks; maximum parity violation occurs in the production and decay of the W boson, the carrier of the charged current. Charged currents couple only to left-handed fermions.

If one considers neutral currents, this maximum parity violation is reduced, since now a coupling to right-handed fermions is allowed. The angular distribution in the center-of-mass system is generally calculated to be:

$$\frac{d\sigma}{d\cos\theta^*} = \frac{3}{8}\cdot\Big(1+\cos\theta^{*2} - \frac{8 g_V^q g_A^q g_V^l g_A^l}{((g_V^q)^2+(g_A^q)^2)\cdot((g_V^l)^2+(g_A^l)^2)}\cos\theta^*\Big) \qquad (7.32)$$

In calculating this angular distribution one must average according to the u and d quark distributions in the protons and antiprotons in the $u\bar{u}$ and $d\bar{d}$ annihilations. It is to be noted that an asymmetry with respect to $\theta^* = \pi/2$ occurs only if all the coupling constants $g_A{}^q$, $g_V{}^q$, $g_A{}^l$, and $g_V{}^l$ are simultaneously different from zero. However, the weak mixing angle $\sin^2\theta_W$ also enters in the coupling to neutral currents. For a fermion with charge Q_f and the third component of the weak isospin T_3 we have (see also Table 2.2 and Table 2.1):

$$g_V^f = T_{3L}^f + T_{3R}^f - 2\sin^2\theta_W Q_f \tag{7.33}$$

$${}^f = T_{3L}^f - T_{3R}^f \tag{7.34}$$

In particular for charged leptons we have:

$$g_V^l = -\frac{1}{2} + 2\sin^2\theta_W \tag{7.35}$$

That is to say, when $\sin^2\theta_W = 0.25$, the linear component of the distribution in $\cos\theta^*$, which provides the asymmetry, is completely suppressed, since then the g_V of the outgoing leptons from the decay of the Z^0 disappears. In general the asymmetry is defined by counting up the leptons in the front and rear hemispheres.

$$A = \frac{N^+ - N^-}{N^+ + N^-} \tag{7.36}$$

Fig. 7.8 shows the measured angular distribution of the outgoing positively charged leptons from our measured Z^o decays. In the distribution electron and muon decays of the Z^o's at both the center-of-mass energies are all added together in order to achieve the largest possible sample. 21 electron events and 12 muon events are included in the plot, since the following cut-off criteria were applied:[9]

- The radiative Z^o candidates were excluded.

- The charge of the leptons must be unambiguosly determined ($(1/p) > 2\sigma(1/p)$).

- The transverse momentum of the Z^o must be less than 15 GeV/c in order to reduce the error caused by pure Drell-Yan production via gluon bremsstrahlung.

- Because of the large momentum uncertainty in the case of the muons, only those muon events were admitted for which, with the aid of the energy balance and a forced mass of the Z^o of 90.7 GeV/c^2, it was possible to improve the momentum measurement (see the chapter on production properties).

- Before the two classes of events were combined, we corrected the distributions for acceptance losses. This correction depends on the transverse momentum of the Z^o, and is slightly different for electrons and muons (again, see also the chapter on the production properties).

---

[9] These cut-off criteria are the same as those applied in the determination of the longitudinal momentum of the Z^o.

A Monte Carlo study gives the result that in calculating the theoretical angular distribution according to the standard model, different structure functions, which require averaging over the quarks, have only a minor influence. From our data we obtain an asymmetry of

$$A = +0.045 \pm 0.18 \tag{7.37}$$

From this we fit a value for the weak mixing angle of:

$$\sin^2 \theta_W = 0.24^{+0.05}_{-0.04} \tag{7.38}$$

With this method we are thus in a position to determine the weak mixing angle without a knowledge of the W and Z masses; we have found an additional independent method. However, we must admit that, due to the small asymmetry a very much larger number of Z^0 events is required to reduce the statistical error in the measurement, and thereby make this method competitive for determining $\sin^2 \theta_W$ from the mass values.

At PETRA energies, in e^+e^- annihilation at center-of-mass energies far below the Z^0 mass, the measurement of the asymmetry, which is obtained from the interference of the photon exchange and the Z^0 exchange, is an important method for measuring the weak mixing angle [121]. There a value of $\sin^2 \theta_W = 0.205 \pm 0.018 \pm 0.013$ was found for $M_Z = 91.9 \pm 1.8$ GeV/c^2.

7.5 A Test of the Lepton Universality

The measurements of the partial production cross sections ($\sigma \cdot B$) for the various decay channels of the intermediate vector bosons offer the possibility for testing the lepton universality for transferred four-momenta $Q^2 = M_W{}^2$ and $Q^2 = M_Z{}^2$. For the muonic decay one has:

$$(\sigma \cdot B) = \sigma_Z \cdot B(Z^0 \to \mu^+\mu^-) \tag{7.39}$$

$$= \sigma_Z \frac{\Gamma(Z^0 \to \mu^+\mu^-)}{\Gamma_{tot}} , \tag{7.40}$$

where Γ_{tot} is the total width and $\Gamma(Z^0 \to \mu^+\mu^-)$ is the muonic partial width. This partial width, in turn, is proportional to the square of the coupling constants:

$$\Gamma(Z^0 \to \mu^+\mu^-) \propto g_\mu^2 \tag{7.41}$$

The ratio of the coupling constants in two leptonic decay channels, in our case, the electronic and muonic channels, may thus be directly calculated form the partial production cross sections:

$$\left(\frac{g_\mu}{g_e}\right)^2 = \frac{\Gamma(Z^0 \to \mu^+\mu^-)}{\Gamma(Z^0 \to e^+e^-)} \tag{7.42}$$

$$= \frac{\sigma_Z \frac{\Gamma(Z^0 \to \mu^+\mu^-)}{\Gamma_{tot}}}{\sigma_Z \frac{\Gamma(Z^0 \to e^+e^-)}{\Gamma_{tot}}} \tag{7.43}$$

$$= \frac{(\sigma \cdot B)(Z^0 \rightarrow \mu^+\mu^-)}{(\sigma \cdot B)(Z^0 \rightarrow e^+e^-)} \tag{7.44}$$

We average within a single experiment weighted by the luminosity, which means that the averaging is done at an effective center-of-mass energy between 545 GeV and 630 GeV, although for all the data samples at different energies. It is important that we measure at the largest momentum transfers that have to date been achieved at particle accelerators: $Q^2 = M_{IVB}^2 \approx 7000$ GeV/c^2. In fixed-target experiments to date, only typical values Q^2 between 10 and 20 GeV/c^2 have been achieved [91]. The result we obtained at UA1 for the coupling to the neutral current was:

$$\frac{g_\mu^{neutral}}{g_e^{neutral}} = 1.02 \pm 0.15 \pm 0.04 \tag{7.45}$$

For the coupling to the weak charged current we also have available the measurements in the tau channel. The result is:

$$(g_\mu^{charged})/g_c^{charged}) = 1.00 \pm 0.07 \pm 0.04 \tag{7.46}$$

$$(g_\tau^{charged})/g_c^{charged}) = 1.01 \pm 0.10 \pm 0.06 \tag{7.47}$$

The first error shown is of statistical nature, the second is systematic. We see that, within the limitations of the precision of the experiment, the three leptons couple equally strongly to both the charged and the neutral electroweak current.

7.6 The Number of Neutrino Generations

The standard model of the electroweak interaction has nothing to say about how many lepton generations and how many quark generations there are. Currently we have experimental knowledge of three generations each, which were introduced in the chapter on theory. It is true, however, that the search is still on for the heaviest quark, the top quark. The lighter bottom quark as well as the tau lepton, which are both assigned to the same generation, have been found and closely examined. The standard model further assumes that there is a mass-less left-handed neutrino in each generation. We are therefore interested in the question of how many additional generations of quarks and leptons there are in addition to the three that are known.

Astronomical observations and cosmological calculations furnish an upper limit to the number of generations. Admittedly, the theoretical calculations are based on conceptions that are difficult to check experimentally. In the universe we observe an excess of light elements such as D, He^3, He^4, and Li^7, which must have come into being in an earlier stage of development of the universe. Their production rate, however, depends, among other factors, on the number of neutrino generations. In particular, a limit of $N_\nu \leq 7$ was derived from the excess of He^4 [102]. A correction to the measurement of the excess yielded $N_\nu \leq 5$ [103]. A more recent interpretation of the measurements, as well as more recent models and error calculations gave Ellis et al. a somewhat higher limit: $N_\nu \leq 5.5$ [104].

We have several possibilities for determining the number of neutrino generations at the proton-antiproton collider. We shall first describe a rather obvious, but inexact, method a) and then a cleverer procedure b), which does, however, depend on theoretical assumptions about the momentum distribution of the quarks in p^+p^- collisions.

About a): As we have seen, the Z^0 decays into a fermion-antifermion pair, thus also into a neutrino and the corresponding anti-neutrino. If there are three generations one obtains a total of $3 \cdot 6(q^+q^-) + 1 \cdot 6(l^+l^-) = 24$ decay channels that, each with their different partial widths, contribute to the total width of the Z^0 mass resonance. Thus we can draw conclusions about the number of decay channels from a measurement of the width of the Z^0 mass. If one further assumes that all additional, unknown, leptons and quarks are heavier than half the Z^0 mass, and hence do not open any additional decay channels, then it follows that the measurement of the Z^0 width results in an upper limit of the number of neutrino generations.

However, there is a difficulty in principle in carrying out this experiment: Our detector is not in capable to determine the mass arbitrarily well in an individual event, since the experimental resolution smears the natural line width of the Z^0. From the mass distribution shown in the muon channel (see the chapter "The Determination of the Z^0 Mass") it is clear that it is not possible there to "unsmear" the natural width of the Z^0 by using the resolution function. In the electron channels at the UA1 and the UA2 that process does succeed, even though the result, the natural line width, is burdened with a large uncertainty. The limits that are derived from these measurements are not very sharp. For the total number of neutrino generations the result is [105, 106]:

$$\text{UA1}: \quad \Gamma_{Z^0} = 2.3^{+3.3}_{-1.5}(\text{stat.})\ \text{GeV}/c^2 \tag{7.48}$$

$$< 8.3\ \text{GeV}/c^2\ (90\%\ \text{CL}) \tag{7.49}$$

This yields

$$N_\nu < 28 \ (90\% \ \mathrm{CL}) \qquad (7.50))$$

$$\mathrm{UA2:} \ \Gamma_{Z^0} = 2.7 \pm 1.0_{(\mathrm{syst.})} \pm 2.0_{(\mathrm{stat.})} \ \mathrm{GeV}/c^2 \tag{7.51}$$

$$< 5.6 \ \mathrm{GeV}/c^2 \ (90\% \ \mathrm{CL}) \tag{7.52}$$

which yields

$$N_\nu < 15 \ (90\% \ \mathrm{CL}) \tag{7.53}$$

Thus this procedure does nothing to tighten the limits set by astronomical observations.

About b): In a better procedure [108], one starts with the ratio of the cross sections for W and Z production, defined as follows:

$$R = \frac{\sigma_W \cdot B(W \to l\nu)}{\sigma_Z \cdot B(Z \to ll)} \tag{7.54}$$

$$= (\frac{\sigma_W}{\sigma_Z}) \cdot \frac{\Gamma(W \to l\nu)}{\Gamma(Z \to ll)} \cdot \frac{\Gamma_Z^{tot}(M_{Top}, N_\nu)}{\Gamma_W^{tot}(M_{Top})} \tag{7.55}$$

$$= R_{QCD} \cdot R_{ew}(M_{Top}, N_\nu) \tag{7.56}$$

The first term designates the ratio of cross sections in the production of the bosons, which takes place by the Drell-Yan process, with the addition of higher order terms that arise from the strong interaction. Thus this term can be calculated only with

QCD accuracy; among other requirements, it is necessary to chose suitable structure functions for quarks and gluons and to correct the Q^2 dependence of the processes correctly. The calculations yield the following results:

$$\left(\frac{\sigma_W}{\sigma_Z}\right) = 3.25 \pm 0.20 \quad [35, 87] \tag{7.57}$$

$$= 3.36 \pm 0.09 \quad [109] \tag{7.58}$$

$$= 3.41 \pm 0.08 \quad [110] \tag{7.59}$$

$$= 3.28 \pm 0.15 \quad [111] \tag{7.60}$$

This ratio is almost independent of the choice of center-of-mass energy.

The second term, R_{ew} may be calculated in the model of the electroweak theory, from which the partial widths of the leptonic decay channels follow. It is true, though, that the total widths of the W and Z exhibit different behaviors as function of the mass of the top quark. Aside from the known channels the W can also decay into a $t\bar{b}$ pair. Since the b is very light relative to the W, the W → $t\bar{b}$ decay is kinematically allowed for top masses up to almost the mass of the W. The Z, by contrast, can also decay, among other possibilities, into a $t\bar{t}$ pair. If the mass of the top quark lies higher than half the mass of the Z, this decay cannot occur. On the other hand, the decay of the W into a $t\bar{q}$ pair is possible almost up to the mass of the W, because of the low masses of the remaining quarks for the mass of the top quark. Thus the only other decay channels open to the Z are the neutrinos of generations not yet observed. R is therefore a function of the mass of the top quark and the number of neutrino generations.[10] If we set a lower limit to the mass of the top quark, then we can state a limit to the number of neutrino generations.

We have determined R, using a likelihood method, namely, by first having performed four individual measurements, namely in the electron channel and the muon channel for each of the two center-of-mass energies, and then having fitted all four measurements of R jointly:[11]

$$R_{exp} = f\left(\sum_i \frac{N(W \to l\nu)}{N(Z \to ll)}\right) \tag{7.61}$$

The averaged experimental value[12] of the measured ratio R amounts to $R_{exp} = 9.1_{-1.2}^{+1.7}$. Fig. 7.9 shows the likelihood function of the fit with the minimum at R = 9.1 from the UA1 data. The values from UA2 as well as the combination and the upward estimates with different confidence limits are shown in Table 7.4.

We now use a fitting procedure [108] to determine the maximum number of neutrino generations from the combined UA1 and UA2 data, making the following assumptions:

- The top quark is heavier than 44 GeV/c^2 [112].

- $R_{QCD} = 3.36$.

---

[10] A hypothetical heavy lepton would have the same influence as the top quark.

[11] Our statistical error still dominates over the uncertainties in the QCD calculation of R_{QCD}.

[12] The value should be reduced by 3%, if the top quark has a mass smaller than about 50 GeV/c^2, since in that event the W samples are contaminated by top-quark background.

- The number of neutrino generations is at least 3.

and find, with 90% confidence:

$$N_\nu \leq 5.7 \ (90\% \ CL) \tag{7.62}$$

Fig. 7.10 shows these limits; for a heavy top quark this conclusion would be even stronger, since in that case the contamination in the W sample would be lower. Since, however, aside from our own mass estimates [112], we have no knowledge about the top quark, we prefer the conservative value of 5.7.

7.7 The Determination of the ρ Parameter

A deviation from the minimal standard model presented here will cause a change in the formalism above. There will be a difference in the weak mixing angle, depending on which method of measurement is chosen. We emphasize once more that we do not find such deviations, but we can state limits on the degree to which deviations from the minimal model are possible; such deviations would manifest themselves as a value of the ρ parameter different from 1. We therefore define:

$$\rho = \frac{m_W^2}{m_Z^2} \frac{1}{\cos^2 \theta_W} \tag{7.63}$$

and obtain the values shown in Table 7.5. All are in good agreement with $\rho = 1$.

7.8 The Search for Heavy W's and Z's

An interesting question is whether heavier gauge bosons, W' and Z' might exist, which would also manifest themselves by their leptonic decay channels. If such heavier bosons did exist, the theory of the electroweak interactions would not be compatible with a minimal standard model. We assume that these heavy bosons would couple to the fermions exactly like the known W and Z, and that they would exhibit the same branching ratios as the known W and Z. Because of the larger number of events we limit ourselves to our data in the electron channel, and recognize:

Neither in the UA1 nor the UA2 were any events found in which the reconstructed mass significantly exceeds the mass of the vector bosons. From this null result we can derive a limit for $\sigma \cdot B$ of the heavy bosons [122]. We must, however, make several assumptions in order to do so:

- 1) For the heavy bosons the acceptance increases by about 5 to 7%, since on the average more energy will be deposited in the calorimeters.

- 2) The motion of the quarks is described by the structure functions of Duke and Owens (Set 1) [93] and Diemoz et al. [111]. Other parameterizations yield results that differ from these by up to 10%; however these differences will in part vanish again in the course of normalization to the existing data sample.

- 3) For the QCD scale we choose $Q = M_{W'}$ and $Q = M_{Z'}$.

- 4) In order to obtain the best possible statistics we add our data sets taken at the two different center-of-mass energies.

We obtain, with 90% confidence:

$$(\sigma \cdot B)_{W'} < 4.6 \text{ pb} \tag{7.64}$$

$$(\sigma \cdot B)_{Z'} < 4.5 \text{ pb} \tag{7.65}$$

Martinelli [123] calculated according to Altarelli [87] how the product of cross section times the branching ratio changes with the mass of the gauge bosons; the relationship is shown in Fig. 7.11. With this relationship the limits for the product $\sigma \cdot B$ can be used to set limits to the masses of the hypothetical heavy partners of W and Z, using the structure functions by Diemoz et al.:

$$M_{W'} > 220 \text{ GeV}/c^2 \text{ (90\% CL)} \tag{7.66}$$

$$M_{Z'} > 173 \text{ GeV}/c^2 \text{ (90\% CL)} \tag{7.67}$$

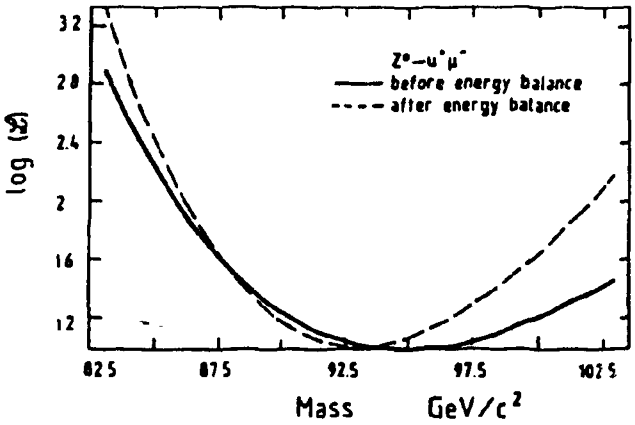

Fig. 7.1: Likelihood Function in the Mass Fit,
With and Without Energy Balance

The minima lie at 94.7 and 93.1 GeV/c^2 .

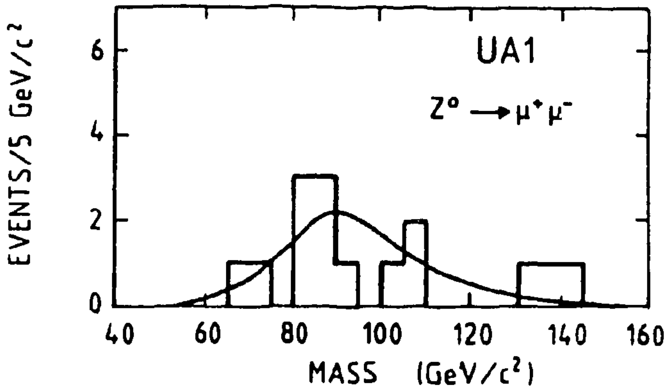

Fig. 7.2: Mass Distribution Without Applying the Energy Balance

18 events are included; events with a hard photon, as well as the event with 53 GeV/c^2 are excluded. The fitted curve represents the Breit-Wigner resonance at 94.1 GeV/c^2 folded with our resolution function. 3 events with large uncertainties lie above 160 GeV/c^2.

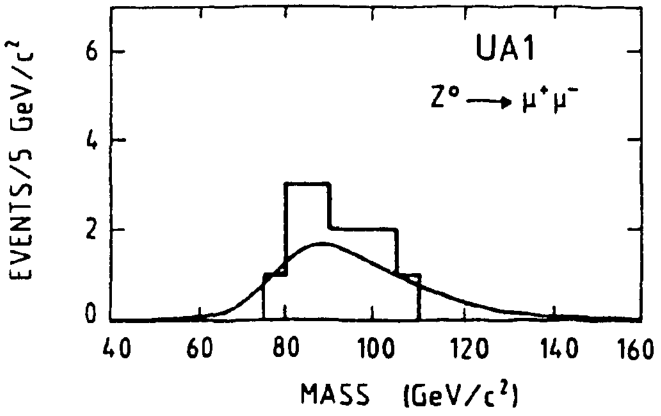

Fig. 7.3: Mass Distribution Using the Energy Balance

14 events are included in the plot.; 5 events with suspicious energy fluxes, as well as the events with a hard photon are excluded. The fitted curve represents the Breit-Wigner resonance at 90.7 GeV/c^2 folded with our resolution function.

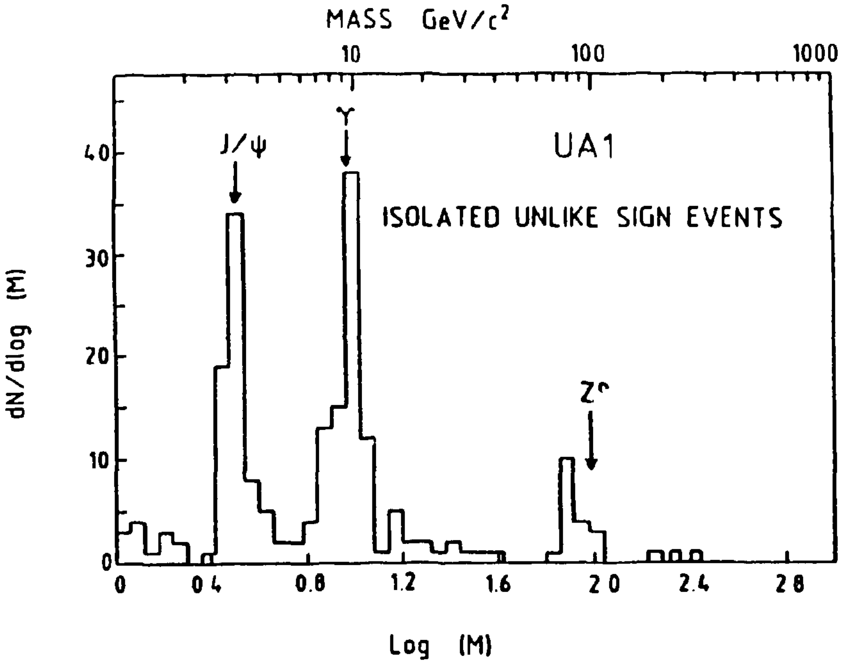

Fig. 7.4: Logarithmic Mass Spectrum for 2-Muon Events

Below 50 GeV/c^2 all masses were calculated from the central detector momenta. Above 50 GeV/c^2 the values are obtained with the combined momentum fit. Where possible, the energy balance was used in addition. The radiative Z^o's are included with the $\mu\mu_\nu$ mass; they were calculated using the energy balance. The events above 160 GeV/c^2 all have errors greater than 50 GeV/c^2. The events with masses M < 6 GeV/c^2, 6 GeV/c^2 < M < 50 GeV/c^2, and 50 GeV/c^2 < M were derived by applying different selection criteria. For this reason the relative frequencies of these mass regions are without significance.

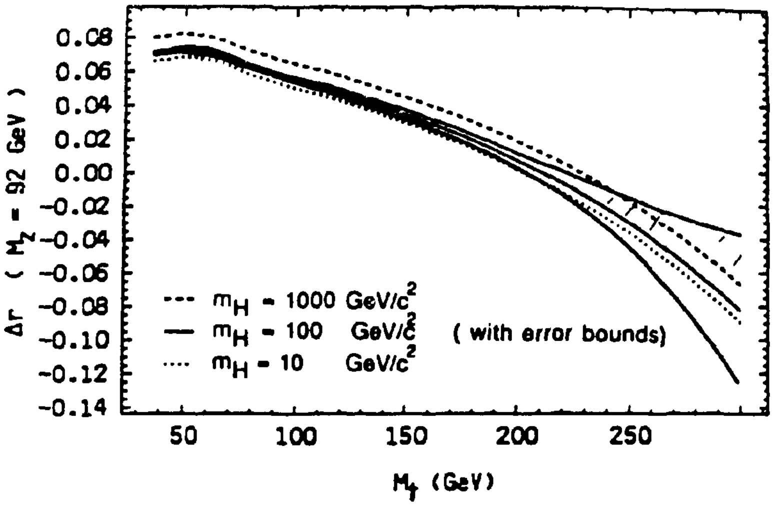

Fig. 7.5: Dependence of the Radiative Corrections on m_t and m_H (From [119, 116])

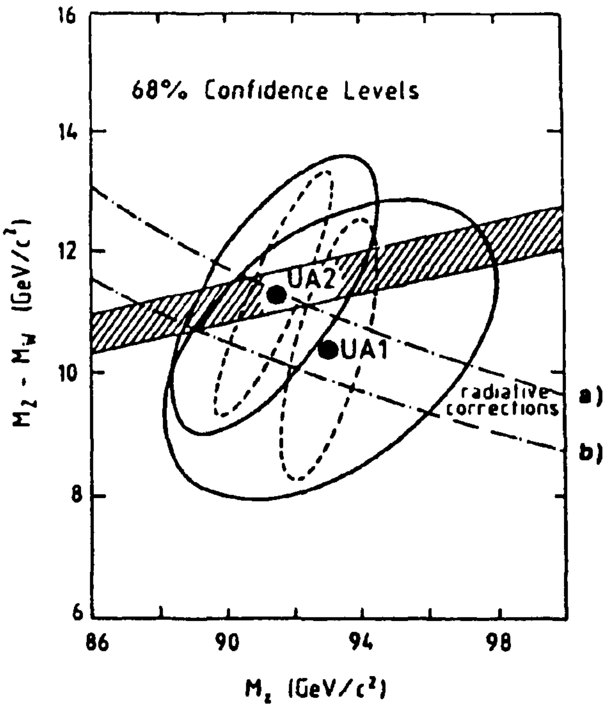

Fig. 7.6: Correlation of the W-Z Mass Difference and the Mass of the Z

Only the electron channel data from UA1 and UA2 are included in the plot. The elliptical curves show the 1 σ contours of the statistical errors as well as the quadratically summed statistical and systematic errors. The hatched band represents $\sin^2\theta_W = 0.232 \pm 0.005$. The curves a) and b) are the standard model predictions with and without radiative corrections for the mass difference as function of the mass of the Z.

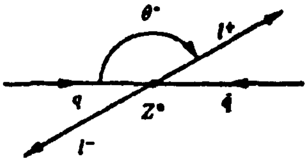

Fig. 7.7: For the Definition of the Polar Angle θ^* in the Center-of-Mass System

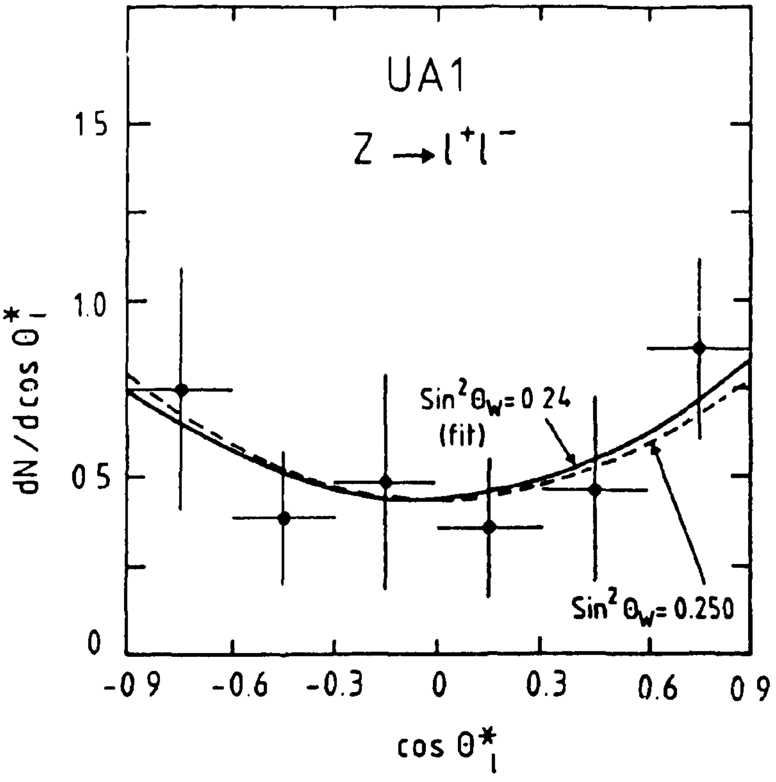

Fig. 7.8: Polar Angle Distribution of the Leptons in the Center-of-Mass System

θ^* is the angle between the out-going positively charged lepton and the out-going antiproton. 33 events are included in the plot. The transverse momentum of the Z^0 must be smaller than 15 GeV/c, and the charge of the leptons must be well measured. The cut-off criteria are the same as in the determination of the longitudinal momentum of the Z^0. The data points have been corrected for the acceptance. For comparison the expectations for a theoretical value of $\sin^2 \theta_W$ = 0.25 and our fitted value of $\sin^2 \theta_W$ = 0.24 are also plotted.

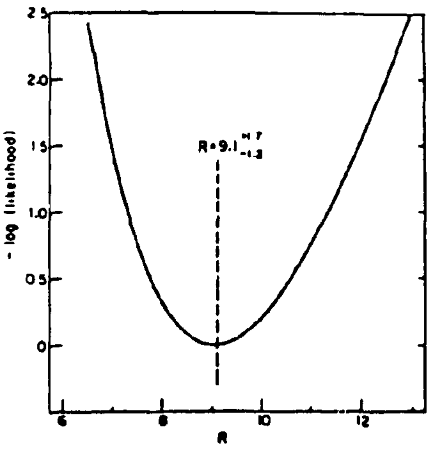

Fig. 7.9: Likelihood Function of the R-Determination in UA1

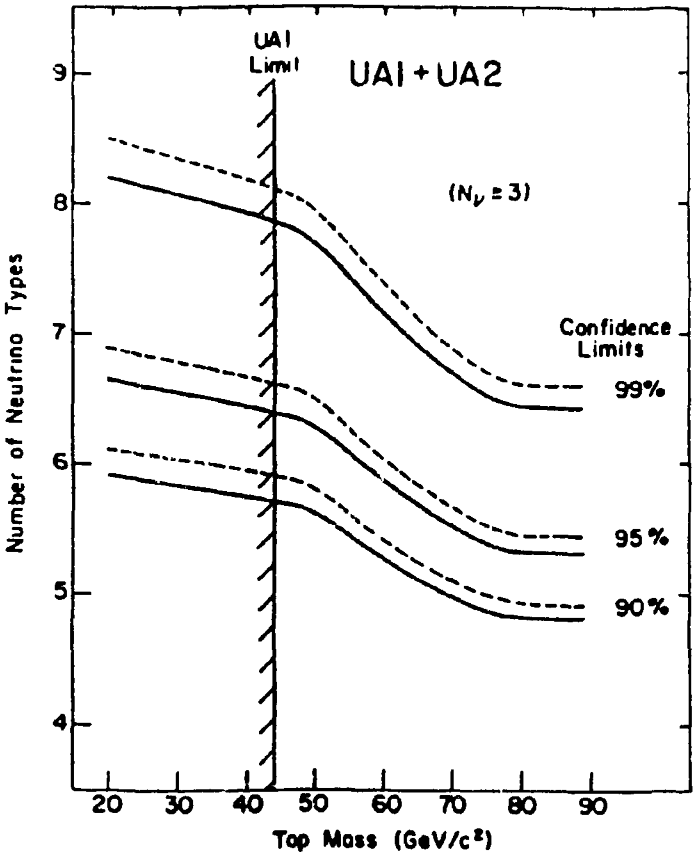

Fig. 7.10: Number of Neutrinos as Function of the Mass of the Top Quark

Limits on neutrino generations as function of the mass of the top quark and the confidence. Combined values from UA1 and UA2 are used, as well as an $R_{QCD} = 3.36$. The boundary conditions are $N_\nu \geq 3$ and $m_t \geq 44$ GeV/c^2. The solid lines were obtained from the predictions of R_{QCD} by Martin et al. [109] The dashed lines are obtained with an R_{QCD} from Halzen et al. [110].

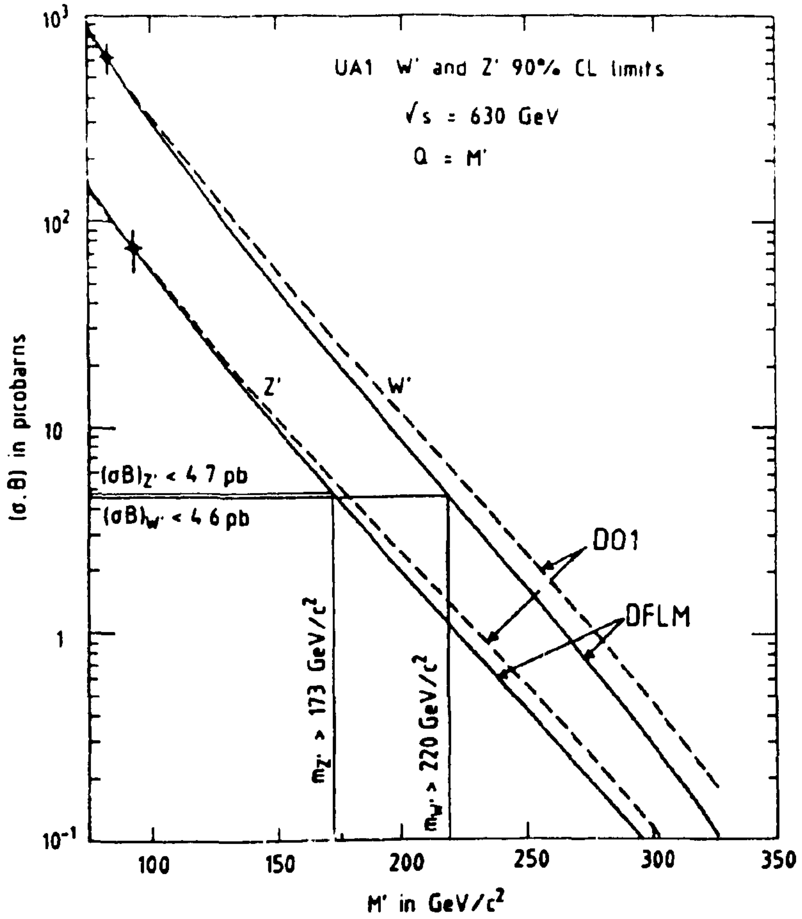

Fig. 7.11: Limits on Heavier W's and Z's

The calculated partial production cross sections for W and Z are shown, fitted with 90% confidence limit to the measured values from UA1 in the electron channel. The values for $\sqrt{S}$ = 546 GeV/c^2 are scaled to $\sqrt{S}$ = 630 GeV/c^2 on the basis of the theoretical expectation of Altarelli, and there added to the measurements. Structure functions by Duke and Owens (Set 1) [93] were assumed (dashed curve); alternatively assumed were λ = 0.2 GeV and Diemoz et al. [111] (solid curve).

Run	Ⓐ Ereignis	Masse ohne Energiebalance Ⓑ GeV/c^2	Masse mit Energiebalance Ⓒ GeV/c^2	Ⓓ Kommentar
6219	947	74 ± 20	89 ± 25	Ⓔ
6600	222	209 ± 336		Energie im Spalt
6636	509	66 ± 16	81 ± 15	$\mu\mu\gamma$
7428	1110	130 ± 215	104 ± 90	
8523	831	83 ± 31	83 ± 28	
9323	93	101 ± 49	87 ± 18	
10605	890	94 ± 35	81 ± 11	
11619	518	84 ± 15	89 ± 15	Ⓕ
12039	1267	53 ± 15	91 ± 14	mögl. $\tau^+\tau^-$-Kandidat
12287	30	106 ± 22	95 ± 11	Ⓔ
12530	937	142 ± 60		Energie im Spalt
15951	770	163 ± 70	109 ± 17	
15621	137	277 ± 518	Ⓖ	Fit-Konversion Problem
16039	474	85 ± 24	Ⓗ	Lichtleiter Problem
16201	30	135 ± 88	91 ± 14	
17027	255	85 ± 36	86 ± 36	
18046	99	87 ± 47	Ⓔ	Energie im Spalt
18451	851	67 ± 11	83 ± 11	
18517	1469	61 ± 53	94 ± 56	$\mu\mu\gamma$
18580	344	106 ± 26	103 ± 21	
19208	17	80 ± 24	76 ± 20	

A	Event
B:	Mass without Energy Balance
C.	Mass with Energy Balance
D.	Comments

E:	Energy in the gap Energy in the gap Energy in the gap
F:	Possible $\tau^+\tau^-$ candidate
G:	Fit conversion problem
H:	Light-pipe problem

Table 7.1: Masses of the Z^0 Events

The muon momenta were determined using the combined momentum fit. For the radiative events ($\mu\mu\gamma$), the mass value with energy balance corresponds to the $\mu\mu\gamma$ mass, while the mass value without energy balance corresponds to the $\mu\mu$ mass.

	UA1
Elektronkanal Ⓐ	
M_W	$82.7 \pm 1.0(\text{stat.}) \pm 2.7(\text{syst.})$ GeV/c^2
Γ_W (90% C.L.)	< 5.4 GeV/c^2
M_Z	$93.1 \pm 1.0(\text{stat.}) \pm 3.1(\text{syst.})$ GeV/c^2
Γ_Z (90% C.L.)	< 5.2 GeV/c^2
Myonkanal Ⓑ	
M_W	$81.8^{+6.0}_{-5.3}(\text{stat.}) \pm 2.6(\text{syst.})$ GeV/c^2
M_Z	$90.7^{+5.2}_{-4.8}(\text{stat.}) \pm 3.2(\text{syst.})$ GeV/c^2
Taukanal Ⓒ	
M_W	$89 \pm 3(\text{stat.}) \pm 6(\text{syst.})$ GeV/c^2

	UA2
Elektronkanal Ⓐ	
M_W	$80.2 \pm 0.6(\text{stat.}) \pm 0.5(\text{syst.}_1) \pm 1.3(\text{syst.}_2)$ GeV/c^2
Γ_W (90% C.L.)	< 7 GeV/c^2
M_Z	$91.5 \pm 1.2(\text{stat.}) \pm 1.2(\text{syst.}_1) \pm 1.7(\text{syst.}_2)$ GeV/c^2
Γ_Z (90% C.L.)	< 5.6 GeV/c^2

A:	Electron Channel
	Electron Channel
B:	Muon Channel
C:	Tau Channel

Table 7.2: The W and Z Masses Measured in UA1 and UA2

Experi-ment	Ⓐ Zerfalls-kanal	$\sin^2\bar{\theta}_W =$ $1 - \frac{M_W^2}{M_Z^2}$	$\sin^2\bar{\theta}_W =$ $\frac{A_0^2}{M_W^2}\frac{1}{1-\Delta r}$
UA1	e	0.211 ± 0.025 (stat.)	0.218 ± 0.005 (stat.) $\pm$ 0.014 (syst.)
UA1	μ	0.187 ± 0.148 (stat.) $\pm$ 0.033 (syst.)	0.223 $^{+0.033}_{-0.029}$ (stat.) $\pm$ 0.014 (syst.)
UA2	e	0.232 ± 0.025 (stat.) $\pm$ 0.010 (syst.)	0.232 ± 0.003 (stat.) $\pm$ 0.008 (syst.)

A: Decay Channel

Table 7.3: The Measured Weak Mixing Angle

Experiment	R_{exp}	R^{max}_{exp} (90% CL)	R^{max}_{exp} (95% CL)
UA1	$9.1^{+1.7}_{-1.2}$	11.5	12.2
UA2	$7.2^{+1.7}_{-1.2}$	9.5	10.4
Ⓐ UA1 und UA2	$8.4^{+1.2}_{-0.9}$	10.1	10.5

A: UA1 and UA2

Table 7.4: Experimental Values of R = $(\sigma B)_W/(\sigma B)_Z$

Experiment	Kanal Ⓐ	ρ
UA1	e	$1.009 \pm 0.028\,(\mathrm{stat.}) \pm 0.020\,(\mathrm{syst.})$
UA1	μ	$1.05 \pm 0.16\,(\mathrm{stat.}) \pm 0.05\,(\mathrm{syst.})$
UA2	e	$1.001 \pm 0.028\,(\mathrm{stat.}) \pm 0.006\,(\mathrm{syst.})$

A: Channel

Table 7.5: The Measured Parameter

Chapter 8

Summary

In the years 1982 to 1985 the intermediate vector bosons $W^{\pm}$ and Z^0 were detected in all the leptonic decay channels. In the present work we examined experimentally the production of the Z^0 in proton-antiproton collisions, followed by decay of the Z^0 into two muons. At present this is possible only in the UA1 experiment.

Within the framework of this work I was initially responsible for the correct data readout from the muon detector. For this purpose it was necessary to build a monitoring system based on microprocessors, which could be used to monitor and test our apparatus. This monitoring system contains numerous programs for the diagnosis of the equipment. In the analysis I first selected the Z^0 events in the runs of 1984 and 1985, and then determined the efficiency of this selection. I also participated in setting up the $p_t^{\mu} > 15$ GeV/c selection. Then the Z^0 sample was tested for completeness, and the background calculated anew. The methods of energy balance and mass fitting were refined and systematized. Thus the production properties and the mass of the Z^0 could be determined for the first time for the entire measurement period of the UA1. The determination of the parameters of the standard model was done by also including the results of analyses from other decay channels of the W and Z bosons.

At center-of-mass energies of $\sqrt{S}$ = 546 GeV and $\sqrt{S}$ = 630 GeV a total of 21 Z^0 events were identified by means of their muonic decay. The analysis of the data yielded the following significant results:

1) The mass and the decay properties of the neutral intermediate vector boson, as they were measured in the muonic channel, are in agreement with the predictions of the minimum standard model of the electroweak interaction. We found:

$$M_{Z^0} = 90.7^{+5.2}_{-4.8}(\mathrm{stat.}) \pm 3.2(\mathrm{syst.})\ \mathrm{GeV}/c^2 \ . \tag{8.1}$$

The angular distribution of the leptons is in accord with the theoretically required V-A character of the neutral currents. From the asymmetry we calculate the electroweak mixing angle to be:

$$\sin^2\theta_W(Asym.) = 0.24^{-0.05}_{-0.04} \ . \tag{8.2}$$

The mixing can be determined even better from the ratio of the $W^\pm$ and Z^0 masses. In the muon channel we find:

$$\sin^2\theta_W(M_W, M_Z) = 0.187 \pm 0.148(\mathrm{stat.}) \pm 0.033(\mathrm{syst.}) \ . \tag{8.3}$$

If one takes the weak mixing angle as known, then the mass ratio can be used to calculate the ρ parameter, whose value the minimum standard model predicts to be unity. In the muon channel we found:

$$\rho = 1.05 \pm 0.16(\mathrm{stat.}) \pm 0.05(\mathrm{syst.}) \ . \tag{8.4}$$

2) The measured cross sections of

$$(\sigma \quad B)^{\mu}_{546\ GeV} = 98.4 \pm 49.8(stat) \pm 19.9(syst) \tag{8.5}$$

(8.6)

are compatible with the prediction of the Drell-Yan production mechanism, which was extended by applying quantum chromodynamics effects. From the ratio of cross sections it is possible to put an upper bound on the number of light neutrino generations N_ν. If one averages over all decay channels and over the UA1 and UA2 experiments, one finds, with 90% confidence, that

$$(\sigma \cdot B)^{\mu}_{630\ GeV} = 65.9 \pm 17.2(stat) \pm 10.9(syst) \tag{8.7}$$

3) The longitudinal momentum distribution of the vector bosons reflects the structure functions of the annihilating particles. The large transverse momentum is quantitatively explained by perturbing QCD effects, such as gluon bremsstrahlung. The frequency of jets caused by this effect corresponds to the theoretical expectations.

4) Other than the known Z^0, additional heavy neutral vector bosons at a mass of less than 173 GeV/c^2 were excluded. The high-energy photons that appear in the Z^0 decay are explainable on the basis of the process of internal QED bremsstrahlung.

More precise results are available from the electron channels in the UA1 and UA2 experiments due to the better statistics and finer resolution.

Future physics in intermediate vector boson (IVB) physics will make it possible to determine the parameters of the standard model better. The emphasis will be on a precision measurement of the masses of the bosons, in order to be able to detect any potential deviations from the standard model. Two experimental paths are followed towards this goal: Using the electron-positron colliders LEP and SLC, it will be possible to study both the mass of the Z^0 and also its width and all the decay channels very well. At the CERN $p\bar{p}$ collider improved UA1 and UA2 detectors will be used, together with the improved luminosity, to measure the properties of the $W^{\pm}$ more precisely. A similar research program will be carried out at the Tevatron.

Appendix A

Operation and Monitoring Of the Muon Detector

A.1 The Power Supplies

The muon chambers require several supplies, which are shown schematically in Fig. A.1. Three LeCroy type LRS 2132 units provide the high voltages on the anodes (+3 kV), the cathodes (-7 kV), and the field-shaping cathodes (-5 kV). These power supplies allow computer control of the applied voltages and the maximum permitted current. These units, which are equipped with microprocessors have a fault-current circuit which regulates the voltage downward in a controlled fashion if the maximum current should be exceeded even only for a short period of time, for example if there is a spark discharge in the chamber. In addition the computer connected to the system will cause an interruption of the control program and sound an alarm. One channel of the LeCroy nits supplies several chambers in common, which are connected together in such a way that upon switch-on the load current, which results from the load resistance and the capacitance of the chambers does not exceed the maximum value of 500 μA for the cathodes and 100 μA for the anodes.

The low-voltage supply is provided by way of linear circuit elements with a maximum current of 100 A, which are switched by hand. For monitoring we read out the voltages and currents of each part of the circuit by means of an analog-to-digital converter. If either current or voltage values fall outside the prescribed tolerances, an alarm is indicated at the computer.

The gas mixture is delivered from a central supply station in UA1. The quality control with respect to the correct adjustment of the mixture and the oxygen concentration is done by the monitor program of the central detector. We merely check the gas flow rates at the inlet and outlet of each chamber. The 116 flux meters are read out by several interfaces that make their data available to the computer on demand, and that forward any error messages to the computer on their own initiatives. The control of all parameters is done with a type CAVIAR [134] microprocessor which contains an interface to a CAMAC controller as well as a graphics terminal. In addition to the controls of the MUON detector this CAVIAR also has access to a CAMAC frame in which fast counters make it possible to monitor all the muon trigger rates. This most important task for the experiment was achieved by S. Levegrün and described in her diploma thesis [135].

The microprocessor runs a program in which the user has access at any time to all monitor tasks and the control of the high voltage, by making selections from a menu. If the user is inactive, after 30 seconds the program will independently choose the next monitoring task, according to a prioritized list. If a measured value falls outside its tolerance limits, the program initiates an acoustic and optical alarm.

A.2 Control of the Data Flow and the Events

The 14 CAMAC frames that contain the drift time digitizers (multiple time digitizers (MTPs) [136]), and the CAMAC frame with the buffers of the fast-trigger decisions for each individual event, are serially processed with a REMUS read-out electronics unit [137]. In a normal event the MTD's deliver a total of about 50 to

100 16-bit words, and the FT buffers [138] another 200 words. These are then transferred on at a rate of 1 word per μs to the central read-out system by way of the REMUS bus.

Before these data leave the area of our electronics, they pass through two buffered data switches [139] located in a CAMAC data frame controlled by another CAVIAR microprocessor. Fig. A.2 is a block circuit diagram. These switches can be set in such a way that the data stream flows either to the CAVIAR or to an additional read-out system located in a VME frame (described below) or to the central data read-out.

This makes it possible to operate the muon detector independently of all the other detectors of the UA1. This independence has shown itself to be absolutely indispensable in practice, since only in this manner were we able to bring our complex device with its multiplicity of electric components to error-free operation. This system, in combination with a test pulse distributor and a special way of operating the fast trigger, also made it possible to measure the efficiency of the detector as well as of the trigger outside the time of official data collection.

An additional property of the data switches was used for monitoring the events. These units are capable of providing, if an event is requested, for example by the central read-out unit, a copy of their data at their second out-put. In order to provide synchronization with the main output the copied data must be buffered once more, in case the computer connected to this output is too slow.

At the time the data was being collected we used this so-called "SPY" mode to monitor our events. The CAVIAR connected to the unit is capable of checking the data structure within 15 s, and activating alarms, if necessary, as well as filling about 250 histograms. The histograms store the hit distributions in the chambers and the decisions of the fast trigger. In addition, a colored representation of a chamber chosen according to selectable criteria, showing the drift tubes that were hit and the fast trigger decision, can be out-put in this same time period. Fig. A.3 shows a copy of the original log-book with one such picture.

Because of the continually increasing luminosity of the SPS the data stream flow rate to the central read-out has meanwhile risen to about 20 events per second. Our spot-check-type event monitoring has therefore become too slow in the configuration described here, and we have gone over to solving on-line tasks in a VME environment (see also Fig. A.2). The VME bus is an asynchronous bus with 20 MHz band width, which allows for 16-bit addresses and 16-bit data. Access to the data stream takes place, as in the past, by means of the already-described data switches, with a so-called RVMEX branch driver [140] which is capable of copying the data autonomously to an input of a memory module. At the other entrance of this so-called dual-port memory, several computers of the type DSSE-CPUA1 with a Motorola 68010 microprocessor [141] have access to the event via the VME bus. In each of these independent computers the same base program can run with different sub-programs, that undertake the individual tasks. At the same time, additional computers in the same VME frame can be used to work on program development.

To achieve this the CPM-68K operating system [142] was installed in the computers with some changes. The originally floppy-disk-oriented operating system was modified by us in such a way that all the computers start from a common, unerasable storage area, a so-called EPROM disk, that contains the system programs, a FORTRAN translator [143], as well as an assembler, a linker, a memory space management program, and a text-processing program. All the computers also have several over-writable so-called RAM disks available to them, whose data are in part protected against power loss by a battery buffering system. The microprocessors are connected to the UA1 On-line computer NORD 100/500 via a special interface on whose disk memory the programs are placed for long-term storage.

With this system we are now in a position to process between 10 and 1000 events per second, depending on the complexity of the task. In testing the detector, or if undesirable high-frequency oscillations in the electronics happen, we can transfer more than 50,000 words of data per event from the muon detector and analyze them.

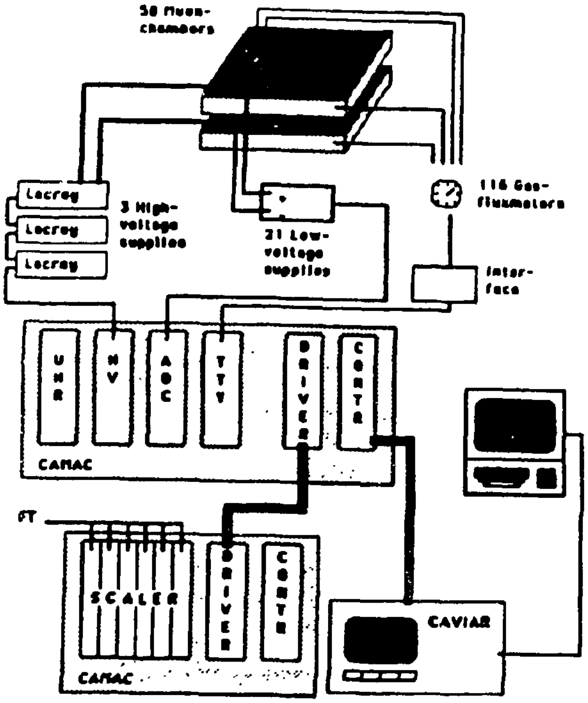

Fig. A.1: The Power Supplies and Monitoring of the Muon Chambers

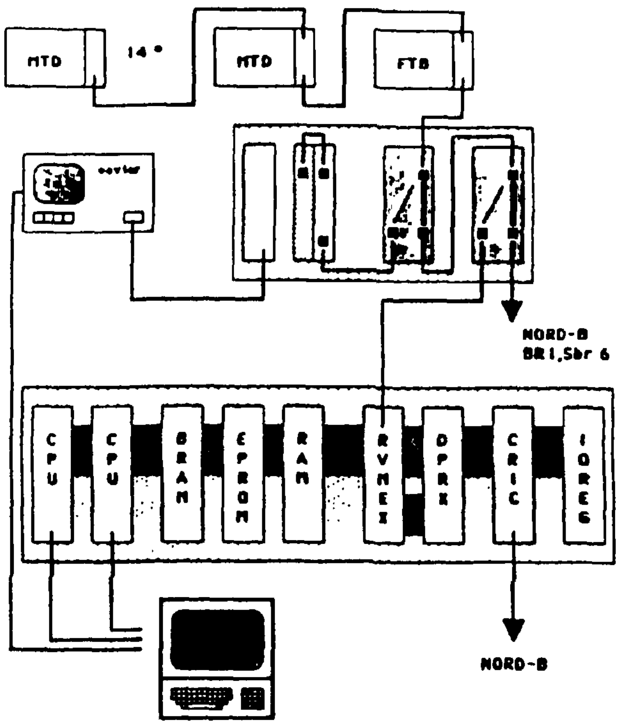

Fig. A.2: Data Read-out from the Muon System

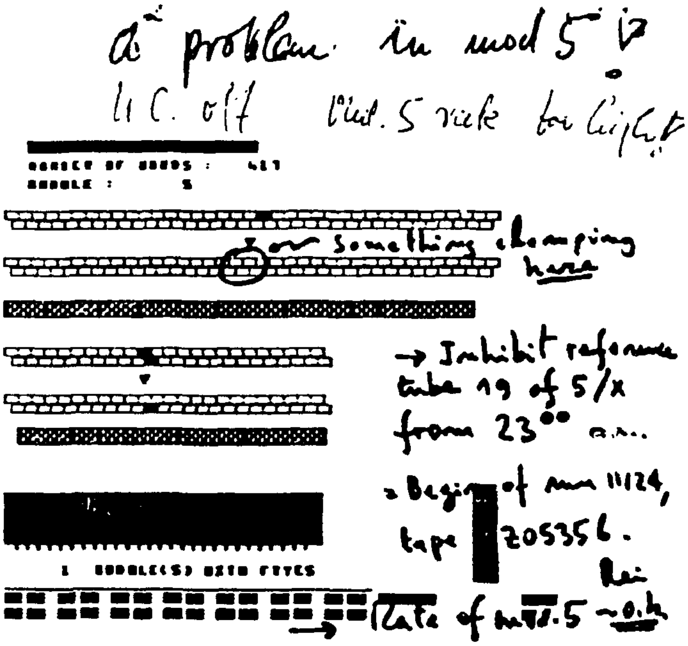

Fig. A.3: On-Line Representation of an Event in the Muon Chambers (Extract from the Log-Book)

Appendix B

The Monte Carlo Simulation

In this work a Monte Carlo program was needed for various purposes. First we studied the effects that arise due to the UA1 detector in detecting the particles or jets. Our apparatus is not a perfect detection device; rather it has only a limited spatial acceptance, and suffers from malfunctions of individual components. Thus the distributions that we infer from the data do not represent an exact representation of reality, since they are distorted by the properties of the detector, However, corrections for this effect can be made with the aid of a detector simulation. However, such a simulation needs artificially created events that correspond as accurately as possible to reality. The computer program ISAJET [144] is such an event generator.

However, with ISAJET we can do more than just study the detector effects. We are also in a position to compare the measured data with the predictions from various theoretical models, and to see what happens when the model parameters are varied. In addition the influence of background events can be observed.

B.1 The ISAJET Program

ISAJET was written by F. Paige and S. Protopopecu and developed further in a continuous dialogue with the UA1 collaboration. It is in a position to simulate processes of the strong, the weak, and the electromagnetic interactions, working with lowest-order perturbation calculations. Thus it is possible to investigate the production of quarks and gluons as well as the decays of the W and Z bosons that were created by the Drell-Yan production mechanism.

The reactions of the incoming quarks are treated with quantum chromodynamic perturbation calculations in first order. This creates out-going leptons, quarks, or gluons. However, quarks and gluons are not observable as free particles; they fragment independently of each other into hadrons [145]. The Monte Carlo program must be capable of describing a wide range of momentum transfers, from several 100 GeV^2 in the hard inelastic scattering of the incident protons, up to $Q^2 \leq 16\ \mathrm{GeV}^2$ in the hadronization. At small values of Q2 the so-called confinement of the quarks plays an important role; in this case it is no longer possible to work with QCD perturbation calculations, but rather one needs models.

A big problem consists of the simulation of gluon bremsstrahlung in the initial state, a process which is of great importance in the investigation of the vector bosons, since this produces the transverse momentum of, for example, the Z^0 . ISAJET is capable of such simulations. The generation of a Z^0 event takes place in the following steps in ISAJET:

- 1) The simulation of the hard collision process.

  Based on a QCD cross section, which was folded with the structure functions of Eichten et al. [92] ($\lambda = 0.2\ \mathrm{GeV/c^2}$).

$$\sigma = \sigma_{QCD} \times f(x_1, Q^2) \times f(x_2, Q^2) \tag{B.1}$$

- 2) The production of a Z^0 in the standard model by the Drell-Yan process.

In this step we set $\sin^2 \theta_W = 0.214$, and postulate vector boson masses of $M_W = 83.4\ \mathrm{GeV/c^2}$ and $M_{Z^o} = 94.1\ \mathrm{GeV/c^2}$. However, in a Drell-Yan process of lowest order the vector bosons do not yet have a transverse momentum.

- 3) The Creation of a Transverse Momentum.

  For this purpose an additional gluon, which becomes a recoil jet, can be radiated off in the initial state. Alternatively, ISAJET also allows for explicit simulation of the processes:

$$q + g \rightarrow Z^0 + q$$
$$q + \overline{q} \rightarrow Z^0 + g$$

  These processes are dominant at high p_t, but for small p_t they result in a $1/p_t^2$ singularity in the cross section. A cut-off criterion parameter is therefore introduced:

$$P_t^{-2} \rightarrow (P_t^4 + P_{t0}^4(M))^{-1/2} \quad , \quad P_{t0}^2(M) = (0.1\ GeV)M \tag{B.2}$$

- 4) The hadronization of all remaining partons [149].

  In this step additional jets may in some circumstances be created from the non-participating quarks and the remaining gluons.

ISAJET reproduces approximately the P_t distribution as calculated by Altarelli [87]. The radiative emission of quarks and gluons in the initial state is based on procedures that were first developed by Fox and Wilfram [146] and later improved [147, 148]. In this procedure a virtual mass, that may be used up in further inelastic processes, is assigned to the partons. The method works satisfactorily down to a parton energy of 6 GeV. Below this threshold ISAJET proceeds according to a model by Feynman and Field, in which the hadronization is simulated by independent fragmentation of the partons [145]. The treatment of the non-participating quarks, which become the so-called beam jets, is done in accordance with an idea by Abromovskii et al. [149]. Some of the algorithms were calibrated on the basis of UA1 data, so that, for example, they describe correctly the energy flux outside the jets, which is difficult to model.

Wherever possible we have done without the absolute predictions of ISAJET, but rather have used the program to determine relative differences in distributions as the parameters were varied. By proceeding in this fashion the systematic errors in the underlying models have very little impact. In the analysis presented here, the focus of the Monte Carlo calculations is on the detector simulation for events from the ISAJET generator.

Acknowledgments

First of all, I thank my Doctor-father, Prof. Allkofer, who stimulated and supervised this work. I received many suggestions and much help from him. He also made possible my stay at the CERN European Nuclear Research Center, as well as several lecture trips both within and outside the country.

On location, I was taken care of by Dr. Dau. His circumspect guidance and the many helpful, critical discussions, always in a friendly atmosphere, were a strong support and a great help. I thank him especially sincerely for this.

I also thank Mrs. E. Tscheslog very much. I cleared up many points of this work with her. She gave me valuable suggestions and gave me support in the development of the analysis programs.

At the time of the data collection, it was a pleasure for me to solve the problems associated with on-line programming and the operation of the detector with Mr. P. Erhard. I thank him for this good collaboration.

I thank Mr. T. Redelberger for the great patience he exhibited in answering my many questions on the UA1 standard programs. He was an important, always helpful discussion partner. With him I also discussed many problems on the edges of our field in a most pleasant atmosphere.

During the course of the analysis I had frequent occasion to discuss important points of this work with Prof. K. Eggert; he also smoothed the path for me to lectures in Italy and Japan. I thank him for this.

I had instructive conversations with Prof. Faissner about the origin of the hard photons in our events, for which I am much beholden to him.

Messrs. S. Wimpenny and S. Haywood were active co-workers in the W/Z Analysis Group. I thank them, and the other members of the group, namely Dr.

M. N. Minard, Dr. E. Locci, Dr. A. Norton, Dr. M. Della-Negra and Dr. D. Denegri, very much for their many helpful suggestions and their support.

I owe many thanks to Prof. Rubbia and the entire UA1 team. Without the enthusiastic leadership of the experiment by Mr. Rubbia, and without the cooperation of the entire group an experiment on so large a scale could, in my view, hardly have been feasible.

I am very grateful to Mrs. S. Levegrün and Mr. M. Schröder for their vigorous help with the final sprint.

Mrs. C. Rigioni drew a portion of the figures, for which I am thankful to her.

I also thank the Federal Ministry for Research and Technology, which supported our experiment and my stay in Geneva.

This work was written using the text processing program LATEX by D. Knuth and L. Lamporte, to whom I also express my thanks here.

Not least, my most heart-felt thanks go to my parents, who supported my education so very much. Especially in the most difficult times, in which I needed help in finding my direction, they were a great support to me.

I also wish to thank A. and H. Höhne personally. They know why.

Index of References

[1] Lucretius, *De Rerum Natura*

[2] I Newton, *Philosophiae naturalis principia mathematica* (1687)

[3] C. Domb, "Clerk Maxwell and Modern Science" , *Xerox College Publishing* (1963)

[4] A. Einstein, "Akademie-Vorträge", *Akademie Verlag Berlin*

[5] E. Rutherford, *Phil. Mag.* **21** (1911) 669,
E. Rutherford, *Phil. Mag.* **37** (1919) 537,
H. Geiger, E Marsden, *Phil. Mag.* **25** (1913) 604

[6] H. Yukawa, *Proc. Math. Soc. Japan* **17** (1935) 48
C.M.G. Lattes et al., *Nature* **159** (1947) 694

[7] I. Curie, *C. R. Acad. Sci. Paris* **198** (1934) 254

[8] H. Becquerel, *C. R. Acad. Sci. Paris* **122** (1896) 501

[9] E. Fermi, *Nuovo Cimento* **11** (1934) 1
E. Fermi, *Zeitschr. Phys.* **88** (1934) 161

[10] W. Pauli, *Proc. 7th Solvay Congress, Bruxelles*, (1933), (Gauthier-Villars, Paris, 1934) S. 324

[11] R.P. Feynman, *Phys. Rev.* **76** (1949) 749
R.P. Feynman, *Phys. Rev.* **76** (1949) 769
R.P. Feynman, *Phys. Rev.* **84** (1951) 123

[12] S.L. Glashow, *Nucl. Phys.* **22** (1961) 579

[13] A. Salam, J. C. Ward, *Phys. Lett.* **13** (1964) 168

[14] S. Weinberg, *Phys. Rev. Lett.* **19** (1967) 1264

[15] T.D. Lee, C. N. Yang, *Phys. Rev.* **104** (1956) 254

[16] C.S. Wu et al., *Phys. Rev.* **105** (1957) 1413

[17] M.T. Burgy et al., *Phys. Rev.* **110** (1958) 1214

[18] R L Kelly et al , *Rev. Mod Phys.* 52(2) (1980)

[19] J. Schwinger, *Ann of Physics* 2 (1957) 407

[20] O. Klein, *Proc symposium Warshaw*, (Inst. Int. de Cooperation Intellectuelle, Paris) (1939) p 6

[21] F.J. Hasert et al., *Phys. Lett.* 46B (1973) 121
F.J. Hasert et al., *Phys. Lett.* 46B (1973) 138

[22] Davis et al., *Phys. Rev. Lett.* 35 (1975) 1402

[23] J. Goldstone, *Nuovo Cimento* 19 (1961) 154
J. Goldstone et al., *Phys. Rev.* 127 (1962) 965

[24] P.W. Higgs, *Phys. Lett.* 12 (1964) 1156

[25] G. T' Hooft, *Nucl. Phys.* B33 (1971) 173
G. T' Hooft, *Nucl. Phys.* B35 (1971) 167

[26] M. Gell-Mann, *Phys. Rev.* 125 (1962) 1067,
G.F. Chew et al., *Sci. Amer.* 210 No.2 (1964) 74

[27] Y. Ne'eman, *Nucl. Phys.* 26 (1961) 222

[28] N. Cabibbo, *Phys. Rev. Lett.* 10 (1963) 531

[29] S.L. Glashow et al., *Phys. Rev.*D2 (1970) 1285

[30] U. Amaldi et al., *Phys. Rev.* D36 (1987) 1385,
J. V. Allaby et al., *CERN/EP* 80-140 (1980)

[31] M. Kobayashi, T.Maskawa, *Progr. Theor. Phys.* 49 (1973) 652

[32] S.D. Drell, T.M. Yan, *Ann. Phys.* 66 (1971) 578
C. Quigg, *Rev. Mod. Phys.* 49 (1977) 297

[33] E.W.N. Glover et al., *Phys. Lett.* 141B (1984) 429

[34] P. Aurenche, J. Lindfors, *Nucl. Phys.*, B185 (1981) 274,301

[35] G. Altarelli et al., *Nucl. Phys.*, B147 (1979) 461

[36] C. Rubbia et al., *Proc. Int. Neutrino Conf., Aachen*, (1976),Herausgeber : H. Faissner, H. Reithler und P.Zerwas (Vieweg, Braunschweig 1977)

[37] G. Arnison et al. (UA1), *CERN/SPSC* 78-06 (1978) 92
M. Banner et al. (UA2), *CERN/SPSC* 78-08 (1978) 93
B. Aubert et al. (UA3), *CERN/SPSC* 78-15 (1978) 96
M. Battison et al. (UA4), *CERN/SPSS* 78-105 (1978)114
M.G. Albrow et al. (UA5), *CERN/SPSC* 78-10 (1978) 108

[38] S. van der Meer, *Nobelpreis Rede 1984*,
S. van der Meer, *IEEE Trans. Nucl. Sci.* **NS-28** (1981) 1994,
D. Möhl et al., *Phys. Reports* **58** (1980) 73

[39] L. Szilard, *Zeitsch. f. Physik* **53** (1929) 840

[40] S. van der Meer, *CERN/PS-AA* 83-48 (1983)

[41] R. Johnson et al., *IEEE Trans. Nucl. Sci.* **NS-30** (1983) 2123

[42] M. Barranco Luque et al., *Nucl. Instr. Meth.* **176** (1980) 175
M. Calvetti et al., *Nucl. Instr. Meth.* **176** (1980) 255

[43] C. Cochet et al., *Nucl. Instr. Meth.* **A243** (1986) 45

[44] B. Aubert et al., *Nucl. Instr. Meth.* **176** (1980) 195

[45] M.J. Corden et al., *Nucl. Instr. Meth.* **238** (1985) 273
M.J. Corden et al., *Phys. Scr.* **25** (1982) 5,11

[46] G. Bauer et al., *Nucl. Inst. Meth.***A238** (1985) 288,
G. Bauer et al., *Nucl. Inst. Meth.***A253** (1987) 179,
G. Bauer et al., *Nucl. Inst. Meth.***A260** (1987) 101,
A. Bettini et al., *Nucl. Inst. Meth.***A253** (1987) 189

[47] R. Leuchs, *Diplomarbeit*, RWTH Aachen (1982)

[48] K. Eggert et al., *Nucl. Instr. Meth.* **176** (1980) 217

[49] J.C. Santiard, *CERN/EP* 80-04 (1980)

[50] G. Hilgers et al., *UA1/TN* 81-19[13]
G. Hilgers et al., *UA1/TN* 81-20
G. Hilgers et al., *UA1/TN* 81-21

[51] A. Astbury et al., *Nucl. Instr. Meth.* **A238** (1985) 288

[52] H. Lehmann, *Diplomarbeit*, RWTH Aachen (1984)

[53] M. Preischl, *Diplomarbeit*, CAU Kiel (1987)

[54] A. Moulin, *Diplomarbeit*, RWTH Aachen (in Arbeit)

[55] S. Levegrün, *UA1/TN* 85-94 (1985)

[56] J. Dorenbosch et al., *UA1/TN* 85-06 (1985)
J. Dorenbosch et al., *UA1/TN* 85-35 (1985)

---

[13] The UA1/TN references are Technical Notes from our experiment. They are not published.

[57] I. Ten Have, *UA1/TN* 85-70 (1985)

[58] P. M. Watkins, *private Mitteilung*

[59] I. Ten Have, *UA1/TN* 85-79 (1985)

[60] R. Leuchs, *Proc. Int. Symp. on the Physics of pp Collisions*, Tsukuba, *KEK report* 85-5 (1985) 178
R. Leuchs, *Proc. 5th. Topical Workshop on Proton-Antiproton Collider Physics, Aosta Valley*, Herausgeber: E. Greco, (World Scientific, Singapore) (1985)

[61] O. C. Allkofer, Introduction to cosmic radiation, *Thiemig* (1975)

[62] O.C. Allkofer et al., *Phys. Lett.* **36B** (1971) 425

[63] G. Arnison et al. (UA1-Kollaboration), *Phys. Lett.* **128B** (1983) 336
M. Bozzo et al. (UA4-Kollaboration), *CERN/EP* 84-91 (1984)

[64] S. Wimpenny et al., *UA1/TN* 86-28 (1986)

[65] R. Leuchs et al., *UA1/TN* 87-22 (1987)

[66] E. Tscheslog, *Diplomarbeit*, RWTH Aachen (1983)

[67] D. Charlton, *UA1/TN* 86-69 (1986)

[68] K. Wacker, *UA1/TN* 86-26 (1986)
N. Ellis, *UA1/TN* 85-43 (1986)

[69] N. Ellis et al., *UA1/TN* 86-82 (1986)
J. Richman, *UA1/TN* 86-74 (1986)

[70] M. J. Corden et al., *UA1/TN* 85-59 (1985)
M. J. Corden et al., *UA1/TN* 85-61 (1985)

[71] M. Jimack, *private Mitteilung*

[72] M. J. Corden, *UA1/TN* 85-60 (1985)

[73] V. Karimäki, *UA1/TN* 86-03 (1986)

[74] H. G. Moser, *Dissertation*, RWTH Aachen (1987)

[75] G. Bauer, *Dissertation*, Univ. of Wisconsin (1986)

[76] G. Arnison et al. (UA-Kollabration), *Phys. Lett.* **147B** (1984) 241

[77] C. Wulz, *Dissertation*, Techn. Univ. Wien (1986)

[78] N. Ellis et al., *UA1/TN* 86-79 (1986)
N. Ellis et al., *UA1/TN* 86-124 (1986)

[79] K. Wacker, *private Mitteilung*

[80] M. Banner et al. (UA2-Kollaboration), *Phys. Lett.* **122B** (1983) 322

[81] G. J. Alner et al. (UA5-Kollaboration), *Nucl. Phys.* B258 (1985) 505

[82] A. Breakstone et al., *Phys. Lett.*, **135B** (1984) 510

[83] M. Schröder, *Diplomarbeit*, CAU Kiel (1987),

[84] M. Aguilar-Benitz et al., (Particle Data Group), *Phys. Lett.* **170B** (1986) 1

[85] G. Arnison et al., (UA1-Kollaboration), *Phys. Lett.* **155B** (1985) 442
(siehe auch [74])

[86] S. Levegrün, *Dissertation*, CAU Kiel (in Arbeit)

[87] G. Altarelli et al., *Nucl. Phys.* **B246** (1984) 12,
G. Altarelli et al., *Zeitschr. Phys.* **C27** (1985) 617

[88] C. Albajar et al., *CERN-EP* 87-149 (1987) (eingereicht bei *Phys. Lett.*)

[89] R. Ansari et al. (UA2-Kollaboration), *CERN-EP* 87-48

[90] C. Albajar et al. (UA1-Kollaboration), *Phys. Lett.* **185B** (1987) 233

[91] J V. Allaby et al. (CHARM-Kollaboration), *Phys. Lett.* **B179** (1986) 301
J. Dorenbosch et al. (CHARM-Kollaboration), *Phys. Lett.* **B180** (1986) 303

[92] E. Eichten et al., *Rev. Mod. Phys.* **56** (1984) 579

[93] D.W. Duke, J.F. Owens, *Phys. Rev.* **D30**, (1984) 49

[94] C. Stubenrauch, *Dissertation*, Univ. Paris-Sud *CEA-N-2532* (1987)

[95] F. Halzen et al., *Phys. Lett.* **B78** (1978) 318
F. Halzen et al., *Zeitschr. Phys.* **C14** (1982) 351

[96] V. Barger et al., *Phys. Rev.* **D23** (1985) 413

[97] R. Odorico, *Phys. Rev.* **D31** (1985) 49

[98] C.T.H. Davies et al., *Zeitschr. Phys.* **C24** (1984) 133
C.T.H. Davies et al., *Nucl. Phys.* **B256** (1985) 413

[99] B. Humpert et al., *Phys. Lett.* **B93** 456

[100] G. Altarelli et al., *Phys. Lett.* **B151** (1985) 457

[101] S. D. Ellis et al., *Phys. Lett.* **B154** (1985) 435

[102] G. Steigman et al., *Phys. Lett.* **B66** (1977) 202

[103] G. Steigman et al., *Phys. Rev. Lett.* **43** (1979) 239
K.A. Olive et al., *Nucl. Phys.* **B180** (1982) 497

[104] J. Ellis et al., *Phys. Lett.* **B167** (1986) 457

[105] G. Arnison et al. (UA1-Kollaboration), *Phys. Lett.* **B166** (1985) 484
G. Arnison et al. (UA1-Kollaboration), *Europhys. Lett.* **1** (1986) 327

[106] J. Appel et al. (UA2-Kollaboration), *Zeitschr. Phys.* **C30** (1986) 1
R. Ansari et al. (UA2-Kollaboration), *Phys. Lett.* **B186** (1987) 440

[107] F. Richards, *Proc. 23. High Energy Physics Conf., Berkley*, Jul. 1986,
Experimente: ASP, Cello, MAC

[108] C. Albajar et al. (UA1-Kollaboration), *CERN/EP* 87-149 (1987) (eingereicht bei *Phys. Lett. B*)

[109] A.D. Martin et al., *RAL-87-02* (1987)

[110] F. Halzen et al., *MAD/PH/342* (1987)

[111] M. Diemoz et al., *CERN-TH* 4751 (1987)

[112] C. Albajar et al., *CERN-EP* 87-189 (1987) (eingereicht bei *Zeitschr. Phys.*)
C. Albajar et al., *CERN-EP* 87-190 (1987) (eingereicht bei *Zeitschr. Phys.*)

[113] I. R. Kenyon, *UA1/TN* 83-39 (1983)
S. J. Haywood, *Mid-term assesment*, Univ. Birmingham (1986)
S. J. Haywood, *Dissertation*, Univ. Birmingham (in Arbeit)

[114] S. J. Haywood et al., *UA1/TN* 86-29 (1986)
S. J. Haywood et al., *UA1/TN* 86-119 (1986)

[115] S. Brandt, Datenanalyse, *BI Wissenschaftsverlag*

[116] E. Tscheslog, *Dissertation*, RWTH Aachen (in Arbeit)

[117] S. J. Haywood et al., *UA1/TN* 86-122 (1986)

[118] A. Sirlin, *Phys. Rev.* D22 (1980) 971
W. Marciano, *Phys. Rev.* D20 (1979) 274
M. Veltman, *Phys. Lett.* B91 (1980) 95
F. Antonelli et al., *Phys. Lett.* B91 (1980) 90

[119] F. Jegerlehner, *Zeitschr. Phys.* *C* **32** (1986) 195
F. Jegerlehner, *Zeitschr. Phys.* *C* 32 (1986) 425
W. Hollik, *DESY* 86 049 (1986)

[120] W. J. Marciano et al., *Phys. Rev.* D**29** (1984) 945
W. J. Marciano et al., *Phys. Rev.* D**22** (1980) 2695

[121] F. A. Behrends, A. Böhm, *PITHA* 87-17, RWTH Aachen (1987), Vorabdruck aus *High Energy Electron Positron Physics*, Herausgeber: A. Ali und P. Soding, (World Scientific Singapore)

[122] E. Duchovni et al., *UA1/TN* 86-75 (1986)
K. Eggert, *private Mitteilung*

[123] G. Martinelli, *private Mitteilung*, (Die Wirkungsquerschnitte sind nach [87] mit einem Programm von G. Martinelli errechnet worden.)

[124] G. Arnison et al. (UA1-Kollaboration), *Phys. Lett.* **B126** (1983) 398

[125] P. Bagnaia et al. (UA2-Kollaboration), *Phys. Lett.* **B129** (1983) 130

[126] G. Arnison et al. (UA1-Kollaboration), *Phys. Lett.* **B126** (1983) 398

[127] R. Ansari et al. (UA2-Kollaboration), (UA2-Kollaboration), *CERN/EP* 87-117 (1987) (eingereicht bei *Phys. Lett. B*)

[128] F. Berends et al., *Nucl. Phys.* **B202** (1982) 63
F. Berends et al., *Nucl. Phys.* **B206** (1982) 61

[129] P. Bagnaia et al., (UA2-Kollaboration) *Zeitschr. Phys.* **C24** (1984) 1

[130] J. Fleischer, F. Jegerlehner, *Zeitschr. Phys.* **C26** (1985) 629

[131] A. Nandi, *private Mitteilung*

[132] B. Sadoulet, *UA1/TN* 82-34 (1982)

[133] B. Rossi und K. Greisen, *Rev. Mod. Phys.* **13** (1941) 240

[134] S. Cittolin, B. Lofstedt, *Proc. Topical Conf. on the Application of Microprocessors to High Energy Physics Experiments, Geneva*, 1981, *CERN 81-07* (1981) (yellow report)

[135] S. Levegrün, *Diplomarbeit*, CAU Kiel (1984)

[136] K.Eggert et al., *Nucl. Instr. Meth.* **176** (1980) 223
K. Eggert et al., *Nucl. Instr. Meth.* **188** (1981) 463

[137] P.J. Ponting, *CERN/EP-Electronics Note* 80-01 (1980)

[138] H. Reithler, *private Mitteilung*

[139] *CERN CAMAC Note 72-00* (1980)
CERN CAMAC Note 71-00 (1980)

[140] C. Engster et al., *Proc. VMEbus in Physics Conference, Geneva*, 7.Oct 85, *CERN 86-01* (1986) (yellow report)

[141] Data-Sud DSSE-CPUA1 *reference manual*

[142] Digital-Research CPM/68K *reference manual*

[143] H. van der Schmitt et al., *Proc. VMEbus in Physics Conference, Geneva* 7.Okt 85, *CERN 86-01* (yellow report)

[144] F.E. Paige et al., *BNL-29777* (1981),
F.E. Paige et al., *BNL-38034* (1986),
M. Della-Negra, *Phys. Scr.*, **23** (1981) 469

[145] R. Feynman, R. Field, *Nucl. Phys.* **B136** (1978) 1

[146] G. Fox et al., *Nucl. Phys.* **B168** (1980) 285

[147] T. Gottschalk, *CALT-68-1241* (1985)

[148] T. Sjostrand, *Phys. Lett.* **157B** (1985) 312

[149] V.A. Abramovskii et al., *Proc. XVI Int. Conf. on High Energy Physics, (Batavia)*, (Vol. 1) (1973) 389

[Translation Note: Diplomarbeit = Diploma thesis; private Mitteilung = private communication, Nobelpreis Rede = Nobel Prize speech]

Index of Figures

2.1: The Fermi Ansatz and the New Three-Particle Interaction 33
2.2: On the Interference of the Z^0 34
2.3: Degenerate Vacuum Expectation Value with Spontaneous Symmetry Breaking 35
2.4: The Lowest-Order Drell-Yan Process 36
2.5: Invariant Two-Lepton Mass in Proton-Antiproton Collisions 37
2.6: Quantum Chromodynamics Corrections to the First-Order Drell-Yan Process: Gluon Radiative Emission in the Initial State and QCD Compton Effect 38

3.1: The CERN Storage Ring Facility SPPS 67
3.2 On the Optimum Cooling Rate 68
3.3: The Particle Density in the AA as Function of the Frequency 69
3.4: The UA1 Detector 70
3.5: The Coordinate System Used 71
3.6: The Central Detector 72
3.7: Two Elements of the Central Electromagnetic Calorimeter 73
3.8: One Element of the Central Calorimeter 74
3.9: The Arrangement of the Drift Chambers of the Muon Detector Since 1985 74
3.10: Schematic Design of a Muon Chamber 76
3.11: Cross Section Through a Drift Tube of the Muon Detector 77
3.12: On the Trigger Logic 78
3.13: The Grouping of Tubes for Defining a Muon Trigger 79
3.14: Block Diagram of the Muon Trigger 80
3.15: The Angular Resolution of the Muon Trigger 81

3.16: The Muon Trigger Areas That Were Used 82
3.17: The Acceptance as Function of the Rapidity of the Muon Trigger Regions 83
3.18: The Efficiency of the Muon Trigger in the First and Second Levels 84
3.19: On the Technique of the Combined Momentum Fit 85
3.20: Comparison of the Momentum Measurements in the CD and with OMF 86
3.21: On the Construction of Energy Vectors 87
3.22: The Precision of Neutrino Momentum Measurement 88

4.1: The Transverse Momentum Spectrum for the Inclusive Muon Events 111
4.2: The Identification of Muons 112
4.3: The Placement of the Cosmic-Ray Counters 113
4.4: Example of a Muon Decay in the Central Detector 114
4.5: The Acceptance as Function of $p_t(Z^0)$ 115

5.1: The Rapidity Spectrum of the Muons from Z^0 Decay 135
5.2: Transverse Momentum Spectrum of the Muons from Z^0 Decay 136
5.3: The Total Calorimeter Energy in Z^0 Decays 137
5.4: Hit Distribution Before and After the Time Fit in the Chamber 138
5.5: View of Event (12039,1267) 139
5.6: View of the Radiative Z^0 Candidate (UA1:18517,1469) $Z^0 \rightarrow \mu\mu\gamma$. 140
5.7: Energy Distribution of the Photon in Internal Bremsstrahlung 141
5.8: Angle Distribution Between the τ and the Nearest Lepton 142
5.9: Probability of External Bremsstrahlung for $Z^0 \rightarrow \mu\mu$ 143

6.1: The Partial Production Cross Sections of the Neutral Vector Bosons 158
6.2: A Quiet Z^0 Event (19208,17) 159

6.3: An Active Z^0 Event (11619, 518) 160
6.4: Longitudinal Momentum Distribution for the Z^0 161
6.5: The transverse Momentum Spectrum of the Z^0's 162
6.6: Mean Transverse Momenta of Drell-Yan Lepton Pairs 163
6.7: Multiplicity Distribution of the Jets 164

7.1: Likelihood Function in the Mass Fit, With and Without Energy Balance 193
7.2: Mass Distribution Without Applying the Energy Balance 194
7.3: Mass Distribution Using the Energy Balance 195
7.4: Logarithmic Mass Spectrum for 2-Muon Events 196
7.5: Dependence of the Radiative Corrections on m_t and m_H (From [119, 116]) 197
7.6: Correlation of the W-Z Mass Difference and the Mass of the Z 198
7.7: For the Definition of the Polar Angle θ^* in the Center-of-Mass System 199
7.8: Polar Angle Distribution of the Leptons in the Center-of-Mass System 200
7.9: Likelihood Function of the R-Determination in UA1 201
7.10: Number of Neutrinos as Function of the Mass of the Top Quark 202
7.11: Limits on Heavier W's and Z's 203

A.1: The Power Supplies and Monitoring of the Muon Chambers 218
A.2: Data Read-out from the Muon System 219
A.3: On-Line Representation of an Event in the Muon Chambers (Extract from the Log-Book) 220

Index of Tables

2.1: The Electroweak Quantum Numbers of the Fermions 39
2.2: Coupling Constants of the Vector and Axial Vector Current g_A and g_V 40

3.1: Properties of the Calorimeters and the Iron Absorbers 89
3.2: The Muon Trigger Rates for 1985 (From [55]) 90

4.1: The Significant Muon Trigger Regions in 1984 and 1985. 116
4.2: Number of Events According to the Individual Selection Steps 117

5.1: Some Properties of All the Z^0 Candidates 144
5.2: Event Parameters of the Radiative Z^0 Candidates 145

6.1: Parameters of the W and Z^0 Samples 165
6.2: Partial Production Cross Sections for W and Z^0 166

7.1: Masses of the Z^0 Events 204
7.2: The W and Z Masses Measured in UA1 and UA2 205
7.3: The Measured Weak Mixing Angle 206
7.4: Experimental Values of $R = (\sigma B)_W/(\sigma B)_Z$ 207
7.5: The Measured ρ-Parameter 208